City Research Online

City, University of London Institutional Repository

Citation: Crowley, B. J. (2020). High and low frequency dominated boundary layer transition through widely spaced discrete suction perforations. (Unpublished Doctoral thesis, City, University of London)

This is the accepted version of the paper.

This version of the publication may differ from the final published version.

Permanent repository link: https://openaccess.city.ac.uk/id/eprint/24744/

Link to published version:

Copyright: City Research Online aims to make research outputs of City, University of London available to a wider audience. Copyright and Moral Rights remain with the author(s) and/or copyright holders. URLs from City Research Online may be freely distributed and linked to.

Reuse: Copies of full items can be used for personal research or study, educational, or not-for-profit purposes without prior permission or charge. Provided that the authors, title and full bibliographic details are credited, a hyperlink and/or URL is given for the original metadata page and the content is not changed in any way.

City Research Online: http://openaccess.city.ac.uk/ publications@city.ac.uk

City, University of London

High and Low Frequency Dominated Boundary Layer Transition through Widely Spaced Discrete Suction Perforations

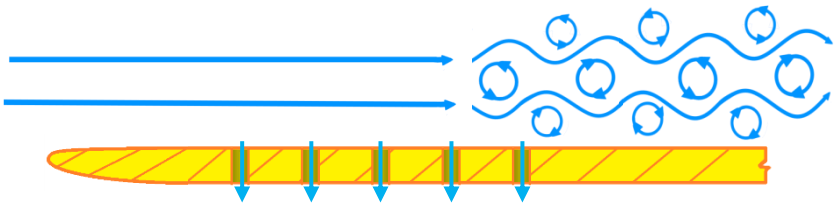

B.J. Crowley

09 Jun. 2020

Supervised by:

Prof. Chris Atkin,

Prof. Michael Gaster

Acknowledgements

This project would not be possible without the financial support of Airbus through AFLET, and ESPRC through LFC-UK. The author would like to thank the organisers for funding this project.

The author would also like the thank Prof. Chris Atkin for being the voice of reason when all reason has been lost; while allowing the author, the freedom to pursue some of their wilder imaginings. Most of all the author would like to thank Prof. Chris Atkin bringing the author into this project, which has been full of surprises and challenges.

The advice of Prof. Michael Gaster has also been essential to the success of this project. Mike's suggestions, critique, and discussion provided the author without a context for the problem that would have been unachievable through the literature alone. Mike's suggestions at key points of the project have had a significant impact on the projects progress to completion as well. For all these reasons, the author extends thanks to Prof. Mike Gaster.

The discussions of cross-flow transition with Evelien Van Bokhorst, have been very useful for the author. Comparison of the behaviour of the author's secondary instability and associated inflections of the mean flow, with the results from Evelien's swept wing study were very helpful in building confidence in the validity and character of the presented results.

The author would like the thank Keith Pamment, Richard Leach, Philip Beckwith, and Paolo Lo Giudice for helping the author correct some of the mistakes from the initial design of the suction plenum; and making the main piece of wooden housing for the pump. Their practical advice has also been important in the design of parts of the experimental setup.

Thanks are extended to Dr. Chetan Jagadeesh for his advice regarding leak testing of the suction plenum and providing advice on the construction of the porous inserts. Thanks are extended to Dr. Erwin Gowree for showing the basics the operation of the hot-wire anemometry instrumentation; and Dr. Marco Placidi for showing the more advanced functionality. Further thanks are extended to Marco for giving the author the opportunity to work on the wind-tunnel control code, without which many of the automated systems required to perform these suction experiments would not be possible. Thanks are also extended to Isabella Fumarola and Dhamotharan Veerasamy for their assistance in the laboratory.

Abstract

Boundary layer or wall-suction is a drag reduction technology with application to civil aircraft wings. Drag is reduced by increasing the extent of laminar flow across the boundary layer. Laminar flow has lower friction and form drag compared to turbulent flow. Wall-suction works by accelerating the air towards the surface of the wing, which has a stabilising effect on disturbances in the boundary layer; it also reduces the boundary layer thickness and thus the Reynolds number. In practice, this accelerated air must permeate through discrete pores in the surface. This creates local three-dimensional flow structures, which have been known to destabilise the flow and reduce the extent of laminar flow over wings, typically when the suction mass flow-rate is high. When this occurs the wall suction is said to be in a state of 'over-suction'.

In this work a set of experimental studies were performed on the problem of 'over-suction' for large arrays of suction perforations (in a widely spaced configuration), and for an isolated single suction perforation. It was found that the suction introduced a low frequency disturbance, this disturbance was found to grow (in amplitude) proportional to the suction rate. Furthermore, it was found that this low frequency was attenuated down-stream of the suction perforations, unless a pre-established N-type transition front was located close to the suction array. In this case the low-frequency was seen to interact with the N-type transition front, causing it to move upstream when at high suction rates. The amplitude of the low frequency also appeared to be Reynolds number independent, suggesting it may be an inflectional instability.

The low frequency was correlated with inflection points in the stream-wise velocity 'u' profile across the span 'z'. It has also been correlated with inflection points in the span-wise velocity 'w' profile across the wall-normal 'y'.

In the absence of any pre-established transition front, a high frequency disturbance was found to dominate the 'over-suction' process. This high frequency was found to only appear when the suction mass flow rate was sufficiently high, whereas the low frequency was found at all suction rates, and grew proportionally the non-dimensional suction mass flow-rate.

This high frequency was also correlated with inflection points in the stream-wise velocity 'u' profile across the span 'z'. It has also been correlated with inflection points in the stream-wise velocity 'u' profile across the wall-normal 'y'.

Contents

Nomenclature

A	Amplitude of disturbance	m/s
A_0	Initial amplitude of disturbance	m/s
A_s	Area of suction panel	m^2
A_c, B_c, n_c	Hot-wire calibration coefficients	N/a
Angles	Angles of hot-wire used in re-construction of 'w'	rad(N/a)
C	Length of plate/ chord length	m
C_s	Suction coefficient	N/a
Comb.uncty	Combined uncertainty of instruments	N/a
D	Pipe diameter	m
E_m	Mean voltage on hot-wire	V
E_f	Fluctuating/instantaneous voltage on hot-wire	V
F	Friction factor	N/a
F_0	Reference Friction factor constant	N/a
F_h	Fourier transformed hot-wire signal	m/s
F_r	Fourier transformed reference signal, for phase reconstruction	m/s
G_{window}	Window function for hot-wire signal	N/a
H	Shape Factor	N/a
I_{Tu}	Turbulence intensity	N/a
K	Minor Loss Coefficient (pipe-flow)	N/a
K_0,K_1	Reneaux and Blanchard criterion coefficients	N/a
L	Pipe Length	m
L_p,	Stream-wise length of applied suction	m
N	Number of samples	N/a
N_{hx}	Number of perforation rows (i.e.: in x-direction)	N/a
N_{hz}	Number of perforation columns (i.e.: in x-direction)	N/a
P_s	Static Pressure	Pa
P_T	Total Pressure	Pa
P_{Tf}	Total Pressure loss due to friction (pipe-flow)	Pa
P_{Tln}	Total Pressure loss due to minor system losses (pipe-flow)	Pa
P_∞	Atmospheric Pressure	Pa
Q_s	Volume flow rate through suction panel	m^3/s

Q_T	Predicted volume flow rate through suction system accounting for all losses using Darcy-Weisbach equation	m^3/s
$R_{\delta 1}$	Reynolds number defined with 'δ_1' as a length scale	N/a
R_1	Reynolds number defined with a unit length scale	N/a
R_x	Reynolds number defined with 'x' as a length scale	N/a
S, S_t	Strouhal number	N/a
S_{hx}, S_{hz}	Perforation row and column spacings in x and z directions respectively	m
S_D	Standard deviation of fluctuating velocity	N/a
S_E, ψ	Spectral energy	m/s
STD.uncty	Standard uncertainty of instrument	N/a
S.S	Beginning of Suction array location	
S.E	End of Suction array location	
S.H	Suction hole/perforation location	
T_∞	Ambient temperature	K
U_e, $u_{mean,e}$, u_e, u	Mean velocity in x-direction, at the boundary layer edge	m/s
U_∞, u_∞, u_{inf}	Mean velocity in x-direction, in the free-stream	m/s
U_κ	Boundary layer edge velocity over Roughness height	m/s
$V_{h,crit}$	Critical Suction velocity	m/s
V_p	Average velocity across suction array length	m/s
c, i	Constant, index value	N/a
d	Perforation diameter	m
d_{FC}	Perforation diameter at flight condition	m
d_{WTC}	Perforation diameter at wind-tunnel condition	m
e	Moody chart roughness parameter	m
f, f_n, f_k	Frequency	1/s
g	Acceleration due to gravity	m/s^2
g_c	Gain on hot-wire fluctuating voltage	N/a
h	Channel height	m
k_x, k_y, k_z	Wavenumbers defined in x, y, and z respectively	1/m
t, t_1, t_2,	Time	s
u_f, u'	Fluctuating/instantaneous velocity in x-direction	m/s

u_{hw45}	Hot-wire velocity measured at 45 degrees from free-stream direction	m/s
u_{hw0}	Hot-wire velocity measured at 0 degrees from free-stream direction	m/s
u_m, u_{mean}	Mean velocity in x-direction	m/s
u_{rms}	Root mean square of fluctuating velocity	m/s
$u_{rms,e}$	Root mean square of fluctuating velocity, at boundary layer edge	m/s
w, w_{mean}	Mean velocity in z-direction	m/s
$w_{mean,e}$	Boundary layer edge velocity component in z-direction	m/s
x	Displacement in stream-wise direction	m
y	Displacement in wall-normal direction	m
z	Displacement in span-wise direction	m
x'	Displacement along x-axis of traverse	m
y'	Displacement along y-axis of traverse	m
z'	Displacement along z-axis of traverse	m
Λ	Wing sweep	rad(N/a)
$\gamma_{dry\ air}$	Ideal gas constant for dry air	N/a
δ, δ_{99}	Boundary layer thickness, $y(u \rightarrow 0.99u_{e)}$	m
δ, δ_1	Displacement thickness	m
δ_{FC}	Displacement thickness at flight condition	m
δx	Step size used in integration	m
δ_{WTC}	Displacement thickness at wind-tunnel condition	m
ε	Orientation of rows in suction array (Offset angle from free-stream direction)	rad(N/a)
η	Non-dimensional wall-normal displacement	N/a
κ	Roughness height (as in Reneaux and Blanchard 1992)	m
μ	Dynamic viscosity	Pas
υ	Kinematic viscosity	m^2/s
ρ	Density	Kg/m^3
φ	Phase of fluctuating/instantaneous velocity	N/a
ω	Angular frequency	rad/s

1 Introduction

At the turn of the 21st century, engineering and the technical sciences are facing significant challenges regarding the sustainability of existing power systems. With the growing dangers associated with climate change, and the impending depletion of fossil fuels, there is a need to reduce or eliminate fossil fuel consumption. In the automotive industry this is being pursued through the adoption of electric and hybrid vehicles, reducing the environmental impact of the sector. However, in the aircraft industry there are currently no suitable electric or hybrid motors which can be used to replace the fossil-fuel-derived power-plants of modern commercial aircraft. It is unlikely that the development of such technologies will occur quickly enough to address the problem of climate change. For these reasons the focus in the aircraft industry has been on aerodynamic drag reduction. Moreover, in implementing a future electric propulsion system, early designs will likely perform more poorly than the existing designs, thus it would be beneficial to reduce the power and range such systems would be required to deliver.

A great deal of drag technology has been successfully developed and proven effective at least in the laboratory setting or through mathematical modelling (Lachmann 1961a; Lachmann 1961b). However, until recently there has been no urgency to adopt this technology, as it would increase manufacturing costs. The increased manufacturing cost, as well as the cost of development of such systems for commercial application has been long considered greater than the returns made through fuel savings. As appropriately divided between the volumes edited by Lachmann (1961), the two main areas of drag reduction have historically been: separation control, and Laminar Flow Control (LFC). There are additional technologies that do not fall strictly into these categories, such as: ribblets, and in-plane forcing.

This work will focus on LFC technologies which can greatly reduce fuel consumption through reduction of skin-friction and boundary layer thickness. These two effects have the benefit of reducing friction and form drag respectively. LFC technologies work by delaying the transition of the flow over the wing to a turbulent state, thus maintaining a laminar flow. Turbulent flow is characterised by having a higher skin friction drag and a thicker boundary layer, both of which are unfavourable in terms of aerodynamic drag.

A simple explanation for why turbulent flow has a higher friction drag than laminar flow: is that, in turbulent flow unsteady velocity perturbations are large in comparison to the mean steady velocity. In contrast, for laminar flows these perturbations are small, if energy conservation is considered: turbulent flow expends much more energy in travelling at the same mean velocity as a laminar flow, as energy is consumed in the production of the unsteady velocity perturbations.

A more detailed explanation would be to note that turbulent flows have a steeper velocity gradient close to the wall, as shear stress is proportional to velocity gradient and skin friction coefficient is proportional to shear stress at the surface of an aerodynamic body. Thus, turbulent flows have a higher skin friction coefficient than laminar flows.

To prevent transition to turbulence- LFC technologies attempt to arrest the growth of the small perturbations in the flow. If these perturbations are amplified, due to conditions in the flow, they will grow algebraically locally (usually dissipating further down-stream) but tend to grow exponentially far from the source of the disturbance. While small, these perturbations do not interact with one another or the mean velocity distribution across the flow.

Upon reaching sufficiently large amplitude they will induce more complex processes that lead to a turbulent flow: these processes are generally governed by interactions between different perturbations or with the mean flow. Of the developed LFC technologies, boundary layer suction shows particular promise. Suction has been shown to be effective for achieving full chord laminar flow in a flight test by Maddalon et al. (1989): this case represents the best out-come for drag-reduction, ignoring power requirements for the suction.

Suction attenuates perturbations in the flow through two mechanisms: the first reduces the thickness of the boundary layer, thus reducing receptivity of the flow to external disturbances through reduction of the Reynolds number parameter; the second effect is that the flow is accelerated towards the wall, and this has a stabilising effect on the flow.

Suction has been long theoretically modelled as being uniform (i.e. continuous) across the surface of an aerodynamic body. Under these conditions suction always has a stabilising effect on the flow. However, in practice air cannot permeate through a solid surface: thus, discrete pores, or gaps are required in the surface to allow for the passage of air. The result of this is that the suction becomes highly localised: producing local three dimensional flow structures, which tend to destabilise the flow. These structures have been observed to grow in proportion to the strength of suction. When these local flow structures grow sufficiently strong they cause premature transition, negating the stabilising effects of suction. This regime where the suction rate is past its optimal strength, in the context of delaying transition of the boundary layer, is called 'over-suction'.

This work has historically been conducted through two main approaches: determining the precise nature of the instability through detailed study of the local flow-field around the perforation (Goldsmith 1957; MacManus and Eaton 2000), and characterisation of the behaviour through parametric study (Ellis and Poll 1996; Reneaux and Blanchard 1992).

The goal of these parametric studies was to develop a set of (non-dimensional) criteria based on flow parameters, that predict the onset of premature transition through suction or 'over-suction'. Ideally, this would then serve as a design tool for potential LFC commercial aircraft, allowing the implementation of suction systems while avoiding 'over-suction', through careful control of critical design parameters. A detailed study of the flow physics helps to better inform these parametric studies, as an understanding is required to define all relevant dimensional parameters.

This study aims to determine the nature of the transition processes that occur at high suction rates through discrete perforations. The majority of prior work on this problem has been conducted in the 1950s and 1960s in studies such as by Butler (1955), Goldsmith (1956), and Gregory and Walker (1958). These studies found pairs of counter-rotating vortices shed from the suction perforations, and highlighted these vortices as a likely cause for premature transition, at high suction rates.

More recently, MacManus and Eaton (2000) found inflected velocity profiles behind the centres of the pairs of counter-rotating vortices shed from isolated suction perforations. A Direct Numerical Simulation (DNS) by Messing and Kloker (2010) found that the physical mechanism of the vortex generation changes on a swept wing, compared to that of an un-swept wing. On a swept wing due to interaction with co-rotating vortices generated by the sweep, one of the suction vortices (in a pair shed from an isolated perforation) is weakened and the other strengthened.

Early studies on discrete suction perforations were performed in an attempt to reduce surface discontinuities present with other transpiration media, such as with slots. They also have pores large enough to prevent clogging due to rain and dust, as was problematic with porous fabrics (Gregory 1961). However, the more recent focus on discrete perforations has been largely due to the development of laser and electron beam drilling (Saric and Reed 1986; Braslow 1999). This is because it has been shown extensively in the literature that the degree of disturbance due to the discrete nature of the transpiration media is proportional to the perforation size (Ellis and Poll 1996; Goldsmith 1957; Reneaux and Blanchard 1992; MacManus and Eaton 2000).

Laser and electron beam drilling allow the manufacture of perforations much smaller than was practical with twist drills (50μm compared to 0.5mm), and suction arrays made from such small perforations are typically highly resistant to 'over-suction' (Saric and Reed 1986). For this reason, the physics behind 'over-suction' and other potentially unfavourable effects due to the discrete nature of suction perforations has not been studied extensively in recent literature.

The usage of laser drilled perforations represents an extreme manufacturing solution for a problem that may be solved through a more comprehensive study of the flow physics. From a manufacturing perspective larger perforations may be preferable: as it could be the difference between thousands and millions of suction perforations, assuming dimensionless spacing is conserved. Furthermore, in early experiments, there were concerns of clogging due to dust and rain when using porous media, which contained perforations of comparable size (Gregory 1961). For these reasons, 'over-suction' remains an important topic in relation to suction.

To provide a comprehensive review of the design and system requirements to implement a suction system in a specified modern commercial aircraft: a set of studies were undertaken by Atkin (2001a, 2001b, 2002, 2010). This investigation looked in detail at the specific requirements to implement suction on an A310 wing, opting for minimal modification of the overall wing geometry and structure.

As part of this investigation 'over-suction' was identified as an unknown: with no universally accepted method of quantifying it. In Atkin (2001a): attempts were made to unify the different criteria available in the literature (see Section 4.4); however, it was found that some of the criteria appeared to be missing critical parameters. Some corrections to these criteria were suggested but were not validated. This prompted the work presented in this thesis, however, during the course of this investigation previously unidentified flow structures were observed at low frequency, which grew proportionally to the suction strength.

As a result of this the presented work became more a study of the cause and effect of these flow structures: as opposed to a parametric study aimed at unifying existing critical suction criteria. It was found that these structures interact with a pre-established transition front location, showing some dependency on its initial location (marking the discovery of a new dependent parameter). This is believed to be a separate mechanism of 'over-suction' from that which has been studied historically, as a high frequency dominated transition was observed to occur in the absence of a pre-established transition front. This mechanism was correlated with inflectional velocity profiles, similar to those reported by MacManus and Eaton (2000).

Additionally, as the physics of isolated perforations has been studied in detail by MacManus and Eaton (2000), this study will investigate if the physics is consistent for large arrays of over one thousand suction perforations. These perforations are widely spaced, based on criteria specified by Reneaux and Blanchard (1992), thus it was expected that the perforations would be sufficiently isolated to prevent interactions with neighbouring perforations through the induced vortices.

2 Aims and Objectives

The aim of this study was to study the presence of low and high frequency structures in the velocity field that were found to be affected by wall-suction.

The objectives of this study were to:

1. Identify the significance of the low and high frequency structures. I.e. how they affect laminar-to-turbulent transition for different flow conditions.
2. To identify the source of these disturbance fields, and compare with existing work in the literature.

3 Literature Review of Boundary Layer Transition

As a prelude to discussing laminar-to-turbulent transition, it seems prudent to discuss some basic characteristics of laminar and turbulent boundary layers. When fluid moves past a body, the fluid is affected by the surface friction of the body. Because Newtonian fluids have no structural stiffness (i.e. they are perfectly plastic). Only the fluid layer at the surface of the body is brought to rest.

Though lacking stiffness, fluid is viscous: this means that fluid naturally dampens out distortions and disturbances in its path of travel. The result of this is that there is a velocity gradient, moving away from the surface of the body (the wall), where the velocity 'u' changes from zero to a maximum value representative of flow free of viscous effects. This region of velocity gradient in which viscosity retards the flow velocity is called a boundary layer.

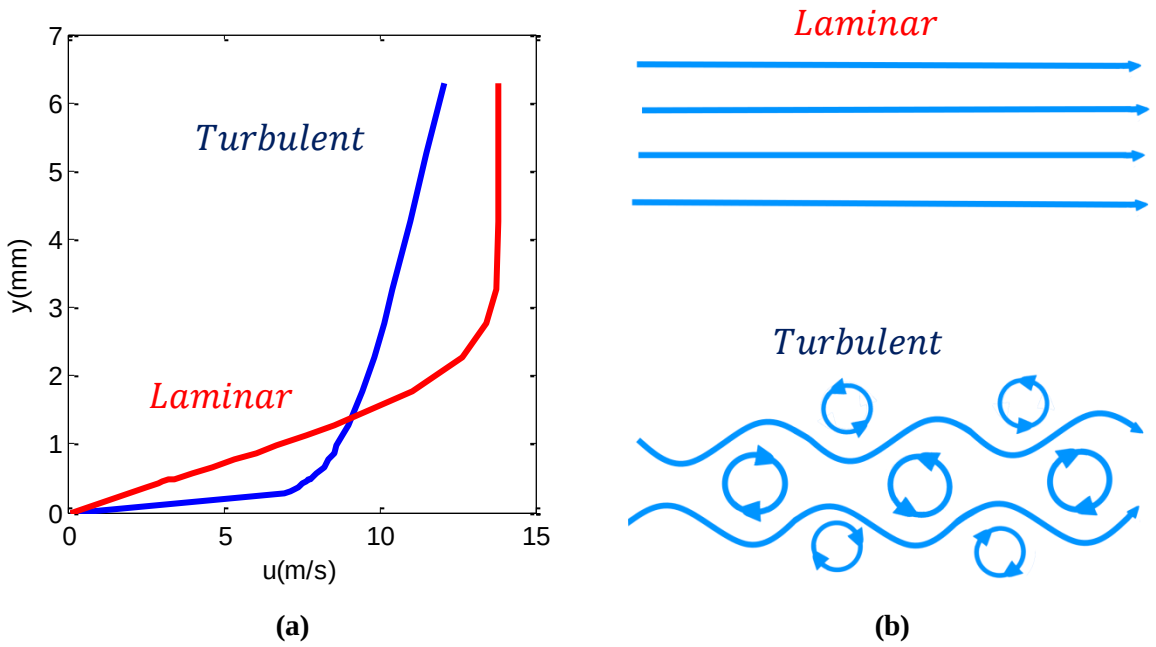

Figure 3.1: Illustration of laminar and turbulent boundary layers (a) shows velocity distributions across boundary layer, and (b) shows conceptual visualisation of laminar and turbulent flow.

The flow in a boundary layer has two basic states, one of low energy and one of high energy. Here the energy of fluctuations in the boundary layer is being specifically referred to. If a boundary layer has very low energy fluctuations, it can be described as laminar as the flow moves in well-ordered laminae across the wall-normal 'y'. If the boundary layer is dominated by high energy fluctuations the flow moves "chaotically" and is called turbulent. Figure 3.1 (a) shows the velocity distribution for laminar and turbulent profiles. Turbulent profiles have a steeper velocity gradient 'du/dy' at the wall, which is associated with higher skin friction drag.

To characterise the physics of ‘over-suction’ it must be discussed within the context of transition mechanisms defined in the literature. A transition mechanism is a process characterised by how structures in the flow change as it transitions to a turbulent state. The characteristic flow structures for specific mechanisms are often important in causing and sustaining the development of the laminar-to-turbulent transition process.

In this section some of the most common transition mechanisms are discussed for future comparison with results from Section 8. These mechanisms are commonly split between different regimes that succeed one another. Most transition mechanisms start in the linear regime, proceed to the weakly non-linear regime, and the flow becomes fully turbulent in the strongly non-linear regime.

The fundamental attributes of these three regimes will be discussed as a separate entry in this section, with special focus upon the linear regime, as it the best understood, and is the easiest to control of the three: thus making it important in the discussion of LFC technologies such as suction.

3.1 The Linear Regime

The transition process, in external flows, typically begins with a laminar boundary layer being influenced by sources of disturbance, such as: acoustic sound, free-stream vorticity, and surface roughness. These boundary disturbances create perturbations in the boundary layer, which may become spatially amplified, depending on flow parameters such as Reynolds number, flow geometry, pressure gradient, and the frequency of the disturbance.

If these initial disturbances are small, the resulting waves that develop in the flow will be amplified or attenuated independently of one another. In this, the waves or modes are said to be linearly independent of one another and are commonly referred to as linear waves or linear instabilities (Schlichting 1979).

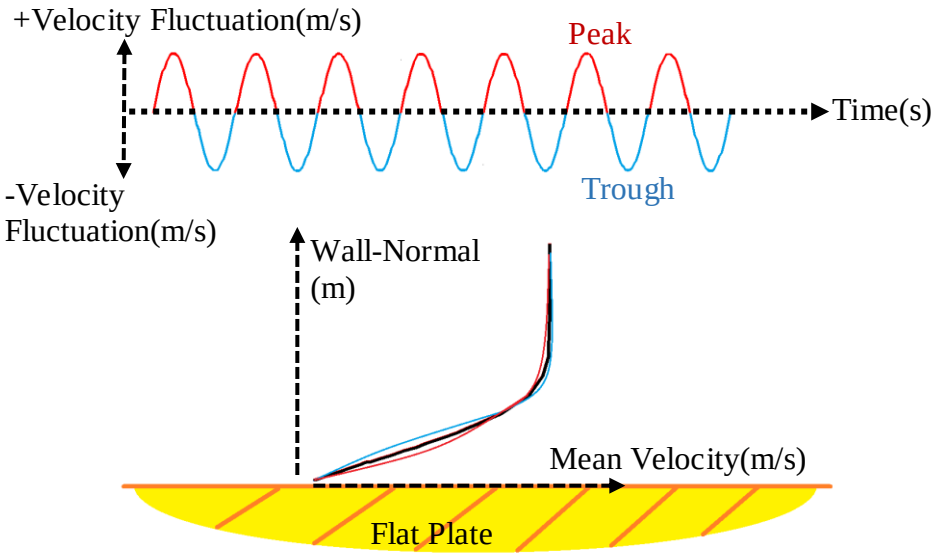

Figure 3.2: Illustration of linear wave acting on a laminar mean velocity profile. The net stabilising effect of the peaks and destabilising effect of the troughs average out.

The shape of the mean velocity profile ‘u’ across the wall-normal ‘y’ strongly affects the stability of disturbances in the linear regime. It can be shown from Rayleigh’s equation that inflectional mean velocity profiles associated with deaccelerating flows are inherently destabilising for velocity fluctuations in the flow (Schlichting 1977). More ‘filled out’ profiles associated with accelerating flows are stabilising.

If Figure 3.2 is considered, the destabilising effect of the blue line (associated with the trough of linear wave), super-imposed on the mean profile, is averaged out by the red-line (associated with the peak). Thus for small two-dimensional waves no net distortion is produced on the mean flow, and the waves can be considered linearly independent of the mean flow.

This usage of the term 'linear' to describe the aforementioned process and instability waves does not refer to growth rates, as the linearly independent instability waves are subject to either algebraic or exponential growth. In two-dimensional parallel flows in the linear transition regime, the fluctuating velocity 'u_f' can be represented as follows, in Equation 3.1, using Euler's formula.

$$u_f(x, y, t) = A(y) \cdot e^{i(k_x x - \omega t)} \qquad \textbf{Equation 3.1}$$

Here it is assumed that waves grow exponentially. For flow subject to temporal instability the temporal frequency (ω) is complex, where the imaginary part governs the stability of the flow: if it is positive the waves are amplified, if it is negative the waves are attenuated. In flows subject to spatial amplification the spatial wavenumber (k_x) governs whether or not the waves are amplified or attenuated. This formula was used to generate the plots shown in Figure 3.3. Here 'x' is distance from the leading edge 't' is time passed.

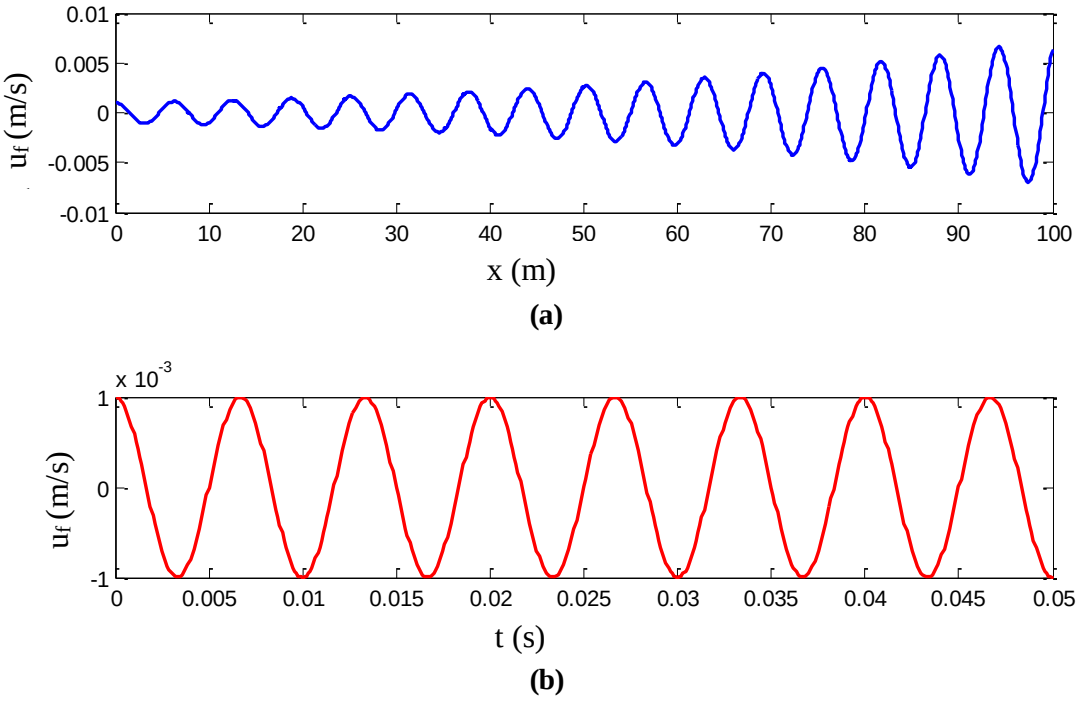

Figure 3.3: Spatially amplified instability waves: development in space is shown in (a), and development in time is shown in (b).

Linear waves are amplified in space or time depending on the flow. In certain types of internal flows, such as Taylor-Couette flow, instability waves grow or decay in time, while exhibiting neutral stability in space. For external flows, these waves are spatially amplified or attenuated as proposed by Gaster (1965b). Prior to this, instability waves were believed to be neutrally stable in space but subject to amplification and attenuation in time (Tollmien and Grohne 1961, p.603).

In Figure 3.3 an illustration of the concept of spatially growing waves is shown. It can be seen in Figure 3.3 (a) that the amplitude of the wave increases exponentially with increasing spatial displacement, in this case a weakly amplified wave is shown. In Figure 3.3 (b) it can be seen that the same wave maintains constant amplitude across the time domain.

Often when using forcing, such as with acoustic sound and a roughness, or an oscillating wall jet: there is a region of localised high amplitude close to the source. This amplitude decays rapidly down-stream from the roughness or wall jet. The region in which this decay occurs is commonly referred to as the near-field. At the end of the near-field when the forced wave has decayed to a minimum amplitude it starts to amplify gradually with an exponential growth rate.

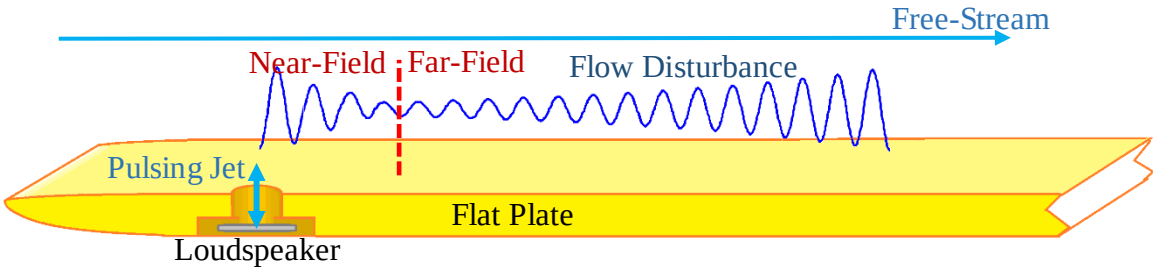

Figure 3.4: Illustration of disturbance near and far fields. The disturbance is introduced by a point source pulsating jet, controlled by a loud speaker inside a flat plate test model.

This second region that follows the near-field is called the far-field and encompasses the rest of the linear stages of the transition process. The example shown in Figure 3.3 would be situated entirely in the far-field. Examples of both the near and far-field regions are illustrated in Figure 3.4.

Disturbances in the near-field tend to grow and decay algebraically, whereas disturbances in the far-field are subject to exponential growth and decay. If these waves (either travelling or stationary) grow sufficiently large, due to spatial amplification, these formerly independent waves will start to interact with waves at other frequencies. Once this occurs the waves are said to be non-linear.

3.2 The Non-linear Regime

However, there are some basic characteristics common across the non-linear stages of transition. Based on experimental observations of the qualitative behaviour of the non-linear regime, the regime is split into ‘weakly’ and ‘strongly’ sub-regimes that are considered separately. This is in part because (ignoring Direct Numerical Solutions) weakly non-linear flow is mathematically modelled using techniques greatly different from those used to model flow that is strongly non-linear. Typically, weakly non-linear interactions are either between the mean velocity field and the fluctuating velocity field; or multiple modes in the fluctuating velocity.

Multiple modes in the fluctuating velocity field interact by resonating in sets of three, forming resonant triads. Resonant triads were proposed originally by Craik (1971): these triads consist of three resonating frequencies in the flow. Typically, one of these frequencies is the fundamental and the other two are oblique waves. To resonate, the sum of the frequency of these two oblique waves must equal that of the fundamental wave, additionally these oblique waves must propagate in opposite directions.

At discrete spatial locations, the modes in a triad are constructively interfering, forming troughs in the fluctuating velocity time series ‘$u_f(t)$’. These troughs interact with the mean velocity as a function of the wall normal ‘u(y)’ to create instantaneous inflection points in u(y). These inflection points seed the non-linear amplification of additional modes.

The type of transition mechanism is usually determined based on the types of non-linear iterations which take place in the weakly non-linear regime. In the strongly non-linear regime the modes appear to be strong enough to interact with modes at neighbouring frequencies. As can be seen in Section 8.2, the spectral energy of most strongly amplified modes (or bands of modes) appears to spread out to fill all neighbouring frequencies until all allowable frequencies have comparably high energy levels, thus forming a transition front. The precise nature of common transition mechanisms with their specific behaviours are described in the following sections.

3.2.1 K-Type

Discovered by Klebanoff et al. (1962), K-type was the first transition process in which the non-linear stages were investigated in detail. In the linear regime, the amplitude of velocity waves developing in the flow are too small to influence the distribution of velocity ‘u’ across the wall normal ‘y’. For this reason, the mean velocity distribution ‘u(y)’ or profile and its derivatives with respect to the wall-normal are used as inputs for the governing equations of linear theory: here it is assumed that the unsteady part of the velocity profile is sufficiently small to be neglected.

If the fundamental wave grows large enough that its contribution to the instantaneous profile is sufficient for it to deviate from the mean profile shape: then the flow can be considered weakly non-linear as the stability of waves are dependent on the shape of both the fluctuating and mean velocity profiles. This is illustrated in Figure 3.5 where it can be seen that inflection points appear in the velocity profile locally in time. This is important because Rayleigh (1880) showed that velocity profiles with points of inflection are inherently unstable. Though previously proposed by Klebanoff et al. (1962) the existence of these time-localised inflection points was verified by Nishioka et al. (1980). These points of inflection coincide with troughs in the time signal of the non-linear velocity waveform (see Figure 3.6).

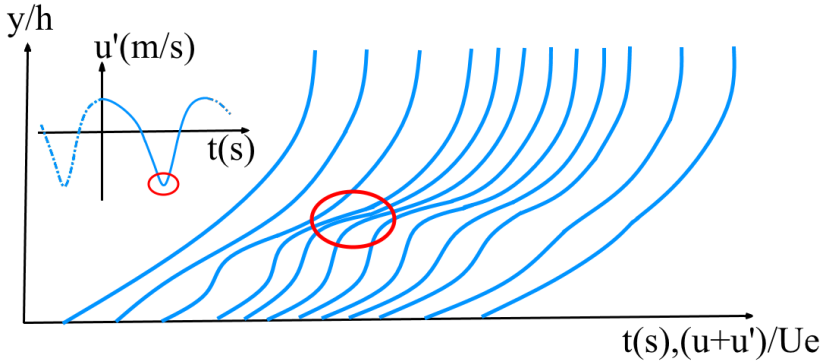

Figure 3.5: Diagram of inflection points in the instantaneous velocity profiles, reproduced from Nishioka et al. (1980).

In the time series of the fluctuating velocity at a fixed spatial position, such as shown in Figure 3.6, the high frequency that is amplified by the inflection points appears as ‘spikes’ due to the high frequency being of short wavelength and only being locally amplified in time. Were the inflection point consistent/uniform across the time series of the instantaneous velocity profile, the ‘spike’ generation would manifest as a set of continuous high frequency waves. Likely due to harmonic resonant triads, these ‘spikes’ appear to multiply when the associated high frequency modes grow large enough to saturate.

Though unconfirmed, the presence of resonant triads in the 'spike' multiplication stage, would explain the three-dimensionality of the K-type process which cannot be explained solely through a weakly non-linear interaction between the mean velocity and individual modes/waves.

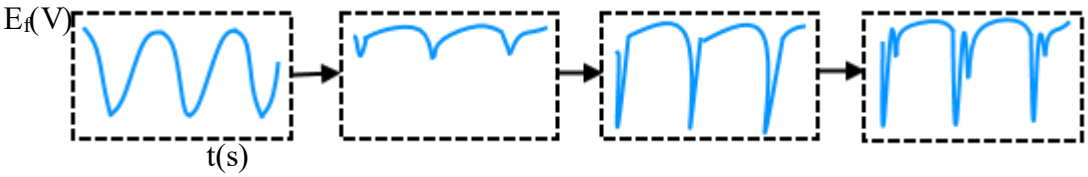

Figure 3.6: Time series showing the development of the fluctuating velocity component during K-type transition (Reproduced from Klebanoff et al. (1962)).

An alternative explanation proposed by Kachanov (1994) that these spikes are caused by resonance between the fundamental wave and its higher harmonics. It is claimed that the spatial phase component of higher harmonics will be constructively interfering at specific deterministic positions across the flow-domain, at these locations the spikes tend to appear. As the effect of the linear modes on the mean flow would average out for an isolated fundamental mode, it may be that resonant triads of the fundamental and higher harmonics are also required for the flow to become non-linear. It is also difficult to explain why transition is three dimensional without the presence of some resonant triads.

It has been claimed that K-type dominates in environments where the turbulence intensity is high, or where the initial disturbance amplitude is large (Kachanov 1994). Span-wise non-uniformity in the process is attributed to resonance of harmonics with three-dimensional oblique modes symmetric about the sub-harmonic of the dominant mode (Kachanov 1994). However, it is believed to be superseded by resonance of higher harmonics in the break-down to turbulence. If there is low background energy at higher frequencies, the sub-harmonic resonance is believed to dominate and cause N-type transition.

3.2.2 N-Type

N-type is believed to dominate in environments where the turbulence intensity is low, or where the initial disturbance amplitude is small (Kachanov 1994). The linear stage of this process is very similar to that of K-type, in that the process is characterised mainly by the spatial amplification of linearly independent two dimensional waves. In the weakly non-linear regime of N-type transition the process is dominated by resonant triads. In these triads two low frequency three-dimensional oblique waves resonate with a (approximately 2D) normal fundamental wave. Different wave types and their propagation angles are shown in Figure 3.7; oblique wave and streak do not propagate in the free-stream direction.

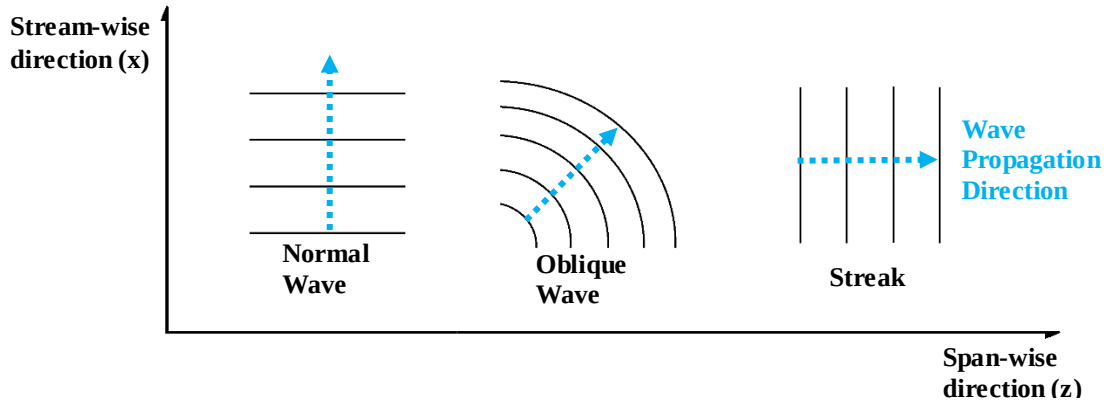

Figure 3.7: Illustration of different types of waves, based on information from Berlin (1998).

The theoretical basis for these triads was proposed by Craik (1971). To resonate, the sum of the frequency of the two oblique waves must equal the frequency of the fundamental. For this reason, the two oblique waves appear symmetrical or coincident about the sub-harmonic of the fundamental wave. The propagation angle of the oblique pair (in the xz-plane) must be symmetrical about the viscid stream-lines. In essence: span-wise wave numbers must be equal but of opposite sign (Schmid and Henningson 2001).

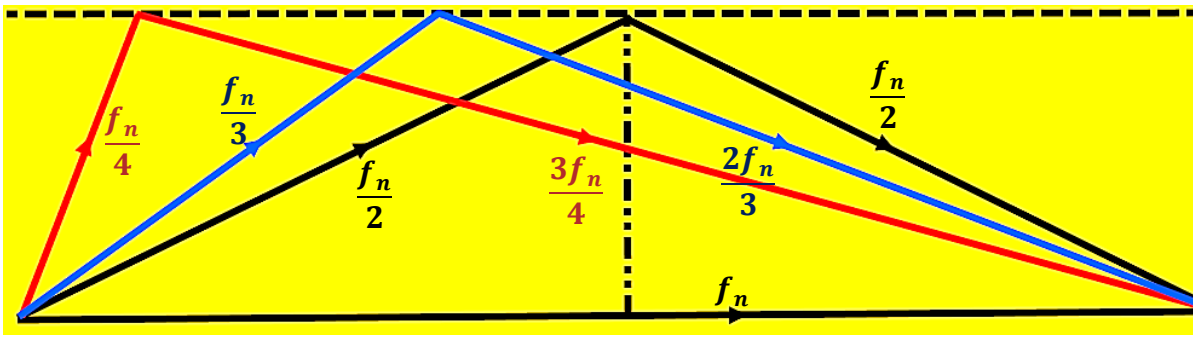

Figure 3.8: Illustration of the concept of resonant triads, f_n is the frequency of the fundamental wave.

This interaction was first observed experimentally by Kachanov et al. (1977) and was studied in detail by Kachanov and Levchenko (1982). Where the two oblique waves did not occur precisely at the sub-harmonic as Craik (1971) showed in their example, but instead occur in a plane of symmetry about the sub-harmonic, as seen in Figure 3.9. This plot shows the development of energy decomposed into individual frequencies, using a Discrete Fourier Transform (DFT), across the stream-wise direction.

In this experiment a two-dimensional travelling wave was generated using a vibrating ribbon, this wave can be seen as the disturbance at 100Hz in Figure 3.9. The sub-harmonic would be at 50Hz. As the oblique waves are symmetric about the sub-harmonic the deviation from the sub-harmonic frequency is equal but of opposite sign for each oblique wave. The sum of the frequencies of the two oblique waves still equals that of the two-dimensional fundamental wave, thus satisfying Craik's triad.

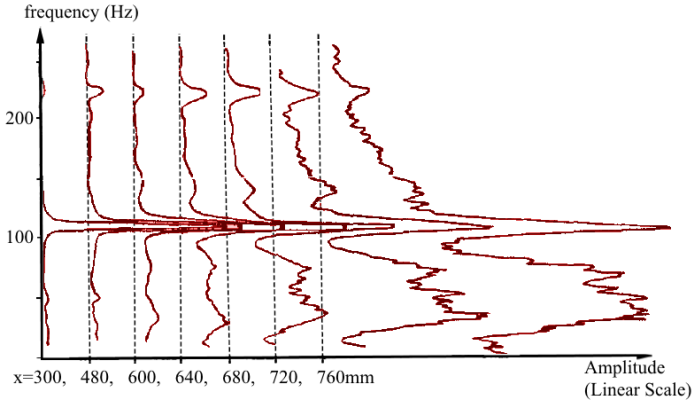

Figure 3.9: Development of spectral modes, with forcing at 100Hz, in N-type transition (reproduced from Kachanov and Levchenko. (1982))

It is claimed in (Kachanov 1994) that this process of resonant growth between the fundamental wave and a pair of oblique waves symmetrical about its harmonics also occurs in K-type transition, however this process does not lead to transition but instead is responsible for the flow becoming three-dimensional in the weakly non-linear stage of transition.

3.2.3 Cross-Flow Transition

The cross flow instability was originally discovered by Gray (1952) in a flight experiment (Reed and Saric 1989). Cross-flow transition, is a transition path most strongly associated with transition over swept wings. Cross-flow transition or qualitatively similar processes can occur in other flows with strong cross-wise pressure gradients. The cross-wise direction is defined as perpendicular to the stream-wise direction which is defined as tangent to the stream-lines. In addition the chord-wise direction is defined as perpendicular to the leading edge, and the span-wise direction as parallel to the leading edge.

All four of these directions are parallel to the surface of the model. Prior to the work by Cooke (1950), the span-wise direction was aligned along the span in what is currently referred to as the cross-wise direction (Pfenninger and Bacon 1961). In Cooke (1950) a new co-ordinate system was defined using the leading edge as datum, in which to align the "span-wise" axis.

This allowed for a simple self-similar solution for the three-dimensional boundary layer equations. As discrete suction induces cross-wise velocity profiles at and down-stream of the suction perforations, it is important to establish the defining features of cross-flow transition, for comparison with observed features in 'over-suction' transition mechanisms. It is important to note that when using suction on a two-dimensional model, the cross-wise and span-wise directions are coincident. Similarly, the stream-wise and chord-wise directions are also equivalent.

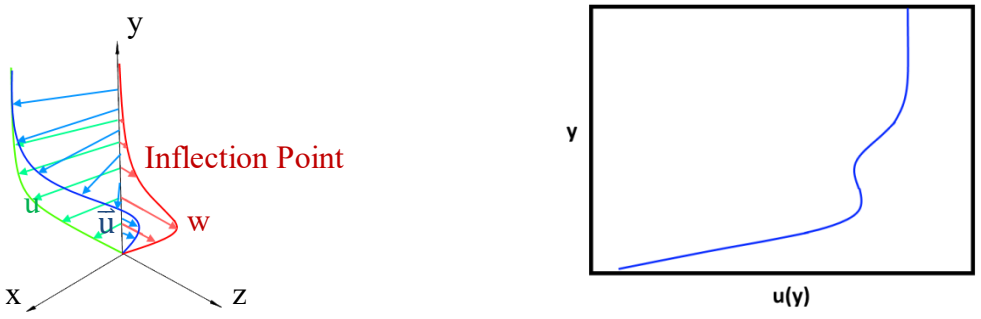

(a) **(b)**

Figure 3.10: Inflectional profiles associated with cross-flow transition: (a) shows the span-wise distortion associated with primary modes (reproduced from Linfield et al. 1961), (b) shows stream-wise distortion associated with secondary modes (reproduced from Kohama et al. 1989).

In cross-flow transition there are a set of primary modes attributed to the span-wise inflection point in the cross-wise velocity profile ‘w(y)’ as shown in Figure 3.10 (a). This inflection point is due to the presence of a non-zero velocity inside the boundary layer, decaying to zero at the boundary layer edge. The inflection point is known to excite two primary modes of significance: the first are travelling waves propagating in the cross-wise direction; and the second is a stationary wave that propagates in the stream-wise direction.

Historically it was believed that the travelling waves were most important in cross-flow transition (Pfenninger and Bacon 1961). This belief was held for a long period of time, with the secondary instability being unclear, with speculation as to whether or not it would be significantly different from K-type and N-type (Reed and Saric 1989).

Poll (1985) studied the development of the stationary mode and found that close to the transition position, a high frequency disturbance appeared. Kohama et al. (1989) found that this high frequency coincided with the appearance of a stream-wise inflection point, see Figure 3.10 (b). This high frequency has since been identified as a secondary wave, triggered by saturation of the stationary mode. As seen from hot-wire probe (see Section 6.3) oscilloscope traces from Poll (1985) in Figure 3.11, the higher frequencies are not modulated by a pre-existing travelling wave as in K-type transition.

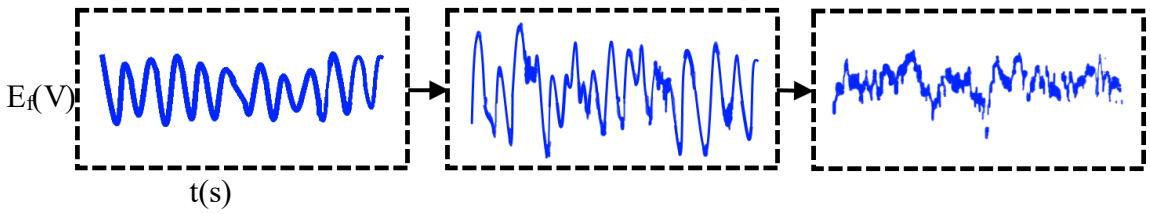

Figure 3.11: Time series showing the development of the fluctuating velocity component during cross-flow transition (Reproduced from Poll (1985)).

The onset of the high frequency has been strongly correlated with stream-wise inflections of the stream-wise velocity ‘u(z)’, in additional to inflections along the wall normal. Because of these modes more strongly correlated with ‘du/dz’ are called type I modes, and modes better correlated with ‘du/dy’ are called type II (White and Saric 2005).

Due to the lack of pre-existing shear gradient along ‘z’, it is speculated that the effect of ‘u(z)’ inflections is less important than ‘u(y)’ which develop in a pre-existing shear layer (i.e. the boundary layer). For sub-critical cross-flow vortices, ‘u(z)’ inflections are present: however, ‘u(y)’ inflections are generally absent.

For this reason it is believed that ‘u(z)’ is a manifestation of the stationary mode and thus is part of the primary instability. The magnitude of ‘du/dz’ grows along with the stationary mode, and once it is large enough to interact with the mean stream-wise profile ‘u(y)’ inflection points appear, exciting high frequency waves.

A systematic diagram of this hypothetical process is shown in Figure 3.12, with some evidence to support it being presented as part of the results of this dissertation (see Section 8.6.2). This is also shown in Kohama et al. (1989) where, a systematic diagram similar to and consistent with Figure 3.12 is provided.

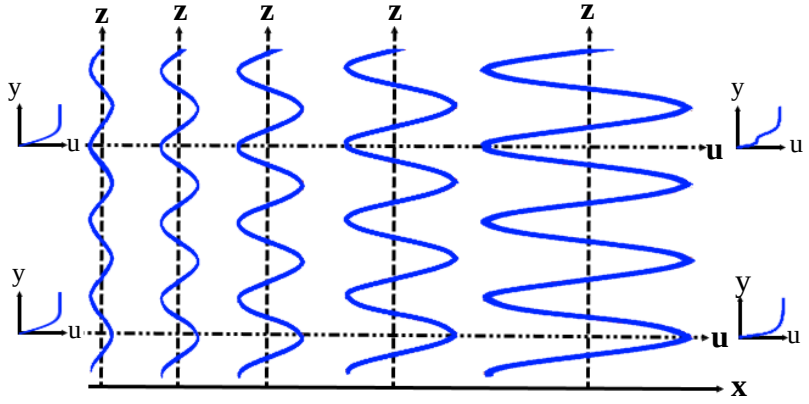

Figure 3.12: Illustration showing growth of a stationary primary wave, and appearance of the inflection point associated with the high frequency secondary modes. The appearance of the inflection point in the stream-wise profile coincides with the trough of the strongly amplified stationary wave. Two of the stream-wise profiles are situated upstream and two are from upstream positions. The difference within each pair, is that one profile is located at the crest of the stationary wave, ‘du/dz’, the other at the trough.

3.2.4 Oblique and Streaky Transition

If the disturbance near-field is very large, it may immediately cause the flow to become non-linear and rapidly transition to a turbulent state. This type of initial disturbance is said to cause transient growth. The term transient comes from the idea of considering the source of the disturbance as an introduced boundary condition, so the formation of the steady-state non-linear near-field can be studied.

The breakdown is associated by the formation of streaks, waves whose wave speed resides in the wall-normal ‘y’ and span-wise ‘z’ plane. Tollmien-Schlichting waves associated with the linear regime by contrast propagate in an xy-plane (i.e. the wave speed is aligned with the free-stream direction ‘x’). These streaks have been associated with the resonance of a pair of oblique waves in the near-field, producing streaks (Berlin 1998). These streaks breakdown as a result of unstable modulation of their structure in the stream-wise direction ‘x’.

Often in the literature transient growth based transition mechanisms are not considered in the context of spectral analysis such as in Sattarzadeh and Franson (2016), due the rapid onset of non-linearities in the flow.

4 Literature Review of Boundary Layer Wall Suction

4.1 Stabilising Suction and 'Over-suction'

4.1.1 History of Stabilising Suction Research

There has been considerable work on the effectiveness of the stabilising effects of wall suction. There are many experimental studies that demonstrate the ability for suction to stabilise disturbances in the flow (Saric and Reed 1986; Sattarzadeh and Fransson 2017; Ellis and Poll. 1996; Maddalon et al. 1989). Experiments by Maddalon et al. (1989) investigated the effectiveness of different suction distributions across the chord. They found that suction near the leading edge had the greatest effect on transition, however, it was also found that weaker suction down-stream further improved transition control.

It can also be shown theoretically by imposing a uniformly distributed suction as a wall boundary condition, when solving the momentum equation across a boundary layer (Schlichting 1979). The main effect of the suction is that it mimics the effect of a stream-wise acceleration on the mean velocity profile across the wall-normal. The modified velocity profile and its derivatives with respect to the wall-normal are used as inputs into a linearised form of the momentum equation, expanded using a fourier series, across the frequency domain (Schlichting 1979). Solving this equation will provide eigenvalues which show the degree of flow stability at different frequencies and wavenumbers (Schlichting 1979). The degree of stability is largely a function of Reynolds number and the shape of the input velocity profile.

4.1.2 History of 'Over-suction' Research

Among one of the earliest known studies on 'over-suction' was performed by Head (Unpublished, reported by Gregory 1961). In this experiment a De Havilland Vampire was modified to accommodate regions of limited suction over its wings, using a suction glove. A suction glove is an outer wing section built on top of the original section designed to accommodate some kind of perforated suction surface, and the systems required to drive it.

Following this was a set of flow visualisation experiments by Meyer (1955) in which smoke measurements were performed inside a transparent tube with radially mounted suction perforations. When in close proximity it was found these suction perforations shed a pair of vortices that link up with vortices from neighbouring perforations to generate a horseshoe vortex that shed unsteady structures down-stream (Gregory 1961).

Further flow visualisation was performed by Goldsmith (1957) where the structures from the smoke visualisation for several different perforation arrangements at different suction rates are sketched and shown. These show some of the effects of perforation spacing, number of perforations, on the transition mechanism through 'over-suction', however, at this stage knowledge of the non-linear regime was only preliminary. Here, transition front locations are identified but few specific details are given to explain the processes behind their formation.

It was found when a single perforation was used the vortices simply convect down-stream (Goldsmith 1957). When using high suction the path of the vortex appeared to meander as it progressed down-stream and caused transition to turbulence when this behaviour was apparent (Goldsmith 1957). For multiple perforations it was again found that the vortices linked up and formed unsteady horseshoe vortices. Limited regions of turbulent flow were noted close to the perforations, At very high suction rates it was found that a standing vortex appeared, and no shedding was apparent (Goldsmith 1957).

Most studies on the physics of discrete suction were performed in the 1950s, such as Goldsmith (1956), where the effect of perforation spacing on the transition mechanism was investigated. However, early studies were limited by the available instrumentation, as hot-wire anemometry was not yet common and techniques such as Laser Doppler Anemometry (LDA) and Particle Image Velocimetry (PIV) had not been developed. The physics has more recently been studied by MacManus and Eaton (1996) and Gaster (1997), where the velocity distributions around isolated suction perforations has been mapped using LDA and hot-wire anemometry respectively. Several structures were identified in these studies, including an inner and outer vortex pair.

Most recently suction has been investigated in the context of streaky and oblique transition mechanisms. Because the discrete suction perforations are a localised source it is feasible that they may generate streaks at high suction rates (Sattarzadeh and Fransson 2017).

4.2 Characteristics of Isolated Suction Perforations

The basic flow physics and structure around an isolated suction perforation was originally mapped qualitatively in experiments by Meyer (1955) and Goldsmith (1957), using flow visualisation techniques (Gregory 1961). From these studies basic flow features around suction perforations were determined, such as two counter-rotating vortices, an elliptical suction envelope, and a region of decelerated flow behind each perforation: these features are shown in Figure 4.1.

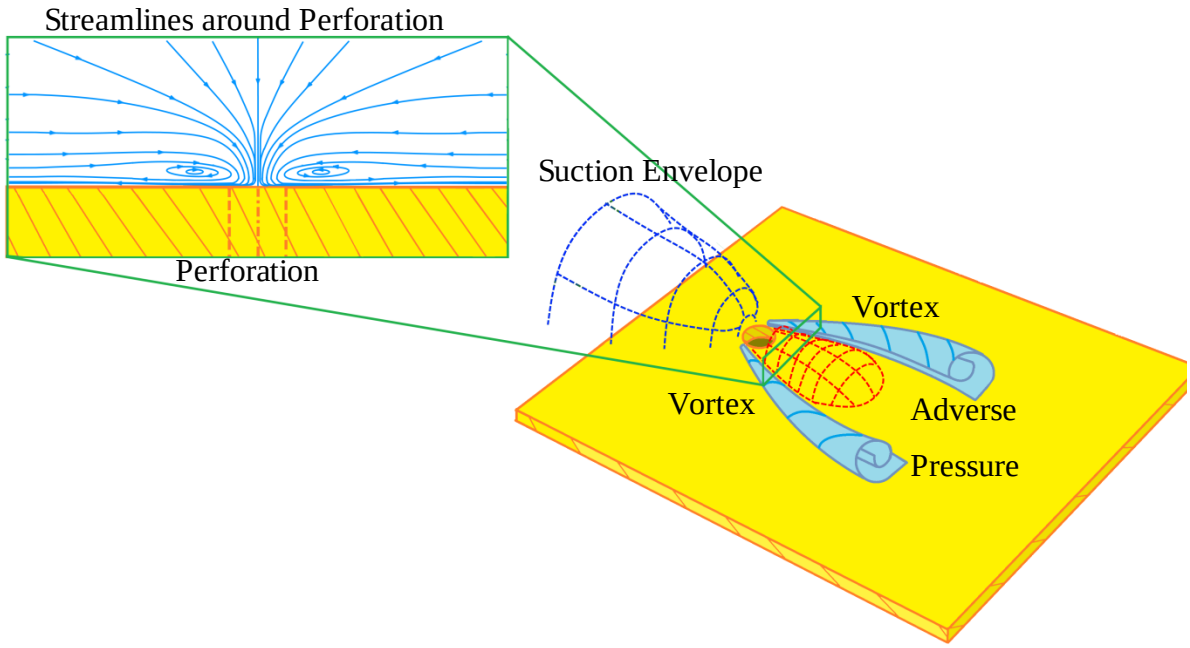

Figure 4.1: Basic flow features around isolated suction perforation, based on MacManus and Eaton (1996).

More quantitative and detailed analysis of the flow structure around isolated suction perforations was performed much later, after significant advances in flow measurement technology. Primarily these studies were performed by MacManus and Eaton (1996; 2000) and Gaster (1997). The former study used Laser Doppler Anemometry (LDA) on 3mm isolated perforations; the latter used hot-wire anemometry on an isolated 1mm perforation. Gaster (1997) focused on very low suction rates, such that flow structures introduced/amplified by the suction were linear and could be calculated using linear stability theory. MacManus and Eaton (1996; 2000) consider much higher suction rates, and were able to measure the velocity profiles behind the vortex cores, where it was found at high suction rates the cores move away from the surface and create local inflection points in the velocity profiles. These inflection points are associated with breakdown into turbulence.

4.3 Characteristics of Suction Perforations Arrays

In this section, key dimensional parameters for over-suction in the context of suction arrays are highlighted. In Section 4.2 some basic flow features around isolated suction perforations were introduced. Here these flow features are placed in the context of suction arrays, and key dimensional parameters found to affect over-suction are discussed. Some more obvious dimensional parameters such as: perforation diameter (‘d’), boundary layer thickness (‘δ’), frequency (‘ω’), wavenumber (‘α’), density (‘ρ’), viscosity (‘μ’), and mean velocity (‘u’), are not discussed in detail.

4.3.1 Effect of Perforation Pattern

Originally discovered by Head (Unpublished, reported by Gregory 1961), changing the orientation of the perforation pattern (‘ε’) can affect the performance of the suction. It was found on a Vampire flight experiment that laminar flow could only be obtained (at high suction rates) by staggering every second row of suction perforations, with respect to the first (Gregory 1961). This was to ensure that successive suction perforations were not in line with the stream-lines over the wing (Gregory 1961). The effect of staggering the perforations has also been studied quantitatively by Reneaux and Blanchard (1992). They found that diamond/triangular arrays exhibit better flow stability characteristics than square arrays. It was also found that there was negligible performance difference between equilateral triangular arrays and isosceles arrays where the base and height of the triangular pattern were equal.

4.3.2 Effect of Perforation Spacing

Goldsmith (1956; 1957) investigated the effect of perforation spacing on transition mechanisms induced directly through suction (i.e. over-suction). Experiments were performed in a circular duct with interchangeable inserts, each consisting of different circumferential distributions of suction perforations (Goldsmith 1956).

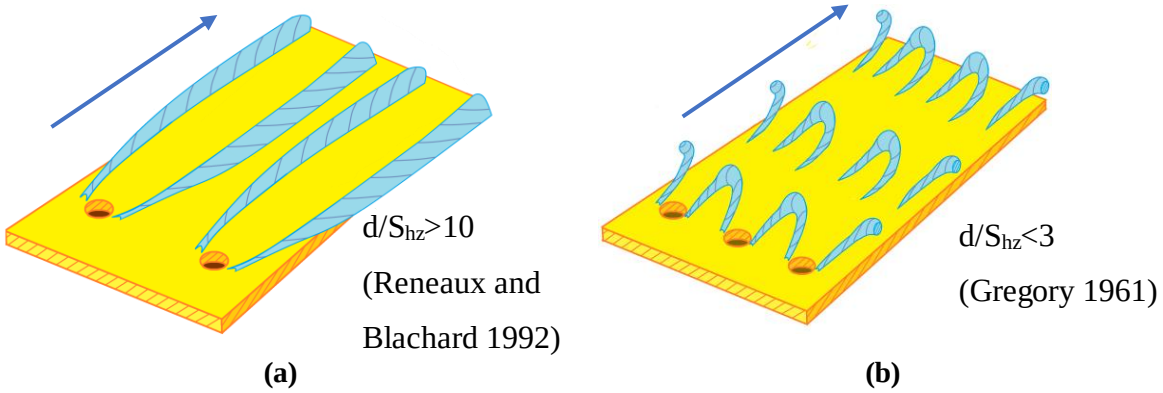

Figure 4.2: Effect of spacing on suction induced vortices: (a) widely spaced holes, (b) closely spaced holes. (Based on flow visualisation results in Goldsmith (1957).

The structure of the flow was also visualised using smoke in a transparent circular duct (Goldsmith 1957). Both of these studies showed that there are two different transition mechanisms of interest which dominate at different perforation spacings ('S_{hz}'). Figure 4.2 shows the effect spacing has on suction induced vortices. In Figure 4.2 (a) the perforation spacing is sufficiently large that the perforations are considered to act in isolation.

For widely spaced perforations, Figure 4.2 (a), each perforation sheds a pair of vortices down-stream which tend to introduce breakdown, as a result of a local inflectional instability produced by the induced stationary wave (MacManus and Eaton 2000). In closely spaced configurations, Figure 4.2 (b), vortices shed from individual perforations tend to link up and shed unsteady streak like structures downstream which grow unstable (Gregory 1961; MacManus and Eaton 2000).

4.3.3 Effect of Wing Sweep

The idea of interaction between wing sweep angle ('Λ') and 'over-suction' was first proposed by Butler (1955). It was suggested that the addition of wing sweep would likely require only a more conservative extension of criteria for unswept suction flows to predict transition (Butler 1955; Goldsmith 1957, p. 38). This was because the global cross-flow from the sweep and the localised cross-flow from the suction were believed to be additive (Butler 1955; Goldsmith 1957, p. 38).

It was speculated that sweep would cause one of the two trailing suction vortices to dominate as a result of interaction between the span-wise pressure gradient introduced by sweep and the local span-wise pressure gradient introduced by the suction perforation (Butler 1955; Goldsmith 1957). It was hypothesised that this would affect critical suction predictions, as criteria would then focus on the dominant vortex which would be stronger than in the unswept case (Butler 1955; Goldsmith 1957). It was further considered by Butler (1955) that resulting co-rotating vortices may be strong enough to prohibit the use of suction at useful suction rates, without causing the vortices to become turbulent prematurely.

The most detailed and significant work on suction in swept wings, with consideration of critical suction and the flow physics pertaining to it, was performed by Messing and Kloker (2010). This study performed a Direct Numerical Simulation (DNS) of individual rows of suction perforations in a swept wing case. It was shown that wing sweep strengthens one of the counter-rotating vortices produced by suction while attenuating the other, as predicted by Butler (1955).

The physics of critical suction is then dictated by the evolution of a series of co-rotating vortices similar to the cross-flow vortices that occur naturally over swept wings. It is suggested that these undergo breakdown through a secondary instability in a similar manner to naturally produced cross-flow vortices (Messing and Kloker 2010). For this reason, Messing and Kloker (2010) questioned the validity of attempting to translate suction criteria from a 2D to a 3D base-flow. Bippes (1999) found that suction was effective at supressing travelling cross-flow and Tollmien-Schlicting waves, but tended to increase the growth rate of pre-existing cross-flow vortices, induced through sweep.

4.3.4 Effect of Pressure Fluctuations due to Common Plenum

Butler (1955) found that if the suction perforations shared a common plenum: small pressure fluctuations between perforations could potentially lead to unsteadiness or even alternating suction and blowing. Butler (1955) found that having an individual isolated plenum for each individual suction perforation solved the problem.

Adhering a porous foam sheet to the back of the suction perforations was found to be an effective alternative solution. Sub-dividing the suction arrays into cells was also recommended by Gregory and Walker (1958).

These experiments were conducted over wings: thus there would be considerable variation in static pressure ('$P_s(x,z)$') across the surface of the wing, compared to a flat plate with no pressure gradient. Atkin(2010) proposed that over a wing there could be local blowing if the surface static pressure dropped below the plenum pressure, as the result of a strong favourable pressure gradient. Here, it is logical that having multiple plenums or forcing a larger pressure drop across the suction surface would mitagate this problem.

It is unclear how these fluctuations were generated, in Section 12B.5, the effect of using porous backing material on the suction, was found to be small. It is feasible that the mechanism observed by Butler (1955) was due to the problem described by Atkin (2010).

4.3.5 List of Dimensional Parameters

To surmise, a list of key dimensional parameters is shown in Equation 4.1, the critical suction velocity ratio '$V_{h,crit}/U_e$' has been shown to depend on these parameters found in the literature.

$$\frac{V_{h,crit}}{U_e} = f\{d, \delta_1, u(y), I_{Tu}, Q_s, A_s, \rho, \mu, \omega, \alpha, L_p, \epsilon, S_{hx}, S_{hz}, \Lambda, P_s(x,z)\} \qquad \textbf{Equation 4.1}$$

Here: $V_{h,crit}$ is critical suction velocity, U_e is edge velocity, d is diameter, δ_1 is displacement thickness, $u(y)$ is stream-wise velocity, I_{Tu} is turbulence intensity, Q_s is volumetric suction rate, A_s is area of applied suction, ρ is density, μ is dynamic viscosity, ω is angular frequency of disturbances, α is wavenumber of disturbances, L_p is stream-wise length of applied suction, ϵ is angle between perforation rows and the stream-wise direction, S_{hx} is the spacing between perforation rows, S_{hz} is the spacing within a row of perforations, Λ is sweep angle, P_s is static pressure. This list of dimensional parameters can be reduced to a set of simpler non-dimensional parameters, which has been done in the literature in an attempt to define a single governing over-suction parameter.

4.4 Existing Critical Suction Criteria (Non-Dimensional Groups)

A number of suction studies have been conducted previously by researchers attempting to provide tools for predicting 'over-suction' for use in the design of suction systems. The results of these studies were sets of non-dimensional groups with critical values of these groups based on experimental data (Ellis and Poll 1996; Reneaux and Blanchard 1992; Goldsmith 1957; MacManus and Eaton 2000; Atkin 2001).

4.4.1 Goldsmith

One of the first criteria developed for critical suction was developed by Goldsmith (1957). It is derived from the relationship between a cross-flow Reynolds number and geometrical parameters of a suction induced elliptical stream tube, where it is assumed that the suction perforations are sufficiently widely spaced to act in isolation from one another. Furthermore, it is assumed that the boundary layer is very thick relative to the height of the sucked stream-tube. The relation that was derived shown in Equation 4.2.

$$\frac{V_{h,crit}}{U_e} = \frac{N_{hx} + N_{hz}}{A_s U_\infty}\left(740\nu\left(\frac{du}{dy}\right)_{y=0}^{-1/3}\right)^{3/2} \qquad \textbf{Equation 4.2}$$

Here '$V_{h,crit}$' is the critical suction velocity, taken as the mean velocity across one perforation; 'N_{hx}' and 'N_{hz}' are the numbers of rows and columns in the suction array respectively; 'A_s' is the 'wetted' area of the suction panel.

This criterion was developed based on a set of experiments which used smoke to visualise the flow around suction peforations located on the wall of a transparent pipe. This allowed stationary modes produced by suction to be followed by the smoke trail, and breakdown is easily distinguished through the visualisation technique (Goldsmith 1957). The effect of important critical parameters was qualitatively measured by adjusting parameters to see how it affected the position of breakdown, as indicated by the smoke.

This critical criterion was also informed by a set of more detailed quantitative measurements, performed in a circular duct with suction perforations arrayed along its interior circumference (Goldsmith 1956). In this experiment interchangeable annulus insert sections with different perforation spacings were used to vary the perforation to determine the effect this had on 'over-suction'.

4.4.2 Reneaux and Blanchard

Based on the suggestion of Pfenninger (1977) and Gregory (1961), Reneaux and Blanchard (1992) proposed a critical suction criteria based on a roughness analogy originally of the form shown in Equation 4.3.

$$\frac{V_{h,crit}}{U_e} = \frac{8}{3\pi}\frac{U_\kappa}{U_e}\left(\frac{\kappa}{\delta_1}\right)^2\left(\frac{\delta_1}{d}\right)^2 \qquad \textbf{Equation 4.3}$$

Where 'κ' is roughness height, and 'Uκ' is the boundary layer edge velocity above the roughness.

This was used to develop the critical suction criterion, shown in Equation 4.4.

$$\frac{V_{h,crit}}{U_e} = \frac{2}{\pi R_{\delta_1}}\left(\frac{\delta_1}{\delta}\right)^2\left[K_0^2\left(\frac{d}{\delta_1}\right)^{-1} - 2K_0K_1 + K_1^2\left(\frac{d}{\delta_1}\right)\right] \qquad \textbf{Equation 4.4}$$

However, values for the added coefficients 'K_0, K_1' were not supplied. Atkin (2001) used information (such as a critical Reynolds number) supplied for the case studied with the smallest perforation sizes, to produce the simplified criterion shown in Equation 4.5.

$$\frac{V_{h,crit}}{U_e} \approx \frac{640}{R_{\delta_1}}\left(\frac{d}{\delta_1}\right)^{-1} \qquad \textbf{Equation 4.5}$$

4.4.3 Ellis and Poll

Ellis and Poll (1996) performed a flat plate experiment with a suction insert, containing large arrays of perforations ranging from 60μm to 2mm. In this experiment the effect of systematically varying critical suction parameters on the transition front location was studied.

To ascertain if the effect of suction was favourable or unfavourable a hot-wire probe was located at a fixed position. The intermittency of the signal was used to determine if the flow was stable or unstable. The free-stream velocity was adjusted until the transition front was located at the probe position. After changing a suction parameter, the amount the velocity that had to be adjusted to find the transition front again, was used to quantify the effect of that parameter on the suction. If the velocity had to be increased, then the parameter had a stabilising effect; if it had to be decreased, then a destabilising effect was produced.

From this experiment two different non-dimensional groups were developed as characteristic criteria: a stabilising, and a destabilising parameter. These criteria were derived using dimensional analysis using previously identified critical suction parameters. The destabilising parameter is defined in Equation 4.6.

$$P_{Destabilising} = \frac{V_{h,crit}}{U_e}\left(\frac{d}{\delta_1}\right)^2 \qquad \textbf{Equation 4.6}$$

This could also be described as a local criterion, as it is based on parameters that induce localised effects, which are generally destabilising. These parameters are related to local perforation geometries and velocities, as this is primarily the difference between the idealised case where suction is assumed to be homogenous and uniform, and no unfavourable effects are introduced through suction. The second is based on stabilising parameters, and can be considered a global criterion, as it is primarily formulated using parameters that are believed to be stabilising: such as the average velocity over the suction surface length 'V_p', and the length over which suction is applied 'L_p'. This stabilising criterion is shown in Equation 4.7.

$$P_{Stabilising} = \frac{V_p L_p}{U_e \delta_1} = \frac{\pi}{4}\frac{V_{h,crit}}{U_e}\frac{L_p}{\delta_1}\left(\frac{d}{S_{hz}}\right)^2 \qquad \textbf{Equation 4.7}$$

Atkin (2001) proposed a method of combining these two criteria into a single citerion. A weakly logarithmic behaviour is observed between the two groups in the experimental data, provided in Ellis and Poll (1996). Atkin (2001) managed to relate the two criteria by assuming a power-law relation, the resulting expression is shown in Equation 4.8.

$$\frac{V_{h,crit}}{U_e} \approx 0.34 \left(\frac{d}{\delta_1}\right)^{-7/4} \left(\frac{L_p}{S_{hz}}\right)^{-1/4} \qquad \textbf{Equation 4.8}$$

4.4.4 Atkin

Atkin (2001a) compared the Ellis and Poll criterion, with the simplified Reneaux and Blanchard criterion. It was noted that the main difference between the two criteria was the absence of a number-of-rows parameter in the Reneaux and Blanchard criterion, and the absence of a Free-stream Reynolds number parameter in the Ellis and Poll criterion. It was proposed that the Ellis and Poll and Reneaux and Blanchard criteria could be unified by adding a free-stream Reynolds number term to the Ellis and Poll criteria, as shown in Equation 4.9.

$$\frac{V_{h,crit}}{U_e} \approx \frac{500}{R_{\delta_1}} \left(\frac{d}{\delta_1}\right)^{-7/4} (N_{hz})^{-1/4} \qquad \textbf{Equation 4.9}$$

It was argued by Atkin (2001a) that the Ellis and Poll criterion demonstrated insensitivity to free-stream Reynolds number as a result of fixing the hot-wire sensor location for transition detection (in their experiments).

In doing this the free-stream velocity had to be adjusted to move the transition front to the sensor location (Ellis and Poll 1996). It was reasoned that if the velocity had to be increased then the suction was having a net stabilising effect on the flow; whereas if velocity needed to be decreased then the suction was producing a net destabilising effect. It was suggested that this inhibits the study of free-stream velocity as an independent parameter.

4.5 Non-dimensional Groups for Presenting Results

For the proposes of presenting reproducable results for comparison with computational work on the same topic, a number of non-dimensional groups are used to present data without contamination due to uncontrolled changes in the experimental test conditions. Non-dimensional groups used for the presentation of experimental data (in this document) are discussed in this section.

4.5.1 Suction Coefficient

Ideally once the critical value has been reached, 'over-suction' will occur in the design being analysed. Often a more basic non-dimensional suction coefficient is used to quantify suction rates. To allow wider interpretation of the 'units' used for suction rate used in this work: Suction Coefficient 'C_s' will be predominately used as a measure of suction rate. Suction Coefficient 'C_s' will be defined in this work as in Schlichting (1979); this definition can be seen in Equation 4.10.

$$C_s = \frac{Q_s}{A_T U_\infty} \qquad \textbf{Equation 4.10}$$

Where A_T is cross-sectional area of the wind-tunnel (at the working section), Q_s is volumetric flowrate through the suction panel, and U_∞ is the free-stream velocity.

4.5.2 Strouhal Number

As part of this study spectral analysis is used extensively, it is therefore useful to define a non-dimensional frequency, here Strouhal number is used as defined in Equation 4.11:

$$St = \frac{fC}{U_e} \qquad \textbf{Equation 4.11}$$

Where U_e is the edge velocity, C is the chord length, and f is the dimensional frequency.

Chord 'C' is used as a length scale instead of perforation diameter 'd' to allow comparisons with other vortex dominated transition studies such as cross-flow transition studies by Serpieri and Kotsonis (2016).

4.5.3 Reynolds Number

Reynolds number is an important non-dimensional group in the study of transition, it governs the stability of different frequencies in the early stages of transition to turbulence.

Three different length scales are notable. The first is displacement thickness, shown in Equation 4.12, which best characterises the onset of transition to turbulence, for a specified pressure distribution.

$$R_{\delta_1} = \frac{\rho U_e \delta_1}{\mu}$$ **Equation 4.12 (White 2011)**

A unit Reynolds number is also defined in Equation 4.13, this is useful for specifying a free-stream condition that is insensitive to drift in density and dynamic viscosity.

$$R_1 = \frac{\rho U_e 1}{\mu}$$ **Equation 4.13**

If the pressure distribution is uniform, then Equation 4.14 applies:

$$\delta_1 \approx \frac{5x}{R_x^{\frac{1}{2}}} = \frac{5x}{(R_1 x)^{\frac{1}{2}}} = 5\sqrt{\frac{x}{R_1}}$$ **Equation 4.14 (White 2011)**

Therefore for a constant R_1, $\delta_1 \propto x$. Thus a R_x parameter can be defined that it equivalent to R_{δ_1} in how it represents the flow physics. This holds for x=C, where C is chord length. Both these forms are shown in Equation 4.15:

$$R_x = \frac{\rho U_e x}{\mu}; \qquad R_C = \frac{\rho U_e C}{\mu}$$ **Equation 4.15**

Where ρ is density, U_e is edge velocity, x is stream-wise position, μ is dynamic viscosity, and δ_1 is the displacement thickness.

Similarly, a Reynolds number can be defined using the wall-normal displacement ‘y’ as a length scale, as shown in Equation 4.16.

$$R_y = \frac{\rho U_e y}{\mu}$$ **Equation 4.16**

4.5.4 Distance from Leading Edge Normalised by Chord

The stream-wise location is normalised by the chord to achieve dimensionless similarity; this is useful when comparing the pressure at a specific location to a measurement, as shown in Equation 4.17.:

$$x/C \qquad \textbf{Equation 4.17}$$

where x is the stream-wise station, and C is the chord.

4.5.5 Non-dimensional wall-normal based on Reynolds number

A non-dimensional wall-normal 'η' can be defined using a ratio of Reynolds numbers. This can be defined as the ratio of 'R_y' to 'R_C'. To prevent this simply being equivalent to 'y/C', the square root of 'R_C' is taken in the ratio shown in Equation 4.18.

$$\eta = \frac{R_y}{\sqrt{R_C}} = y\left(\frac{u_e}{\nu C}\right)^{1/2} \qquad \textbf{Equation 4.18}$$

4.5.6 Pressure Coefficient

Pressure coefficient is effectively a measure of static pressure non-dimensionalised with respect to the ambient pressure and dynamic head. It can be expressed as a ratio of pressures or velocities, as shown in Equation 4.19:

$$C_P = \frac{P_s - P_\infty}{\frac{1}{2}U_\infty{}^2} \approx 1 - \left(\frac{U_e}{U_\infty}\right) \qquad \textbf{Equation 4.19}$$

Where P_s is static pressure, P_∞ is atmospheric pressure, U_∞ is the free-stream velocity, and U_e is the edge velocity.

5 Experimental Design

5.1 Predicted Suction Rates Required Based on Criteria

To design a suction experiment, some idea of the required suction rates was needed. This would allow the purchase of suitable flow meters and a suction pump capable of achieving and measuring the flow-rate, in a suitable range around the threshold of critical suction.

Table 5.1: Critical suction coefficient 'C_s' predictions for a flat plate with: x/C=0.289, R_1=0.9E6, d=0.6mm.

Goldsmith	Reneaux and Blanchard	Ellis and Poll	Atkin
0.018	0.065	0.009	0.008

The criteria specified in Sections 4.4.1 to 4.4.4 were used to specify the performance characteristics of the suction pump and the flowmeter. Thus the flow-rate as predicted by these different 'over-suction' criteria is shown in Table 5.1. Here a perforation size of d=0.6mm is considered.

To determine parameters needed to apply the criteria, such as: boundary layer edge velocity, displacement thickness, Reynolds number, and shear stress maximum, a combined panel method and Falkner-Skan code based on (Cummings et al. 1998) and (Saric and Nafeh 1977) was used. A flat plate pressure distribution was assumed based on the experimental setup shown in Section 6.2.

In comparing the predicted critical suction rates from the different criteria: it can be seen from Table 5.1 that the Reneaux and Blanchard criterion (Equation 4.5) is the least conservative criterion. The values reported from this criterion do not seem reasonable compared to the others, given the significant difference in magnitude.

In contrast, the Ellis and Poll (Equation 4.8) and Atkin (Equation 4.9) are the most conservative criteria and have similar predicted values. The Goldsmith criterion (Equation 4.2) is the next highest estimate of critical suction coefficient 'C_s' after the Reneaux and Blanchard criterion.

Using the Goldsmith criterion, a flowmeter would need to be capable of achieving a suction coefficient of: C_s=0.018 (at R_1=0.9E6). In dimensional units, this is approximately 1000L/min.

5.2 Determining Hole size based on Reynolds Number Scaling

In this study, three perforation sizes were chosen. These three sizes were limited by manufacturing capabilities in relation to the minimum perforation size. However, the range of sizes was not arbitrarily chosen based on the smallest perforation size that could be fabricated. For practical flight conditions, 50-100μm diameter perforations are recommended for cruise altitudes which typically occurs at 30,000ft at a Mach number of 0.8 (Ellis and Poll 1996; Fichter et al. 2005).

In the context of 'over-suction' applied to discrete perforations, flow distortions due to isolated suction perforations should scale most significantly with respect to the boundary layer thickness. For this reason, the ratio between perforation diameter ('d') and displacement thickness ('δ_1') is used in scaling the perforation size from the flight configuration to a laboratory configuration where the free-stream Reynolds number is lower. This dimensionless parameter is shown in Equation 5.1.

$$\frac{d}{\delta_1} \qquad \textbf{Equation 5.1}$$

The displacement thickness is found using a Blasius solution for the specified wind tunnel speed of Mach 0.04 (14m/s) and a cruise speed at Mach 0.8 (274.4m/s). These cases considered the displacement thickness at a station located: 650mm down-stream of the leading edge for the flat plate case; and 500mm (0.1% Chord of an A320) for the flight condition (typical of flight experiments such as Maddalon et al. (1989)). Density and viscosity were determined from altitude tables, for a condition of 30,000ft for cruise conditions, and at sea level where the wind tunnel experiments were performed.

The displacement thickness was found to be 1.55mm for the wind tunnel case (δ_{WTC}), and 0.4mm for the flight condition (δ_{FC}). The non-dimensional parameter shown in Equation 5.1 is applied to the flight and wind tunnel conditions, both diameter and displacement thickness are known for the flight condition but only the displacement thickness is known for the wind tunnel condition. These two ratios are then equated and rearranged as follows to determine a suitable perforation diameter for wind tunnel testing, as shown in Equation 5.2.

$$d_{WTC} = \frac{d_{FC}}{\delta_{FC}}\delta_{WTC} = \frac{0.075}{0.4}1.55\text{mm} = 0.29\text{mm} \qquad \textbf{Equation 5.2}$$

When the experiments were planned, 0.6mm was the smallest perforations size available so it was chosen alongside 1mm and 1.5mm perforations. Despite this is it still useful to contextualise the chosen perforation diameters through comparison with the value determined in Equation 5.2. It is also acknowledged that other non-dimensional groups could be used for scaling the diameter of the suction perforations to laboratory conditions.

For example, a Reynolds number parameter where perforation diameter ('d') and edge velocity ('U_e') could be used. Such a parameter is used as an 'over-suction' criterion in Saric and Reed (1986). Similarly, other critical suction criterion could be used such as those proposed by Ellis and Poll (1996), Goldsmith (1956), Renaux and Blanchard (1992) and Atkin (2001). However, for brevity, the above parameter shown in Equation 5.2 was used for scaling. This is because the distribution of stream-wise velocity ('u') across the boundary layer thickness ('δ_{99}', related to 'δ_1') is known to be important in how both uniform and discrete suction interacts with the flow, whether having a net stabilising or destablising effect (MacManus and Eaton 2000).

6 Experimental Setup and Data Acquisiton

The experiments performed as part of this work were undertaken at the Gaster Wind-Tunnel facility at City, University of London. This facility was chosen because of its large size ($0.91\times0.91\times1.87m^3$ test section), and its low turbulence characteristics. The size of the tunnel is beneficial as larger models will more easily transition to turbulence due to the higher Reynolds number 'R_{δ_1}' resulting from the increase in chord length, 'C'.

6.1 Wind-tunnel Size Specification and Arrangement

A basic outline of the layout of key components of the wind-tunnel is provided, alongside a detailed analysis of the dimensions of the working section. The working section is an interchangable section of the wind-tunnel. There are multiple working sections, each contains a different test model. This facilitates a faster installation of models.

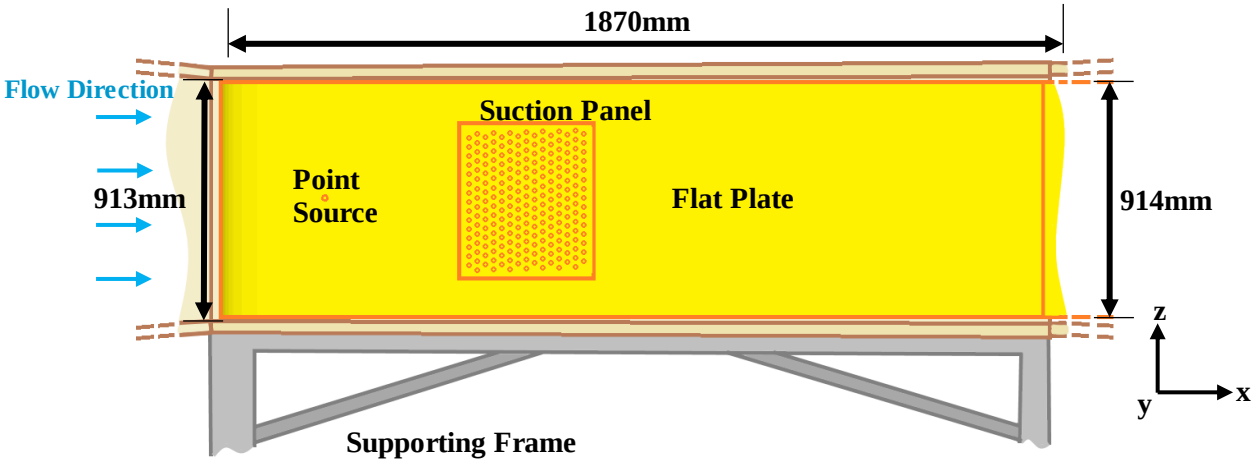

Figure 6.1: Diagram showing elevation view of the working section along with key dimensions and parts of the experimental setup.

An illustration of the side elevation view of the working section is shown in Figure 6.1. The dimensions are also shown, as well as a set of co-ordinate axes. These axes are oriented with respect to the test model, such that: the x-ordinate is oriented with respect to the stream-wise direction, the y-ordinate is oriented with respect to the wall normal, and the z-ordinate is oriented with respect to the span. It is noted that the test section diverges slightly; however, this divergence is small at approximately 1mm. The flat plate model used is also included as a visual aid: it includes a mounted suction panel with an up stream point source. This model is discussed further in Section 6.2.

Figure 6.2 shows a plan view of the same working section shown in Figure 6.1. From the plan view, it can be seen that the divergence of the test section is much greater when compared to the elevation view. In addition, the mounting of the three axes traversing mechanism is shown. Each axis is colour coded to correspond to the closest ordinate of the co-ordinate axis. It can be seen that there is some misalignment between the traversing mechanism and the global co-ordinates. This is due to the traversing mechanism being incorporated into the front wall of the wind tunnel which diverges with respect to the surface of the flat plate model. This is compensated by using a laser displacement sensor, the procedure for which is discussed further in Section A.3.

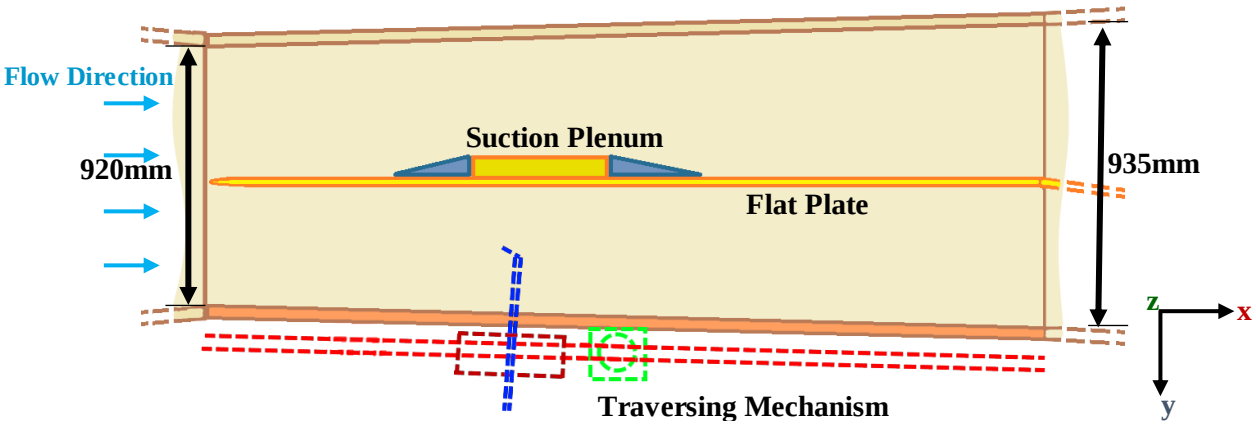

Figure 6.2: Plan view of test section showing dimensions, and traverse arrangement. Colours of the illustrated traversing mechanism represent different closest corresponding spatial co-ordinate axis.

6.2 Flat Plate Model

For all experiments a 2.25m long flat plate was used, all dimensions except for the leading edge are provided in Figure 6.3 (b). Figure 6.3 (a) shows an illustrative diagram of the different parts of the flat plate model. The key features of this model are: the asymmetric elliptical leading edge; the suction panel, and plenum; and the point exciter.

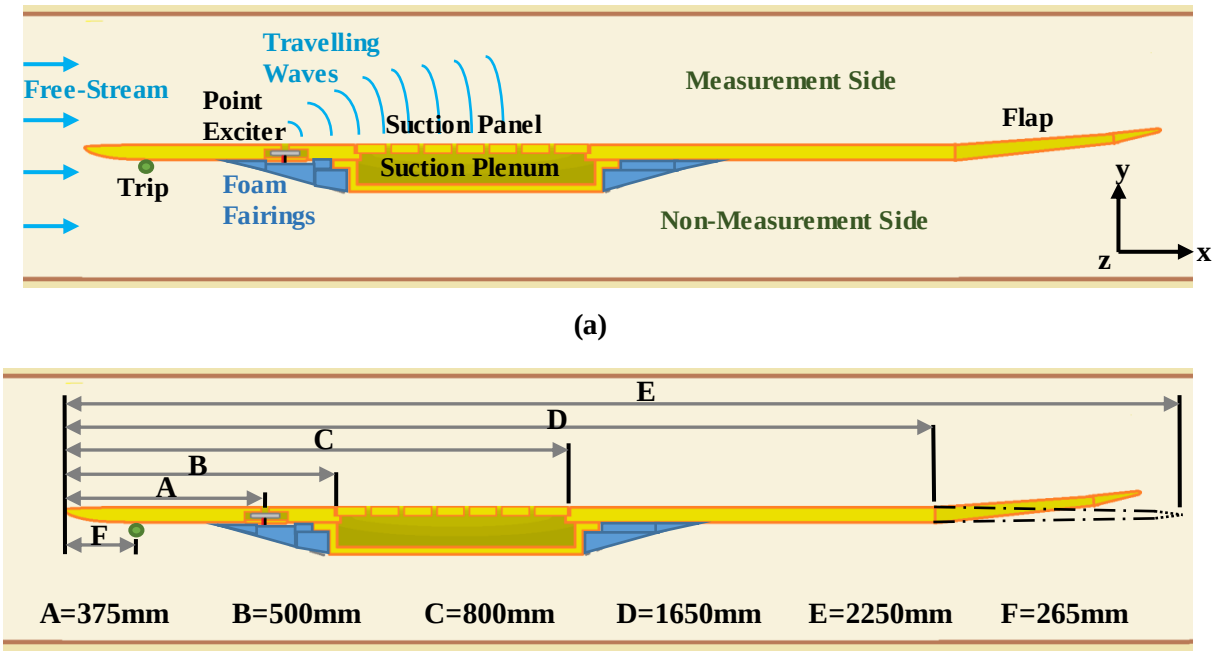

Figure 6.3: Description and relevant dimensions of the flat plate model used in this study.

The leading edge was designed to minimise receptivity at the joint between the leading edge and the rest of the model. The leading edge was made asymmetrical to further increase the ratio between the elliptical major and minor axis for the measurement side.

The suction panel was an insert panel that contained the array of suction perforations. The panel was bolted to the suction plenum with sufficient gaskets to prevent leakage. A gap was allowed at the interface between the suction panel and the rest of the plate to allow the use of filler material. This helps to reduce the severity of steps between the panel and the rest of the plate, as the filler provides a smooth continuous surface between the panel and the rest of the plate.

The suction plenum is used to apply a pressure drop across the suction panel, it is airtight, and protrudes 20mm out of the model on the non-measurement side. Fairings are used to reduce the blockage and re-circulation regions due to the plenum. The plenum itself is connected to three 8mm inner diameter pipes that connect to the flow-meter and suction pump.

A flap was mounted on the rear of the plate, the flap had two elements: the down-stream element was mainly used to adjust the stagnation point, whereas the up-stream element was used to adjust the pressure distribution.

It can be seen that a 3mm trip was placed on the non-measurement side of the model, this was to force to the boundary layer to a turbulent state before it reached the protruding suction plenum to prevent/reduce separation. Foam Fairings were used to reduce the blockage resulting from the protruding suction plenum.

6.2.1 Suction Array Details

A diagram of the suction array arrangement is shown in Figure 6.4 (a). The perforations size were chosen based on the smallest sizes available for manufacture. How this compares to perforations correctly scaled for testing at this wind-tunnel facility is discussed in Section 5.

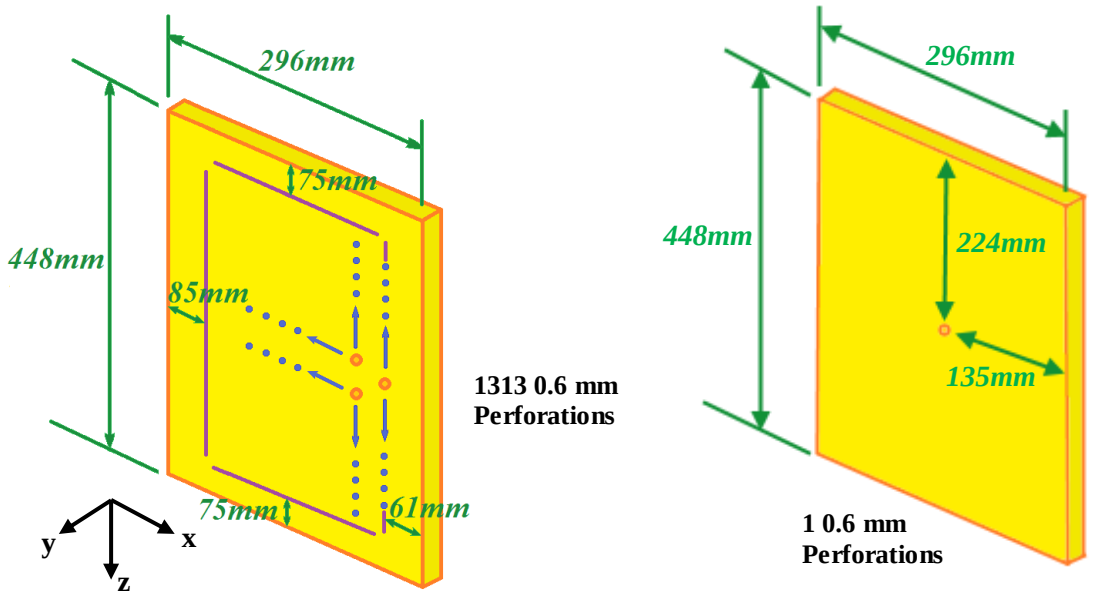

(a) **(b)**

Figure 6.4: Illustration of the arrangement of the perforations on the suction panel. A total of 1313 suction perforations were used.

The suction array pattern was chosen based on work in the literature by Renaux and Blanchard (1992) and Gregory (1961). From these works it was decided to use a 10 perforation diameters spacing between suction perforations within a row. Rows were similary 10 perforation diameters apart. This was to ensure any over-suction would occur in the widely spaced configuration (see Section 4.3.2). Some test cases only used a single surction perforation, the layout for this arrangement is shown in Figure 6.4 (b).

6.2.2 Point Exciter

Figure 6.3 shows a point exciter mounted upstream of the suction panel (a diagram of the mounting arrangement is shown in Figure 6.5). This point exciter was used to selectively set an initial disturbance amplitude for traveling waves in the boundary layer. This allows the change in spatial growth as specified frequencies to be more easily studied. Furthermore, this is the most convenient way of pre-scribing an initial transition front location that has a clearly defined linear regime stage upstream. This method not a novel means of excitation and has been used in studies such as Gaster and Grant (1975).

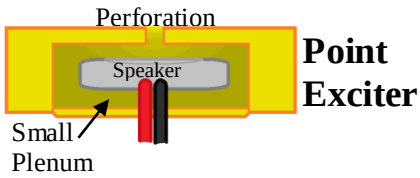

Figure 6.5: Detailed view of Point Exciter arrangement.

An alternative method of achieving the same effect would be to use a vibrating ribbon, mounted upstream. The main advantage of a vibrating ribbon, is that the induced travelling waves are two-dimensional, whereas with a point exciter the waves are slightly three dimensional. The main implication of this, is that a two-dimensional linear stability calculation is insufficient for modelling the point exciter, where it would be sufficient for a vibrating ribbon. This reduces computational cost and difficulty of modelling the experiment computationally.

There is some evidence to suggest that use of a point exciter over a vibrating ribbon does not greatly alter the physical transition mechanism observed. Results in Section 8.2 for that of a N-type transition (with no suction) compare well with spectra presented by Kachanov and Levchenko (1983), shown in Section 3.2.2.

6.3 Hot-wire Anemometry Instrumentation

All experiments conducted by the author in the context of this study used hot-wire anemometry as the primary measurement technique. A DISA M unit was used as a control circuit, with a variety of Dantec probes used for measurements. The basic geometry of the probe is shown in Figure 6.6 (a).

In this measurement technique a 5μm diameter wire, usually made from tungsten, is suspended from a pair of prongs (Perry 1982). The wire is heated either by: a constant current source, or using a feedback circuit which maintains constant temperature (Perry 1982).

As the wires typically have very low resistance (usually less than 5Ω), they generate considerable heat when powered. When air flows over the sensor, heat is convected away from the wire. The amount of heat convected away primarily depends on the velocity of the air flowing over the wire. If the wire is heated by a constant current source, then the voltage drop across the wire will change with the resistance of the sensor as heat is convected away from it. This can be used to define a relationship between velocity and voltage drop across the wire.

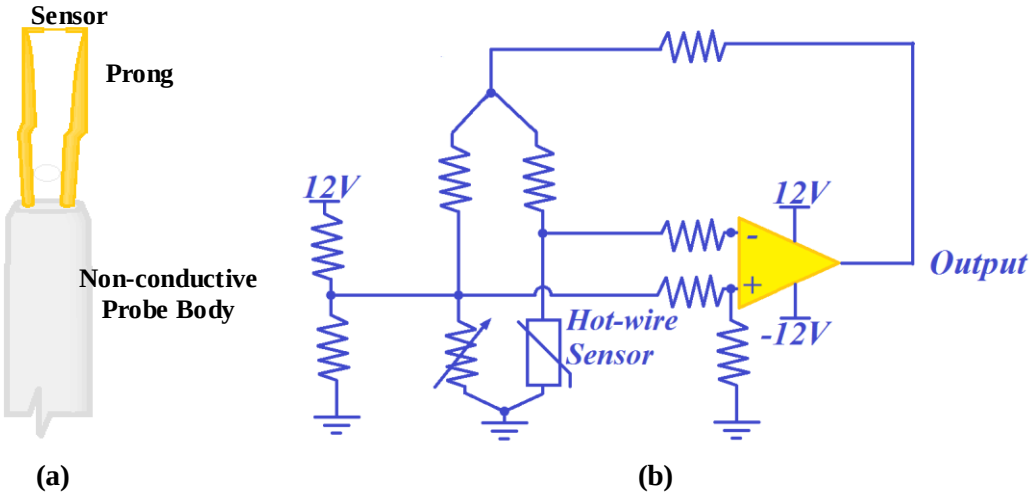

Figure 6.6: Basic probe geometry (a) and circuit (b) used for constant temperature(resistance) hot-wire measurement.

A hot-wire anemometry circuit design is illustrated in Figure 6.6 (b). These circuits employ a Wheatstone bridge, with a bias voltage connected as an input to one of the arms of bridge. The two sides of the bridge are used as inputs into a differential operational amplifier. The amplifier ensures its output voltage will change such that the resistance of the hot-wire sensor is kept constant. The resistance of the wire is proportional to its temperature, thus the circuit maintains the sensor at a constant temperature.

6.3.1 Hot-wire System

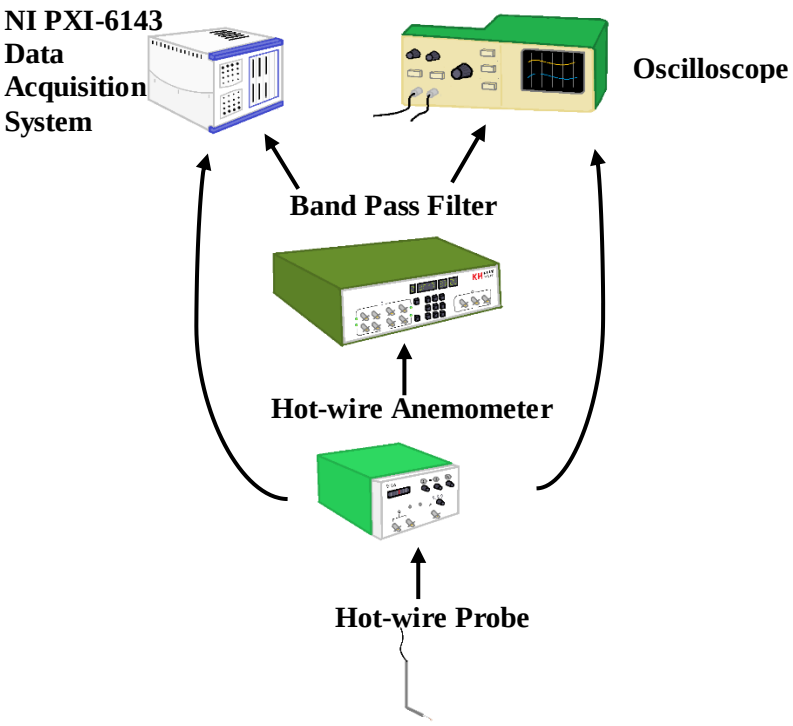

Figure 6.7: Diagram showing flow of information from the Hot-Wire probe to the Data Acquisition System.

The hot-wire system consisted of a hot-wire probe mounted in a Dantec probe holder; this probe holder was connected to a DISA type 55 M hot-wire anemometer. The voltage output from the anemometer was split using a T-connector: one channel was connected directly to the NI PXI 6143 Data Acquisition System, the second was passed through a Krohn-Hite band-pass filter. This signal was filtered between 2Hz and 5000Hz (St=0.3-750), using a Butterworth type filter. A gain of 33.33 was used in the experiments. The filtered signal was then connected to NI PXI 6143 Data Acquisition System and an oscilloscope using a T-connector.

6.3.2 Hot-wire Calibration

As the hot-wire system measures output voltage of the anemometer directly, a method of calibrating the hot-wire voltage against velocity is required.

The hot-wire system measures velocity through the ability of the anemometer circuit to maintain a constant temperature. Therefore, if the ambient temperature changes during a set of measurements, the measurement error will grow proportionally to the temperature drift. In the presented experiments this drift was about 1°C.

As it is difficult to derive a calibration law that accounts for drift in ambient temperature, a law which assumes a fixed temperature was used when relating voltage to temperature. This law is based on a simple relation between a potential flow model, and a heat transfer model with a simplified convective heat flux model around the wire (Perry 1982, p.12). This law is King's law, shown in Equation 6.1, which assumes the following form for this ideal case (King 1914a; b).

$$E_m^2 = A_c + B_c u_m^{n_c} \qquad \textbf{Equation 6.1}$$

Here u_m is the mean velocity; E_m is the mean voltage; and A_c, B_c, and n_c are calibration coefficients.

The hot-wire system needs another instrument which accurately measures velocity to calibrate against. In these experiments a Pitot-static tube was used, as these instruments exhibit a weaker dependency on temperature, through variation in density as seen in Equation 6.2. This is derived from Bernoulli's equation, where it is noted that pressure will vary to some degree with temperature (White 2011, p.175). Assuming constant pressure should be a reasonable approximation, as the manufacturer of the pressure transducer state that the calibration will hold between a temperature range of -18°C to 65°C (Setra 2017).

$$U_\infty = \sqrt{\frac{2 \times \{P_T - P_s\}}{\rho(T)}} \qquad \textbf{Equation 6.2}$$

Where P_T is total pressure, P_s is static pressure, ρ is density and T is temperature.

6.3.3 Probe Location

In hot-wire experiments, it important that the hot-wire probe move with respect to the surface of the model, hence-forth referred to as the wall. The wall is the datum from which many important length scales in the study of boundary layers are defined. Locating the wall can be difficult, as the location of the wall must be determined through manual alignment. There are different procedures for determining the location of the wall: in this section, methods used within this study are outlined.

Firstly, the probe was positioned within the boundary layer. From theory (Schlichting 1979) and from prior experience, an approximate value of the boundary layer thickness can be estimated. Based on this estimate the probe can be moved inside the boundary layer by checking the probe position visually. After this more accurate methods locating the wall can be employed.

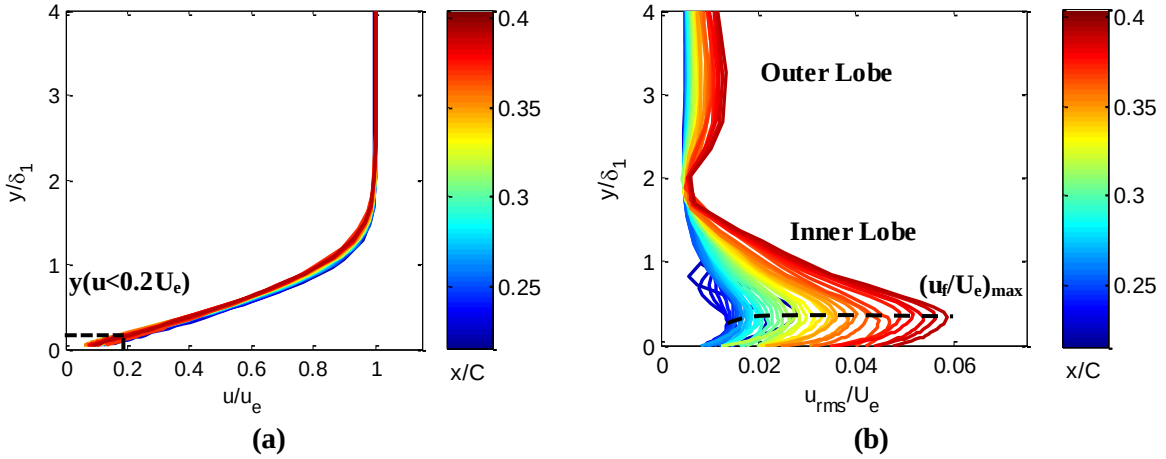

Figure 6.8: Illustration of wall allignment criteria: (a) shows the mean velocity profile, and (b) shows the RMS of velocity profile.

Once inside the boundary layer the wall was approached in step sizes that are half of the estimated distance from the wall. Two criteria were used to decide if the hot-wire probe was sufficiently close to the wall: firstly the hot-wire probe is moved inward until a fixed percentage of the free-stream velocity is measured by the sensor, as shown in Figure 6.8 (a). As the flow feature closest to the wall is the inner lobe of a velocity wave: ideally the probe should be moved sufficiently inward such that it is past the maximum amplitude of the inner lobe highlighted in Figure 6.8 (b). The amplitude of the velocity wave was measured using an oscilloscope; typically using a point source to specify the initial amplitude of the velocity wave.

6.3.4 Probe Types

In this study, measurement of two velocity components was required, this can be difficult as individual hot-wire probes have only weak directional sensitivity. A probe is most sensitive to flow in the plane normal to the sensor. However, there is some sensitivity from other directions including the traverse direction, i.e.: along the sensor. The directional sensitivity of a hot-wire probe is usually modelled as a modified Cosine function, where the maximum is at zero degrees, the sensitivity decreases with increasing angle between the normal of the sensor and the direction of the flow (Perry 1982).

Figure 6.9: Straight and slanted hot-wire probe configurations.

However, the slight directional sensitivity that is present is sufficient to resolve specific velocity components with reasonable accuracy if a second off-axis probe is used. Using simple trigonometry, the velocities from the two sensors can be used to determine the stream-wise and span-wise velocity components.

In this study, two separate runs were performed with different hot-wire probe configurations, illustrated in Figure 6.9. The first run of the pair was a standard set of measurements using a straight hot-wire probe. Afterwards, a 45° slanted hot-wire was used. Care was taken to realign it to the same position as the straight wire. It is noted that there was increased difficulty in performing the near-wall alignment (See Section 6.3.3). This slanted hot-wire probe was used to perform measurements for the purpose of resolving the span-wise velocity/wall normal profile ‘w(y)’, to investigate how strongly correlated this field was with the suction distribution.

The procedure for using the slanted and straight hot-wire probes for resolving the ‘u’ and ‘w’ mean velocity components is outlined as follows.

First a set of measurements is performed using the straight probe to find the ‘u’ component (see Section 6.3.1). Afterwards the slanted probe is placed in the probe holder, and the hot-wire system is re-calibrated.

To calibrate the slanted probe, the sensor must be oriented perpendicular to the direction of the free-stream flow, as seen in Figure 6.10. To accomplish this: the probe holder is rotated 45 degrees. After performing a calibration (See Section 6.3.1), the probe is rotated back. A calibration should be performed before the start of a set of automated measurements. Care should be taken to ensure it returns to the same position as was used in the straight wire case. A mismatch between the two will introduce error into the measurement. The angle was checked using a protractor with 0.5 degree increments.

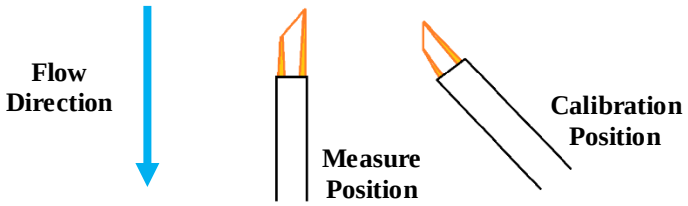

Figure 6.10: Slanted wire arrangement during measurement and during calibration.

The probe is then aligned with the wall, using a near-wall alignment procedure similar to the one described in Section 6.3.3. However, the procedure differs in that greater care is required as the measured velocities will be reduced slightly.

Once measurements have been taken with both probes, the span-wise velocity component ‘w’ can be reconstructed using the trigonometric relation shown in Equation 6.3.

$$w = \{u_{Hw45} - u_{Hw0} \times \cos(45)\} \times \cos(45) \qquad \textbf{Equation 6.3}$$

Here u_{Hw45} is the slanted wire velocity determined from the 45 degree position, u_{Hw0} is the normal wire velocity.

To define this relation, the velocity measured by the straight probe is split into two orthogonal co-ordinates. This is done simply by multiplying the straight probe velocity by the sine and cosine of the slanted probe, as illustrated in Figure 6.11. As the slanted wire is at 45 degrees it is equally sensitive to flow in the x and z directions (see Perry 1982), contamination from velocity component in the x-direction (u) must be removed from the slanted wire. This is achieved by subtracting u_{Hw0}Sin45 from u_{Hw45}. The result can then be transformed about 45 degrees to work out the velocity (w) in the z-direction.

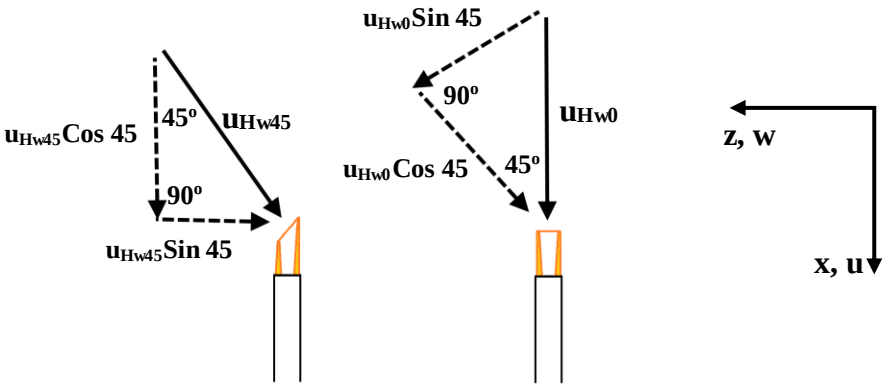

Figure 6.11: Illustration of angle transformations used in Equation 6.3

This method does not account for transverse flow along the sensor. This will cause some small error in the determined 'w(y)' velocity, it is believed that this error is acceptable as the transverse flow is typically ignored in the literature when determining 'w(y)' components from two hot-wire probes (Perry 1982).

6.3.5 Loss of Phase Information

In hot-wire anemometry single point measurements (when using a single probe) are taken at different positions across the flow-field to map the structure of the flow-field. Each measurement is performed sequentially with a random time delay between each measurement. The implication of this is that there is a random phase change in the hot-wire signal between any pair of measurement records performed at times 't_1, t_2'.

Table 6.1 shows a comparison of the phase change ('ωt_1 to ωt_2') between measurement locations for a hypothetical hot-wire, and Particle Image Velocimetry (PIV) scan. Because, when measuring with PIV, all measurements are taken at the same time, the phase of the signal is representative of the physical flow field without any corrections. It can be seen in Table 6.1, that for different positions the same temporal phase component 'ωt' is present, this is because time is constant.

Table 6.1: Illustration of loss in phase information when performing sequential measurements.

General form:	$u_f(x, y, z, t) = \lvert u_f \rvert e^{-i(k_x x + k_y y + k_z z + \omega t)}$
First PIV measurement point (x_1,y,z,t):	$u_f(x_1, y, z, t) = \lvert u_f \rvert e^{-i(k_x x_1 + k_y y + k_z z + \omega t)}$
Second PIV measurement point (x_2,y,z,t)	$u_f(x_2, y, z, t) = \lvert u_f \rvert e^{-i(k_x x_2 + k_y y + k_z z + \omega t)}$
First hot-wire measurement point (x_1,y,z,t_1):	$u_f(x_1, y, z, t_1) = \lvert u_f \rvert e^{-i(k_x x_1 + k_y y + k_z z + \omega t_1)}$
Second hot-wire measurement point (x_2,y,z,t_2):	$u_f(x_2, y, z, t_2) = \lvert u_f \rvert e^{-i(k_x x_2 + k_y y + k_z z + \omega t_2)}$

Here the signal of the fluctuating wave is shown represented using Euler's formula. There is an amplitude '$|u_f|$' and phase angle component '$k_x x + k_y y + k_z z + \omega t$'. The amplitude component is simply the maximum value of the wave. The phase angle (shown as the exponent) describes the periodicity of the wave and varies in three dimensions of space 'x y, z' and one of time 't'. Thus it requires three spatial wavenumbers 'k_x, k_y, k_z', and a frequency 'ω' to be described mathematically (see Table 6.1).

It is possible to reconstruct the phase, and correct this problem. However, reference signals at the frequencies of interest, located at a fixed spatial position, must be acquired simultaneously with the hot-wire signal.

Because the reference is at a fixed position, spatial phase '$k_x x + k_y y + k_z z$' should be constant for all measurements of the reference signal. As phase can again only be determined as a lumped sum of all spatial and temporal components 'ωt', fixing the position will cause the total phase to only vary with time. If the phase angle of the reference signal is then subtracted from the phase of the hot-wire signal, where neither space nor time are fixed, then the temporal phase variation is removed. This is shown using Euler's formula in Table 6.2.

Table 6.2: Simple method of determining correct phase angle of hot-wire signal .

For fixed point sequential measurements:	$u_f(0,0,0,t_1) = \lvert u_f \rvert e^{-i(\omega t_1)}$
The correct hot-wire phase can be determined as:	$u_f(x_1, y, z, t_1) = \lvert u_f \rvert \left\{ e^{-i(k_x x_1 + k_y y + k_z z + \omega t_1)} e^{+i(\omega t_1)} \right\}$
This forces all hot-wire measurements to have a constant temporal phase angle of zero:	$u_f(x_1, y, z, t_1) = \lvert u_f \rvert e^{-i(k_x x_1 + k_y y + k_z z)}$

If the resulting phase is used to reconstruct the hot-wire signal, using the correct amplitudes '$|u_f|$', then time 't' will be physically consistent across all measurement locations. Plotting the data will correctly display the variation in the instantaneous velocity field '$u_f(x,y,z,t)$' across all stations. The Reference signal used in these experiments was obtained using a point exciter described in Section 6.2. This procedure was used to obtain the figures shown in Section 8.1.2.

6.3.6 Sources of Noise/Errors

A significant issue when conducting hot-wire measurements is the effect of electronic noise on the output signal from the anemometer. This must be distinguished from background turbulence in the tunnel, and notable flow features.

Three simple methods have been found to be effective at identifying electronic noise. The first is to check if the intensity of the noise is affected by the speed of the wind-tunnel (i.e. free-stream Reynolds number): if it is unaffected by changes in speed then it is likely electronic noise. Noise from the motor driving the fan of the wind-tunnel is also a possibility if it is inadequately shielded and is in close proximity to the anemometer and other data acquisition equipment.

The second method for identifying electronic noise is observing the frequency of the noise: if it is at high frequency (kHz to MHz) it is likely noise induced by background electrical fields (largely from switched mode power supplies). If the noise is a harmonic of 50Hz it is likely mains-pickup noise, resulting from grounding noise passed through power supplies.

The third way of identifying electronic noise is to investigate the spatial variation of the signal in question, particularly in the y-normal direction. If the signal is attenuated close to the surface of the model then it is affected by the no-slip condition at the wall, and must be related to the flow.

Control of background noise is achieved through a combination of grounding techniques, shielding techniques, and filtering of the acquired signals. Isolating the grounds of older instruments (that use older types of transformer rectifier circuits) from the grounds of newer instruments (powered by switched mode power supplies) has been found to reduce common mode noise. As most measurements are acquired between 0.002-5kHz, higher frequencies can be removed by using a low pass filter.

6.4 Suction System Instrumentation

The suction system used in this study consisted of a number of components, as illustrated in Figure 6.12. The first of note is the suction plenum connected to the underside of the plate containing the suction array, see Section 6.2. This suction plenum was connected to a set of pipes which connected to a volumetric flow-meter. This flow-meter was used to determine suction coefficient 'C_s' from its measured volumetric flow-rate 'Q_s' and the wind-tunnel free-stream velocity 'u_∞'. The flow-meter was connected via pipeline to a suction pump whose purpose was to create a static pressure 'P_s' drop to atmospheric values (P_s=P_∞).

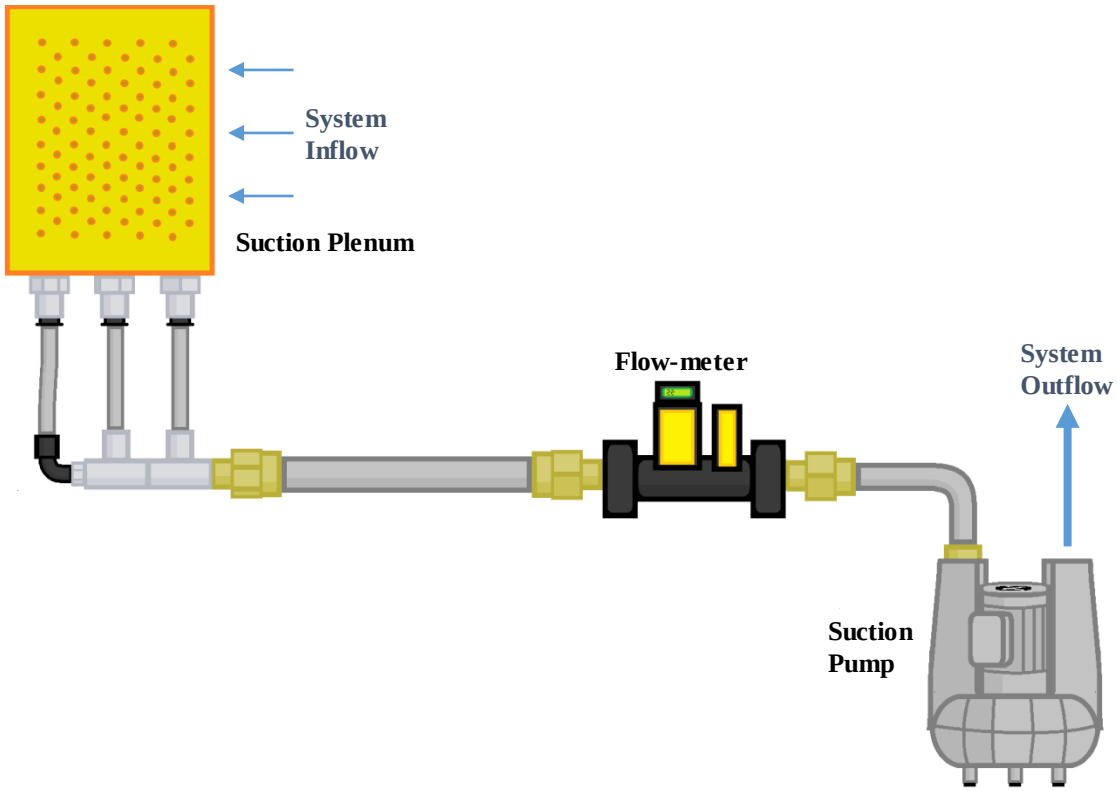

Figure 6.12: Layout of suction system arrangement, including suction plenum, flow meter, and suction pump.

6.4.1 Flow-meter

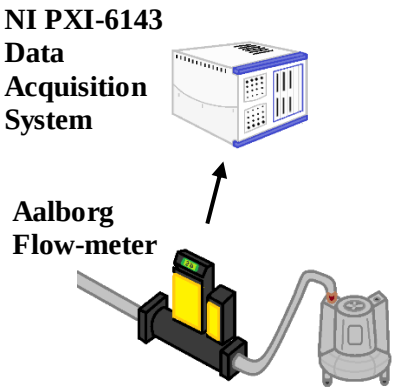

Figure 6.13: Diagram showing flow of information from the flow-meter to the Data Acquisition System.

The suction volumetric flow rate was measured using an Aalborg GFC mass flow controller Aalborg (2014). As shown in Figure 6.13, this was an analogue instrument that connected directly to the data acquisition system. The suction rate scaled linearly with voltage on the output, and the suction rate was displayed on the screen of the unit, allowing for a calibration.

6.4.2 Suction Pump

A Becker SV 5.130/2 suction pump was used in these experiments. It had a power rating of 700W (Becker 2015). Its maximum volume flow rate with no external losses was 1250L/min ($0.021 m^3/s$) and its maximum pressure rise was 375mbar (Becker 2015). The basic arrangement for the suction pump is shown in Figure 6.14.

The suction pump was placed in a wooden box with acoustic lining to help maintain safe acoustic noise levels in the laboratory. This created an issue, as it caused the suction pump to heat up during operation. To combat this issue holes to allow natural convection through the box were added, and four 230Vac computer fans were mounted axially to increase the airflow through the wooden box. Additionally, the air-conditioning was switched on, to allow hot-air to be extracted from the room.

Refer to Appendix A. for the pump sizing procedure, in which a pressure loss analysis was performed to determine the desired pump characteristics for a design suction flow-rate.

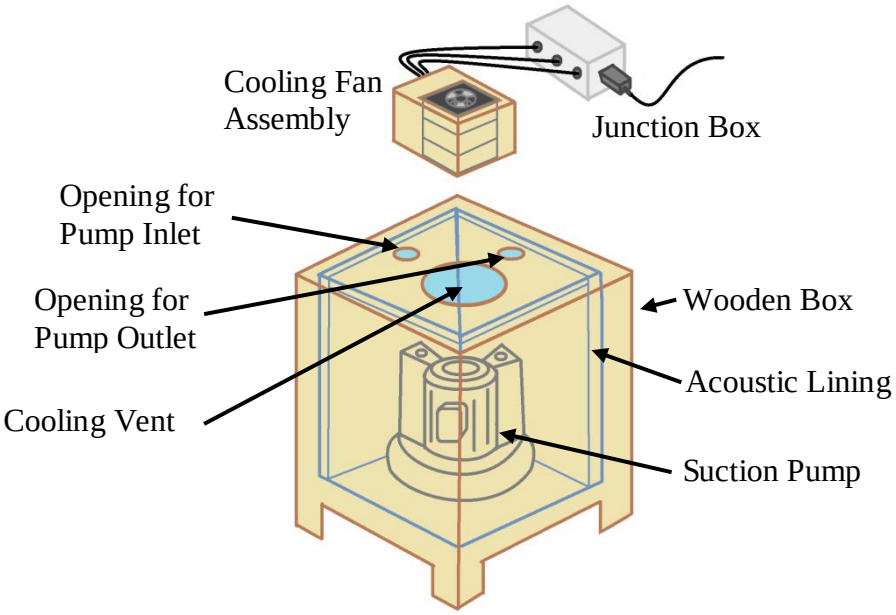

Figure 6.14: Suction pump layout, including acoustic liner box, and cooling fans.

With these measures in place the pump would still over-heat if ran for long enough. Upon overheating the pump would automatically switch off, using an internal bimetallic switch. The wind-tunnel control code was altered to detect if the pump sudden stopped by monitoring the flow-rate through the suction system.

Additionally, the temperature of the suction pump was monitored using a thermistor circuit, the thermistor accuracy was to within ±1^{o}C of a multimeter mounted thermocouple. The uncertainty of this instrument was not critical as it was not used for measurements, simply as a threshold for a control circuit to switch on and off the suction pump from the wind-tunnel control code. This way any disruptions in measurements could be controlled.

6.5 Other Instrumentation

6.5.1 Pressure and Temperature

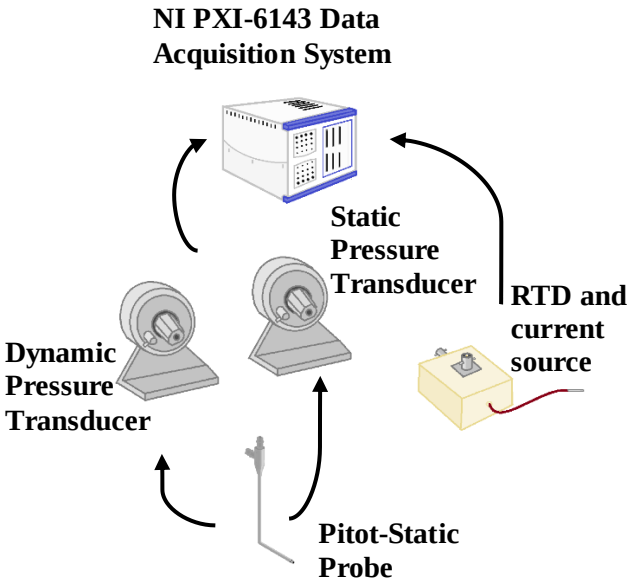

Figure 6.15: Diagram showing flow of information from the Pitot-Static Probe and RTD sensor to the Data Acquisition System.

To measure the free-stream velocity 'u_∞', instruments for measuring atmospheric conditions were required. Thus, instruments were needed to measure the dynamic pressure, barometric pressure, and temperature. These instruments were used to determine the density 'ρ' and dynamic viscosity 'μ' which allowed the free-stream velocity to be calculated from the dynamic pressure.

A pitot static probe was mounted on the roof of the tunnel, and the two outputs were connected to a Setra 239 instrument to measure the dynamic pressure. The static pressure line was split using a T-connector which allowed it to be directly measured by a Setra 270 instrument to determine the barometric pressure. A Resistance Temperature Device (RTD), powered by a current source, was used to measure the temperature using a PT1000 probe. All three instruments were connected back to the NI PXI-6143 Data Acquisition System.

6.5.2 Laser Displacement System

A laser sensor was purchased and mounted on the saddle of the x'-traverse. The idea was to correct for divergence between the x'z'-axes and the surface of the model; this is illustrated in Figure 6.16. Here, it can be seen that the tunnel walls are divergent, it can be also seen that the traversing mechanism is mounted on one of the walls. If the flat plate is mounted with zero angle of attack, then its surface will not be parallel with the x'-axis of the traversing mechanism.

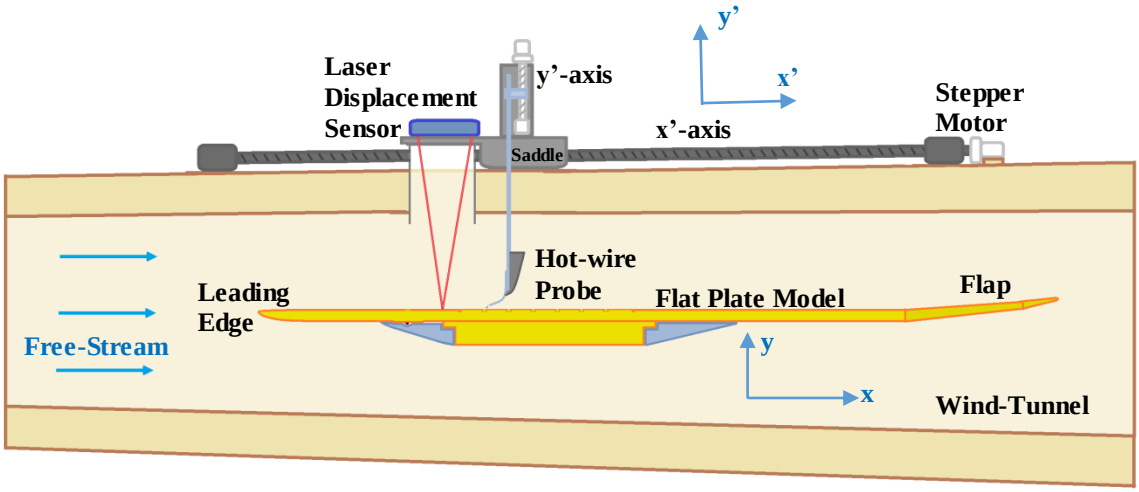

Figure 6.16: Illustration of laser displacement system and its operation: showing the overall mounting of system with respect to traversing mechanism and wind-tunnel.

During the hot-wire alignment procedure (see Section 6.3.3), the experimenter attempts to move the hot-wire probe as close to the wall as possible such that any significant flow structures in the inner boundary layer are captured, but not so close as to break a probe. Ideally this alignment should apply to all hot-wire measurement stations, however, because of the previously mentioned divergence: there will be drift in the wall normal direction.

The laser compensates for this drift (between x' and x; and z' and z), such that measurements are effectively taken parallel to the wall (xyz-coordinates). It does this by determining a new position in traverse co-ordinates (x'y'z'-coordinates) that will effectively result in a movement in wall-aligned datum co-ordinates (xyz) being satisfied.

The laser sensor itself was a OptoNCDT-1750 with an accuracy of ±3µm, over a range of 50mm.

6.6 Post Processing Procedure

Before useful information from the experimental data can be presented, the data must be processed. This involves converting the hot-wire data from a voltage to a velocity, using pre-determined calibration coefficients; and performing a Fourier transform on the converted signal.

6.6.1 Converting Hot-Wire Voltage to Velocity

As the hot-wire system is an analog instrument, velocity measurements were acquired as a voltage signal. Thus, measurements needed to be converted to velocity before further analysis could be performed. This was achieved using Kings law and its appropriate coefficients, obtained through a calibration procedure performed before taking measurements (see Section 6.3.1). The mean velocity can be easily obtained by taking the mean of the hot-wire signal, once it has been converted to velocity.

As the magnitude of velocity fluctuations in laminar flows is very small in comparison to the magnitude of the mean velocity, it was desirable to amplify these fluctuations- to improve the signal to noise ratio from the hot-wire anemometer.

However, the mean of the hot-wire signal must be removed, to prevent the signal from saturating when acquired by the analog to digital converter which has a limited input range of 0-5V. To achieve this, the hot-wire signal was band pass filtered (between 2Hz and 5000Hz). As the filtered signal had been amplified, a modified form of King's law was needed to convert it to a usable velocity. Equation 6.7, determined through differentiation of King's law (Perry 1982; Gaster 2015). King's law is repeated below for clarification, in Equation 6.4.

$$E_m^2 = A_c + B_c u_m^{n_c} \qquad \textbf{Equation 6.4}$$

If it is considered that: $E_f = \Delta E_m$, and $u_f = \Delta u_m$. This is to say that the fluctuating velocity 'u_f' is made up of samples that deviate from the mean, and the same logic can be applied to the hot-wire voltage. Differentiating Equation 6.4 with respect to 'u_m', gives Equation 6.5.

$$\frac{2E_m}{g_c}\frac{\Delta E_m}{\Delta u_m} = n_c B_c u_m^{(n_c-1)} \qquad \textbf{Equation 6.5}$$

Rearranging Equation 6.5 in terms of 'Δu_m' results in Equation 6.6.

$$\Delta u_m = \frac{\Delta E_m}{g_c}\left(\frac{2E_m}{n_c B_c u_m^{(n_c-1)}}\right) \qquad \textbf{Equation 6.6}$$

Recalling that $u_f = \Delta u_m$, and inserting into Equation 6.6 gives Equation 6.7: which can be used as a calibration law for the filtered hot-wire signal.

$$u_f = \frac{E_f}{g_c}\left(\frac{2E_m}{n_c B_c u_m^{(n_c-1)}}\right) \qquad \textbf{Equation 6.7}$$

Here g_c is the hot-wire filter gain.

6.6.2 Fourier Transforming the Data

As the early stages of laminar to turbulent transition is governed by the amplification of independently growing waves, being able identify individual waves is important. As each wave has a fixed frequency, converting the data from the time to the frequency domain allows specific waves to be characterised. A Fourier transformation is performed on the dataset, using the FFT (Fast Fourier Transform) function library provided in Matlab.

Before the data can be transformed, it is often divided into blocks and windowed. Fourier series assumes that a single mode has infinite extent in time, and many Fourier modes would otherwise be required to represent the sudden discontinuity at the beginning and end of each record. The window function 'G_{Window}' is shown in Equation 6.8.

$$G_{Window}(i) = \frac{1}{2}\left\{1 - \cos\left(\frac{2\pi i}{N-1}\right)\right\} \qquad \textbf{Equation 6.8}$$

Here 'i' is the sample index, and 'N' is the number of samples in the signal.

To window, the time signal record is split into smaller records of equal length: each of these records is multiplied by a window function, which is a bell-shaped record with the outer edges tending to zero amplitude. This gradually forces the beginning and end of each record to zero. A Hann window was used in the author's experiment, whose function can be seen in Equation 6.8 (Lynn 1989). The Hann window was used as it is a general purpose window that attempts to optimise spectral leakage; more specialised windows can be used if the spectral content of the signal is well understood (National Instruments 2019).

6.6.3 Determination of Correct Hot-Wire Phase

As discussed in Section 6.3.5, there is a problem of phase distortion between spatially varying measurements when using hot-wire anemometry.

The correct hot-wire signal was initially determined simply by subtracting the phase angle of the reference signal 'F_r' from the phase angle of the hot-wire signal 'F_h'. This is accomplished by converting the two signals to Fourier space and computing the arctan of the imaginary component over the real component of each signal, this determines the phase angle 'φ': as shown in Equation 6.9.

$$\varphi = \tan^{-1}\left(\frac{\text{imag}\{F_h\}}{\text{real}\{F_h\}}\right) - \tan^{-1}\left(\frac{\text{imag}\{F_r\}}{\text{real}\{F_r\}}\right) \qquad \textbf{Equation 6.9}$$

The difference in the phase angles is then used to reconstruct the instantaneous velocity field 'u_f', using Euler's formula shown in Equation 6.10, in combination with the amplitude of the relevant Fourier mode.

$$u_f = |u_f| e^{-i\varphi} \qquad \textbf{Equation 6.10}$$

However, it has since been found that computing the cross-spectrum can yield cleaner results. This is accomplished by converting the two signals to Fourier space, real and imaginary terms of the two signals are then used to determine the cross-spectrum using Equation 6.11.

$$F_h * F_r = \{F_r\} \times [\text{real}\{F_h\} - \text{imag}\{F_h\}] \qquad \textbf{Equation 6.11}$$

(Baher 1990, p.362)

Though this has been found to be an effective method for determining the phase, it has been found that this formula also distorts the signal amplitude. Thus the phase angle is taken as the arctan of the imaginary over the real, and is used to reconstruct the function using Euler's formula (Equation 6.10), again with the appropriate amplitude for the given Fourier mode.

This procedure of phase determination must be performed for every individual resolved mode, for which the correction is to be applied: the sum of these corrected modes across a frequency band will yield the instantaneous velocity across that band.

6.6.4 Ensemble/Conditional Averaging

Ensemble averaging is a post-processing technique for improving the signal-to-noise ratio of the reconstructed instantaneous velocity field. This is a further development of the procedure used to reconstruct the phase, and thus the instantaneous velocity that is described in Section 6.6.3. Ensemble averaging is the process of dividing a time series into discrete lengths, and averaging the lengths; however, in this process the phase angle at the start of each length must be consistent or the signal will be diminished through the averaging procedure. In this work the procedure outlined in Section 6.6.3, is used to ensure that the phase angle is consistent at the start of each record, before the averaging is performed.

6.6.5 Uncertainty Analysis

The main sources of uncertainty were in the measurement of: local velocity through the hot-wire system; unit Reynolds number R_1 through the temperature and pressure sensors; and the suction coefficient 'C_s' through the flow-meter. The uncertainty of the dimensional parameters upon which these non-dimensional groups depend (see Section 4.3 and Section 4.5) is presented in this section.

6.6.5.1 Pressure and Temperature Uncertainty Analysis

Using the procedure outlined in Bell (1999), the measurement uncertainty of the instruments shown in Figure 6.15 can be determined and is shown in Table 6.3.

Table 6.3: Uncertainty of Figure 6.15 instruments.

	Setra 239	Setra 270	PT1000 Sensor	RTD current source
Uncertainty	±0.26 Pa	±23.88 Pa	±0.29°C	±0.12°C

The uncertainty of the instruments was determined from the tolerances specified in the respective user manuals (Correge Sensors 2019; Setra 2019a; Setra 2019b; RS 2019). Therefore, uncertainty can be estimated using Equation 6.12.

$$\text{Standard Uncertainty} = \frac{\text{Tolerance}}{\sqrt{3}} \qquad \textbf{Equation 6.12}$$

Bell (1999)

The tolerance for the analogue to digital conversion was quoted as 1/65536, as this is much smaller than the other uncertainties it is treated as negligible.

To determine the net uncertainty of the temperature measurements, the combined uncertainty was determined using Equation 6.13.

$$\text{Comb. Uncty}\langle T\rangle = \sqrt{(\text{Std. Uncty}\langle PT1000\rangle)^2 + (\text{Std. Uncty}\langle RTD\rangle)^2} \qquad \textbf{Equation 6.13}$$

Bell (1999)

Thus the standard uncertainty of the three measured quantities is shown in Table 6.4.

Table 6.4: Summary of standard uncertainties of environmental conditions.

	$P_T - P_\infty$	P_∞	T_∞
Uncertainty	±0.26 Pa	±23.88 Pa	±0.314°C

These uncertainties can be used to determine the uncertainty of derived quantities. The square root of the sum of uncertainties of the products and quotients in the formulas, normalised by the measurements, can be used to determine the uncertainties of derived quantities used for analysis in this work, as in. Equation 6.14

$$\text{Std. Uncty}\langle\rho\rangle = \rho\sqrt{\left(\frac{\text{Std. Uncty}\langle P_\infty\rangle}{P_\infty}\right)^2 + \left(\frac{\text{Std. Uncty}\langle T_\infty\rangle}{T_\infty}\right)^2} \qquad \textbf{Equation 6.14}$$

Bell (1999)

Using Equation 6.14, the uncertainties of the key derived quantities used in these experiments was determined and tabulated in Table 6.5.

Table 6.5: Uncertainties of derived dimensional units used in experiments.

	Density (ρ)	Temperature (T_∞)	Viscosity (μ)	Free-stream velocity (u)
Uncertainty	±0.021Kg/m^3	±0.314^{o}C	±3.15E-7Pas	±0.249m/s

Determination of the standard uncertainty of different derived quantities, depended on the relationships used to determine the aforementioned quantities. Formulas for these quantities are shown in Equation 6.15, Equation 6.16, and Equation 6.17.

$$\text{Density}\ (\rho) = \frac{P_\infty}{\gamma_{\text{dry air}} T_\infty}; \qquad \textbf{Equation 6.15}$$

White (2011)

$$\text{Viscosity}\ (\mu) = \left(\frac{{T_\infty}^{3/2}}{110.4 + T_\infty}\right) \times 1.458 \times 10^6; \qquad \textbf{Equation 6.16}$$

White (2011)

$$\text{Velocity}\ (u_e) = \sqrt{\frac{2(P_T - P_\infty)}{\rho}}; \qquad \textbf{Equation 6.17}$$

White (2011)

6.6.5.2 Hot-wire Uncertainty Analysis

As the hot-wire probe is calibrated using the free-stream velocity determined from the instrumentation described in Section 6.3.5, there is measurement traceability from the hot-wire system to an absolute quantity. Thus the uncertainty of the hot-wire is a combination of the derived uncertainty of the free-stream velocity (see Section 6.6.5.1) and the residual error from the hot-wire calibration (velocity was related to voltage through King's law). These values are shown in Table 6.6.

Table 6.6: Hot-wire uncertainty quantities.

	Residual	Free-stream velocity	Hw.Probe Velocity
Uncertainty	±0.000167	±0.249m/s	±0.249 m/s

The King's law calibration curves for the normal wire and slanted hot-wires are shown in Figure 6.17. See Sections 6.3.1 and 6.6.1 for information on hot-wire calibration procedure, and the sensor configurations used in experiments. Here 'E' is the voltage of the wire and 'u' is the mean velocity, 'n' is a calibration coefficient from King's law. The uncertainty for the hot-wire mean signal should be taken as ±0.249 m/s, however, for the fluctuating velocity Equation 6.7 considers the fluctuating velocity a perturbation from the mean (i.e. it is a linearised from of King's law): thus it appears more appropriate to taken the uncertainty of the fluctuating velocity as the residual of the hot-wire calibration: ±0.000167.

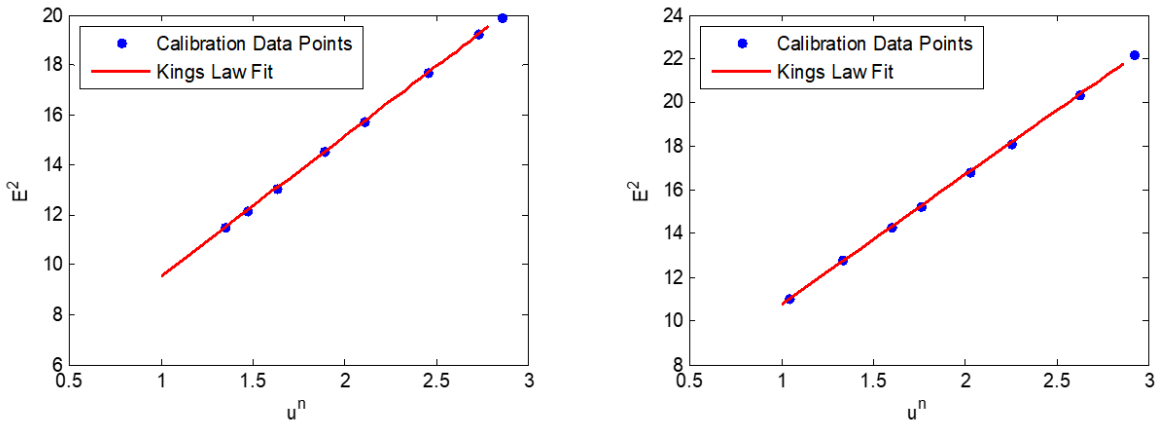

(a) **(b)**

Figure 6.17: Example hot-wire calibration curves, for a straight (a) and slanted (b) wire respectively.

There is also some stochastic uncertainty associated with hot-wire measurements as the unsteady portion of the velocity is measured. This primarily affects experiments in two ways: the first is that the Sampling time must be sufficiently long such that all periodic signals average to a value close to zero; the second is that the sampling rate must be sufficiently high to avoid aliasing of the measured signal. This is solved by ensuring that the hot-wire signal is sampled at twice the low-pass cut-off frequency, set on the band pass filter shown in Figure 6.7.

To check if the record length was sufficiently long: the mean and RMS (root-mean-square) of the velocity were plotted with different sampling times. This is shown in Figure 6.18(a) and (b) respectively. It can be seen that the mean velocity decays to constant average almost immediately, whereas the RMS of the velocity requires a sampling record length of at least 2 seconds to resolve the RMS.

From this analysis, a sampling time of at least 2 seconds was used in all experimental measurements with the hot-wire probe.

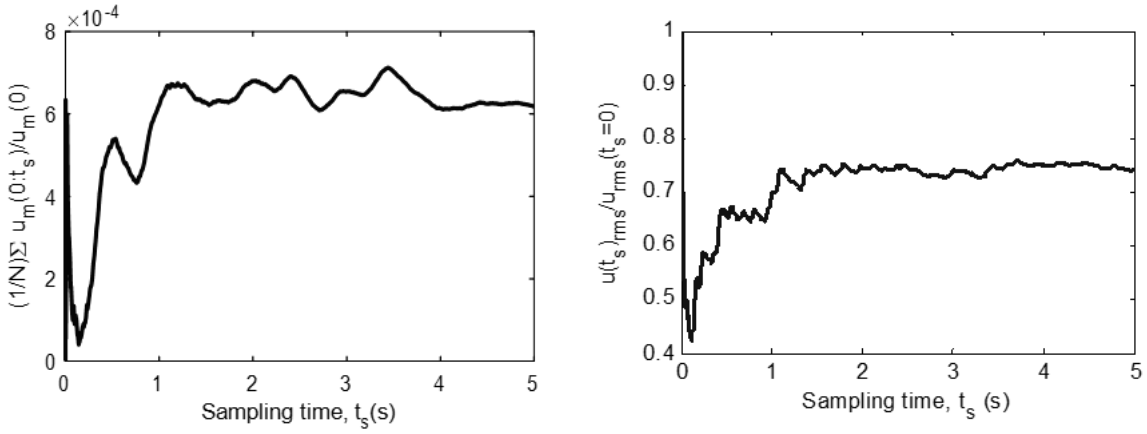

(a) **(b)**

Figure 6.18: Change in mean (a) and RMS (b) of the recorded hot-wire signal for different sample lengths.

6.6.5.3 Flow-meter Uncertainty Analysis

The uncertainty of the suction flow-rate can be determined from the manual of the unit. This can be used to determine the uncertainty of the Suction Coefficient 'C_s' if the uncertainties of free-stream velocity and tunnel area are known. The tunnel area was determined by measuring the width and height of the working section with a ruler, that had 0.5mm increments. Thus, the resolution of the ruler was used to specify its uncertainty. Using these values in combination with Equation 6.14, the uncertainties of the first of the two flow-meters described in Section 6.4.1, was determined and tabulated in Table 6.7.

Table 6.7: Low-range/high-accuracy flow-meter uncertainty values.

	Suction flow-rate	Free-stream velocity	Tunnel Area	C_s
Uncertainty	±1.6E-6m^3/s	±0.249m/s	±1E-3m^2	±1.9E-07

A second flow-meter was used at high suction rates, it had a $1/10^{th}$ the accuracy of the flow-meter used for most test cases. The uncertainty is shown in Table 6.8.

Table 6.8: High-range/low-accuracy flow-meter uncertainty values.

	Suction flow-rate	Free-stream velocity	Tunnel Area	C_s
Uncertainty	±1.6E-5m^3/s	±0.249m/s	±1E-3m^2	±1.4E-06

The lowest C_s value considered in this study had a value of 0.75E-5, see Figure 8.11. This suggests that the uncertainty of the non-dimensional suction rate 'C_s' is acceptable.

6.6.5.4 Unit Reynolds Number Uncertainty Analysis

The uncertainty of the dimensionless parameter unit Reynolds number 'R_1' was also determined (again using Equation 6.14) and tabulated in Table 6.9.

Table 6.9: Reynolds number uncertainty analysis results.

	Dynamic Viscosity	Free-stream velocity	Density	R1
Uncertainty	±3.15E-7Pas	±0.249m/s	±0.021Kg/m^3	±2.75E4

Here it can be seen that that uncertainty associated with Reynolds number is far less than its nominal value of R_1=0.9E6.

7 Experimental Strategy and Preliminary Validation

7.1 Overview of Tests

In this study a large number of experimental test cases were investigated. This number is large enough to prohibit the display of all experimental results in this document. Here, some context and justification is provided for the results that are presented. The different types of measurement sets taken during this work are discussed. Tests were performed on suction arrays and an isolated suction perforation, the layout of these test panels is described in Section 6.2.1.

7.1.1 Initial Parametric Study

At the beginning of this work, a parametric study was performed on the 'over-suction' phenomenon. In this parametric study, the probe was located at a fixed position down-stream of the suction array. A single profile was taken for each combination of dependent suction parameters. In this study the point exciter was used to force the boundary layer, the idea was that the amplitude of the $u_{rms}(y)$ velocity profile could be monitored and recorded for each test case, at the excitation frequency.

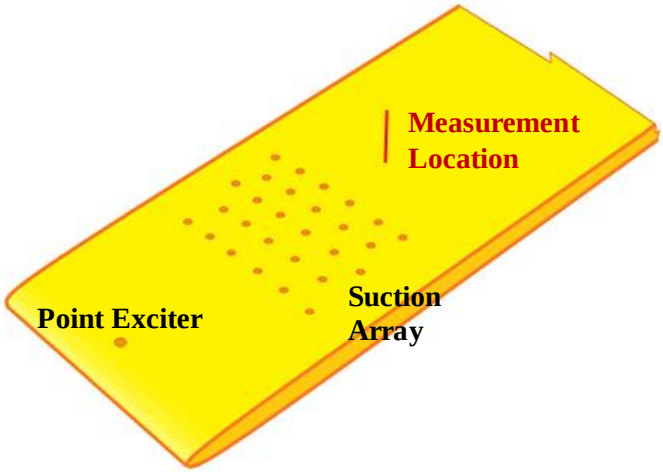

Figure 7.1: Illustration of single point measurements used in parametric study of 'over-suction'.

If the excited wave was attenuated, compared to the no-suction case, the implication was that the suction was having a stabilising effect on the flow. Conversely, if the amplitude increased, it suggested that the suction was having a destabilising effect on the flow and potentially causing a premature transition. The test cases studied are presented in Table 7.1. These measurements were taken at x/C=0.34.

Table 7.1: Suction rates studied for different perforation size and Reynolds number (R_1) combinations.

	0.6mm Perforations	1mm Perforations	1.5mm Perforations
R_1=0.5E6	C_s=[0.0, 0.517E-6, 0.615E-6, 0.689E-6, 0.788E-6, 1.059E-6, 1.304E-6, 1.625E-6, 1.846E-6, 3.569E-6, 8.641E-6]	C_s=[0.0, 0.541E-6, 0.615E-6, 0.714E-6, 0.812E-6, 0.935E-6, 1.403E-6, 1.625E-6, 1.970E-6]	C_s=[0.0, 0.025E-6, 0.074E-6, 0.123E-6, 0.197E-6, 0.246E-6, 0.295E-6, 0.345E-6, 0.492E-6, 0.615E-6, 0.862E-6, 1.231E-6, 1.920E-6]
R_1=0.75E6	C_s=[0.0, 0.410E-6, 0.443E-6, 0.492E-6, 0.525E-6, 0.607E-6, 0.705E-6, 1.033E-6, 1.443E-6, 1.722E-6]	C_s=[0.0, 0.328E-6, 0.377E-6, 0.459E-6, 0.590E-6, 0.357E-6, 0.820E-6]	C_s=[0.0, 0.082E-6, 0.164E-6, 0.197E-6, 0.246E-6, 0.312E-6, 0.426E-6, 0.820E-6]
R_1=1E6	C_s=[0.0, 0.234E-6, 0.271E-6, 0.283E-6, 0.307E-6, 0.344E-6, 0.443E-6]	C_s=[0.0, 0.222E-6, 0.246E-6, 0.283E-6, 0.333E-6, 0.357E-6, 0.443E-6]	C_s=[0.0, 0.172E-6, 0.209E-6, 0.246E-6, 0.369E-6, 0.468E-6, 0.530E-6, 0.640E-6, 0.764E-6]

The results from this parametric study are not shown in this document, due to the difficulties in interpreting the dataset and presenting it in a clear and concise manner, however more detailed examples of what was observed can be found in Section 8.1.

The main findings of the initial parametric study were as follows. Firstly, the fluctuating velocity root mean square value 'u_{rms}' for the entire spectrum (St=0.3-750, 2-5000Hz) decreased consistently for increasing suction, until a point was reached where 'u_{rms}' started to increase for increasing rates of suction.

Secondly, if 'u_{rms}' for only the excitation frequency (this varied with the Reynolds number) was studied, it was found the it was attenuated for all considered suction rates, except in cases where a fully turbulent spectrum was observed.

Thirdly, it was found that the majority of the energy in the spectrum at high suction rates was at low frequencies (St~0.3-6, 2-40Hz). This prompted a detailed study of the flow physics of the boundary layer, as it was unclear how to define a threshold of 'over-suction'. Due to the time intensive nature of the detailed measurements, efforts were focused only on the smallest perforation size (d=0.6mm) for all detailed measurements presented in this thesis.

7.1.2 Centre-line Stream-wise Measurement Planes

A number of test cases consisted of stream-wise measurements at centre span (z/d=0, where d is perforation diameter). In this study the centre span location aligns with the point exciter, and the perforations in every second row of the suction array, as shown in Figure 7.2. In essence these measurements allowed the stream-wise development of the boundary layer to be assessed. Here it is expected that the local flow-field attributed to the suction, will be dominated by the local change in pressure gradient ahead and behind individual suction perforations. Tests presented in this document that use this measurement plane are shown in Table 7.2

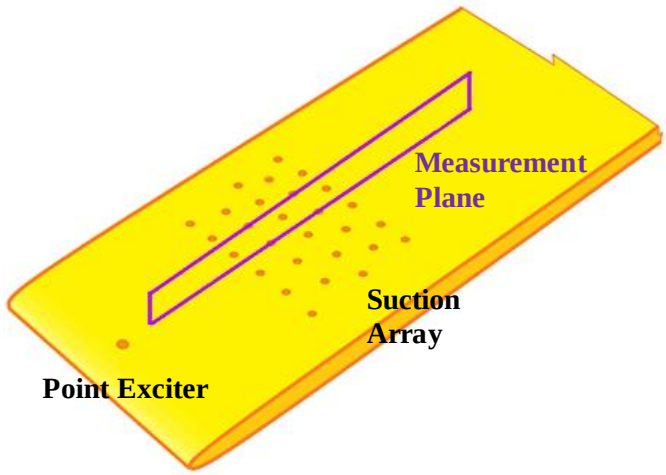

Figure 7.2: Illustration of a typical centre span measurement plane

Table 7.2: Figures that show Stream-wise tests taken along centre-span.

Figure 7.10: 0.24<x/C<0.53
Figure 7.11: 0.24<x/C<0.53
Figure 7.12: 0.24<x/C<0.53
Figure 12.4: 0.25<x/C<0.35
Figure 12.6: 0.22<x/C<0.54
Figure 12.7: 0.25<x/C<0.35
Figure 12.8: 0.22<x/C<0.54
Figure 12.9: 0.18<x/C<0.40

Here the number of measurement profiles (i.e. line measurements across the wall-normal 'y') per plane for the figures shown in Table 7.2 are provided. This is to show the resolution of the measurements taken in this study. Figure 7.10 to Figure 7.12 use a resolution of 40 profiles. Figure 12.4 and Figure 12.7 used 13 measurement profiles per measurement plane. Figure 12.6 and Figure 12.8 used 71 profiles per measurement plane Figure 12.9 used 21 measurement profiles per measurement plane.

7.1.3 Off-axis Stream-wise Measurement Planes

Most test cases presented in this document were taken in the stream-wise direction by offset from centre span. This offset was z/d=-3.33. As with the centre-line measurements these types of measurements follow the stream-wise development of the boundary layer. Based on span-wise measurements taken at a single x/C station, this offset was known to be in the path of vortices shed from the suction perforations (described in Section 4.2). Effectively these measurements also assessed the stream-wise stability and development of these vortices/stationary modes. Tests presented in this document that use this measurement plane are shown in Table 7.3.

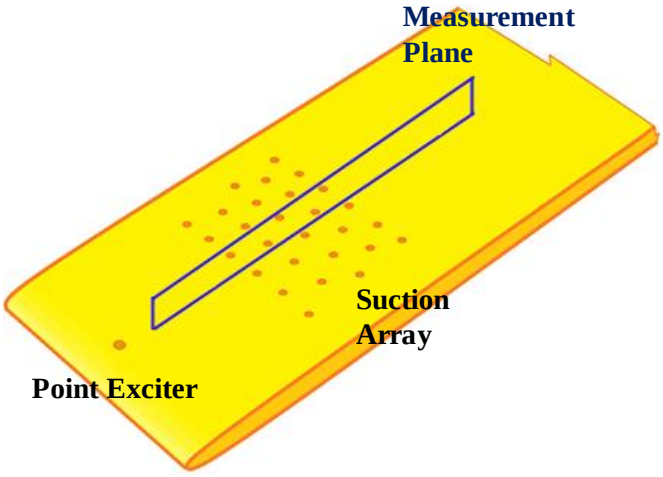

Figure 7.3: Illustration of a typical off-centre span measurement plane

Table 7.3: Figures that show stream-wise tests taken offset from centre-span.

Figure 8.2: 0.24<x/C<0.53	Figure 8.9: 0.18<x/C<0.53
Figure 8.3: 0.24<x/C<0.53	Figure 8.10: 0.23<x/C<0.55
Figure 8.4: 0.24<x/C<0.53	Figure 8.11: 0.24<x/C<0.53
Figure 8.5: 0.21<x/C<0.4	Figure 8.12: 0.24<x/C<0.53
Figure 8.6: 0.18<x/C<0.53	Figure 8.14: 0.22<x/C<0.34
Figure 8.7: 0.18<x/C<0.53	Figure 8.17: 0.22<x/C<0.34
Figure 8.8: 0.18<x/C<0.53	

The resolutions of the figures shown in Table 7.3 are as follows: Figure 8.2 to Figure 8.5 show cases with 40 measurement profiles per measurement plane. Figure 8.6 to Figure 8.9 show cases with 10 measurement profiles per measurement plane. Figure 8.10 show cases with 73 measurement profiles per measurement plane. Figure 8.11 and Figure 8.12 show cases with 10 measurement profiles per measurement plane. Figure 8.13 and Figure 8.14 and Figure 8.17 shows cases with 25 profiles per measurement plane.

7.1.4 Span-wise Measurement Planes

As a three-dimensional flow field was present in all experiments that used wall suction, it is necessary to study the span-wise variation of structures in the flow. To this end a number of span-wise measurement planes were used in these tests, similar to the illustration shown in Figure 7.4. These span-wise measurements were taken shortly down-stream from the last suction perforation row (x/C=0.33) to 200mm from the end of the stream-wise traverse axis (x/C=0.53). In this study, results are presented from a case where 7 equally spaced planes were taken between these beginning and end stations. Figures that use data from this case are presented in Table 7.4.

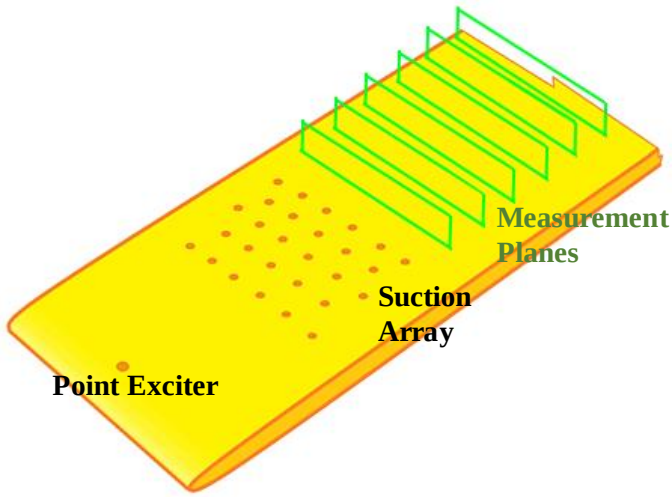

Figure 7.4: Illustration of a typical span measurement planes.

Table 7.4: Figures that show span-wise tests taken across different stream-wise stations.

Figure 8.13: -6<z/d<6
Figure 8.15: -6<z/d<6
Figure 8.16: -6<z/d<6
Figure 8.21 (b): -6<z/d<6

A number of additional span-wise plane measurements were taken that are not presented in this document. This is because it was unknown what the correct spatial resolution should be to avoid aliasing before starting these experiments. To find the correct resolution an initial span-wise resolution was chosen arbitrarily, and a measurement was taken. The resolution was then doubled and repeated. This process was repeated until the span-wise variation of the measured flow-field stopped changing. An initial resolution of 1mm was chosen, the final resolution used was 0.333mm. It was found that there was no change from a 0.5mm resolution case used for comparison. For the cases shown in Table 7.4 a resolution of 22 profiles per measurement plane was used.

7.1.5 Centre-line Stream-wise Measurement Planes (Isolated Perforation)

Additionally, some isolated suction perforation test cases were studied, this was to investigate if observed flow features were due to interactions between multiple perforations. A diagram of the basic measurement plane configuration is shown in Figure 7.5. Stream-wise measurements along the centre were taken and the figures that use this type of measurement plane are shown in Table 7.5. In these cases, a resolution of 21 profiles per measurement plane was used.

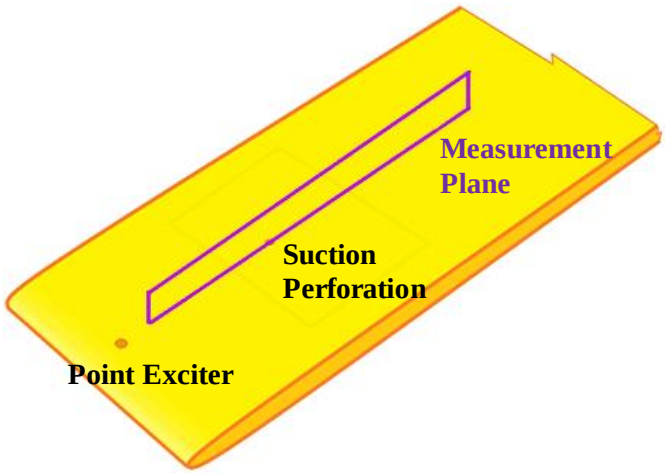

Figure 7.5: Illustration of a typical off-centre span measurement plane (Single Perforation).

Table 7.5: Figures that show stream-wise tests taken along centre-span (Isolated Perforation).

Figure 8.18: 0.18<x/C<0.4
Figure 8.19: 0.18<x/C<0.4
Figure 8.20: 0.18<x/C<0.4

7.1.6 Span-wise Measurement Planes (Isolated Perforation)

Span-wise measurements were also taken with the isolated perforation. A diagram of the basic measurement plane configuration is shown in Figure 7.6. Stream-wise measurements along the centre were taken and the figures that use this type of measurement plane are shown in Table 7.6. In these case, a resolution of 26 profiles per measurement plane was used. The test case shown consisted of 8 measurement planes. Though only the results from one plane is presented in Figure 8.21.

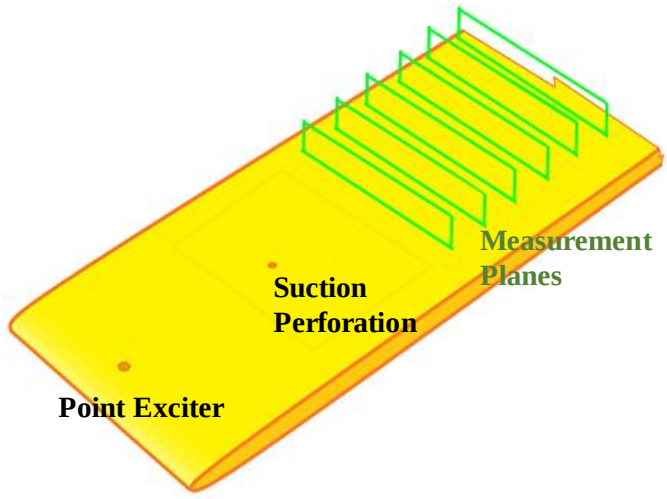

Figure 7.6: Illustration of a span-wise measurement planes cross multiple stream-wise stations (Single Perforation).

Table 7.6: Figures that show span-wise tests taken across different stream-wise stations (Isolated Perforation).

Figure 8.21 (a) : -8.3<z/d<8.3,

7.2 Flow Quality Checks

7.2.1 Background Turbulence-Empty Test Section

To investigate the residual background turbulence levels in the Gaster wind-tunnel facility, a hot-wire probe was placed facing upstream inside an empty test section. Typically in the literature values for the turbulence intensity are given by the root mean square velocity, u_{RMS}, as a percentage of the free-stream velocity, u_{inf} (Poll 1985; Bippes 1999). This however does not indicate the uniformity of the spectral energy across the frequency domain.

Figure 7.7 shows the spectral energy distribution of the fluctuating velocity component across the frequency domain, for an empty working section. This data represents a range of different free-stream velocities. On this plot only the velocities that produced the maximum and minimum spectral energy are shown.

As expected the energy scales with Reynolds number so the lowest and maximum velocity cases correspond to the spectral energy minimum and maximum respectively. An average spectral energy curve is also plotted which shows the average of all the spectral energy across all velocities considered. It can be seen that the energy is not spread uniformly across the frequency domain.

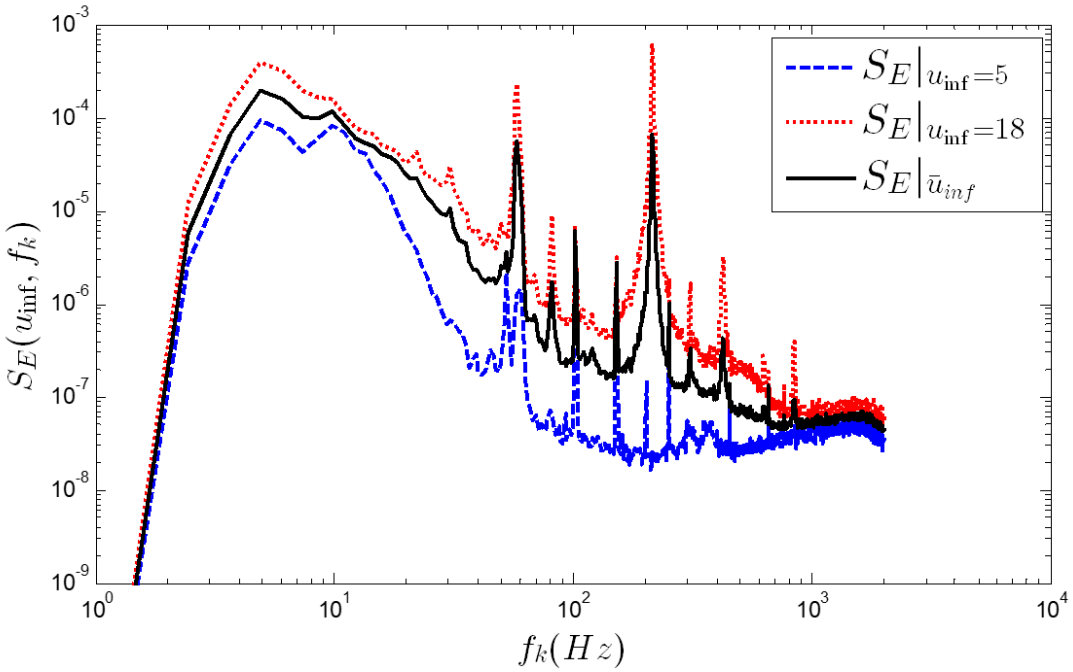

Figure 7.7: Spectral Energy distribution across the frequency domain, for an empty test section. This was obtained at 8 different free-stream velocities: 5, 6, 7, 10, 12, 15, 17, and 18 m/s. Spectral energy plots are provided for the minimum and maximum speeds, in addition the average spectrum across all velocities is shown. The range in Reynolds number is 0.3E6 to 1.2E6.

It is useful to try and determine the source of the tones or peaks in Figure 7.7, this provides an idea of the signal noise and unwanted flow disturbances acting on the controlled experiment. It is seen that there is considerable low frequency in the spectrum, this is commonly attributed to noise generated in the flow by the wind-tunnel (Sattarzadeh and Fransson 2017). For example, there are vortices in the corners of the wind-tunnel due to its cross section being square (White 2011).

There are also peaks at 50Hz, 100Hz, and 200 HZ; these are associated with mains-pick-up noise. Effectively this is noise that comes through the power supply. Dimension frequency 'f_k(Hz)' is presented as it makes sources of deterministic noise such as the mains-pick-up noise easier to identify.

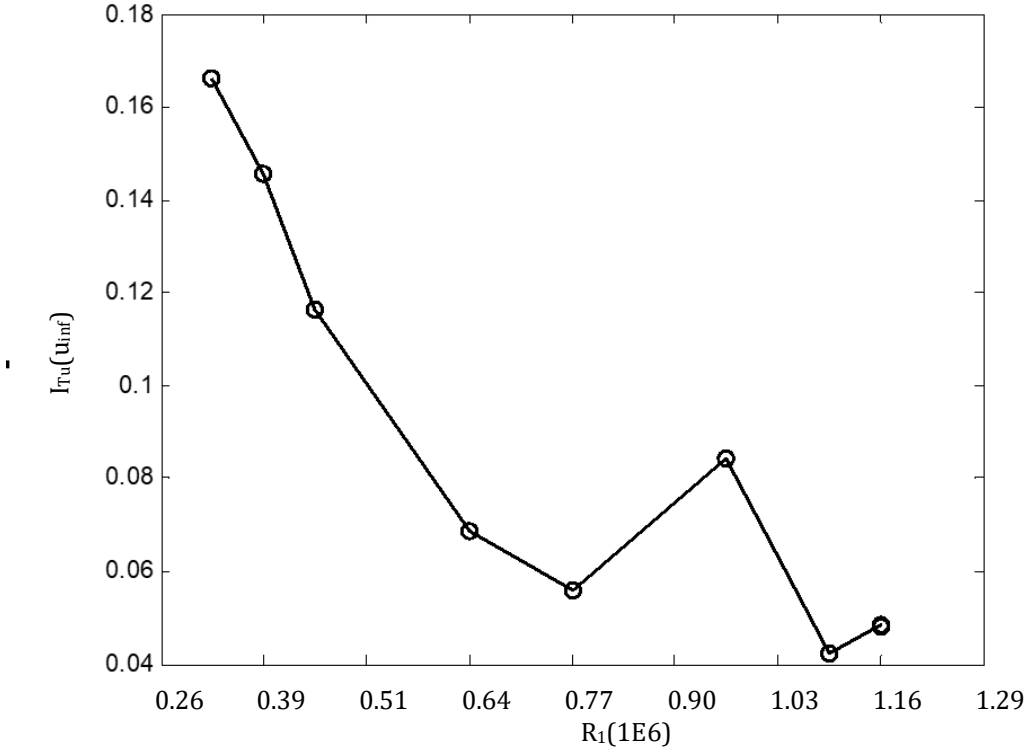

Figure 7.8: Change in turbulence intensity across different unit Reynold numbers, for an empty test section.

Figure 7.8 shows the change in turbulence intensity 'I_{Tu}' across the different unit Reynolds numbers 'R_1', using the same data as shown in Figure 7.7. I_{Tu} can be seen to decrease with increasing unit Reynolds number; a region of high localised turbulence appears to be present at R_1=0.965E6. Here, the spectral energy is not uniformly distributed across the frequency domain, the effects of which are excluded in Figure 7.8.

The distribution of spectral energy can be demonstrated through the standard deviation 'S_D' of individual modes from their Root Mean Square (RMS) value. This helps to quantify how non-uniform the background turbulence is at different Reynolds numbers. This is important for the study of transition as in the linear regime modes grow linearly independent of one another. Thus, if all the energy is localised across a small frequency band, instability waves will grow non-linear at lower energy levels than an equivalent case where the free-stream turbulence is uniformly distributed across the spectrum. Thus the standard deviation of velocity perturbations from their RMS value is shown in Figure 7.9. It can be seen that the Standard deviation follows the same trend seen in Figure 7.8, for the turbulence intensity 'I_{Tu}'.

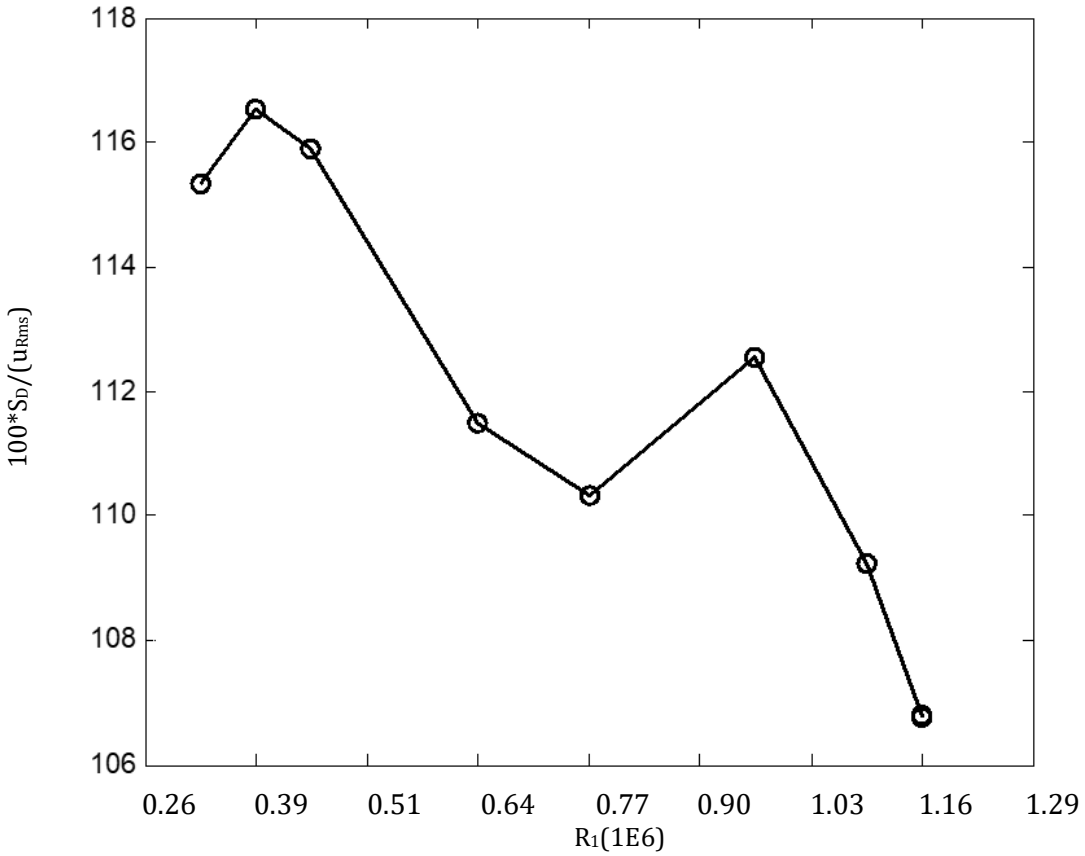

Figure 7.9: Change in the standard deviation of different Fourier modes from the RMS velocity in the fluctuating velocity spectrum across different unit Reynold numbers. These standard deviations are expressed as a percentage of the RMS velocity.

7.2.2 Background Turbulence-With Flat Plate Model

With an empty section the background turbulence intensity ('I_{Tu}') is quoted to be less than 0.01% (NWTF 2018). With a test section containing a flat plate model, these levels are expected to be higher. Figure 7.10 shows measurement of the turbulence intensity 'I_{Tu}' in a stream-wise ('x') / wall-normal ('y') plane. In this plot 'y' is plotted against 'I_{Tu}', the data is separated into stations: where each station corresponds to a different 'x' location in the dataset.

The change in intensity across the boundary layer is shown at two stream-wise ('x') stations and as an average across all stream-wise ('x') stations. The average intensity across 'x' is denoted as '$\bar{x}$'. It can be seen in Figure 7.10 that the average turbulence intensity, outside the boundary layer, is less than 0.02%. Here the range of 'x' stations, normalised by chord 'C', is 0.24<x/C<0.53.

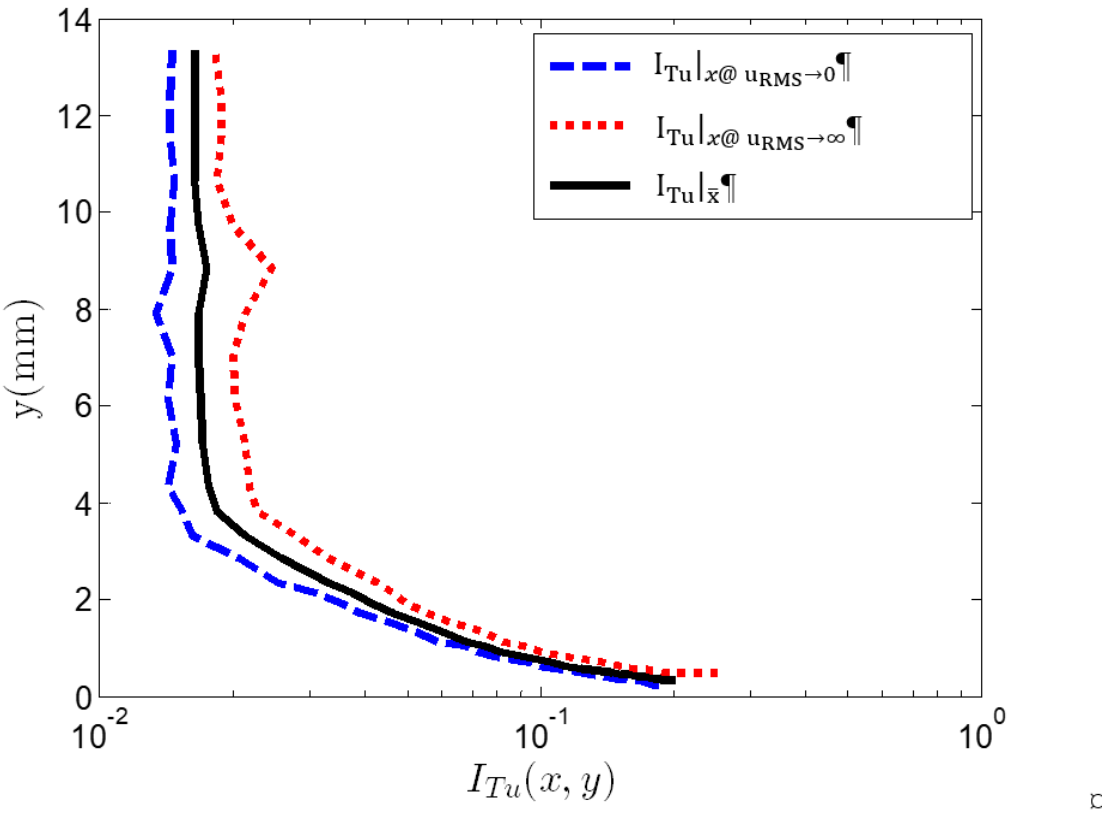

Figure 7.10: Distribution of stream-wise averaged turbulence intensity across the boundary layer. Flat plate model is present, free-stream velocity is 14m/s (R_1=0.9E6). Turbulence intensity is shown as percentage of mean velocity 'u(x,y)'. 0.24<x/C<0.53

Providing the free-stream turbulence intensity of the wind-tunnel when the model is mounted, is useful for comparing the results of this thesis with other experiments on transition, as well as with practical flight applications. This is because the level of background disturbance energy will affect the amount of growth of mentioned disturbances required by the flow to transition to a turbulent state. However, turbulence intensity as a metric is not fully comprehensive. This is because this metric assumes that the turbulence is reasonably homogenous. If this were true, then the spectral distribution of energy should be uniform across the frequency domain.

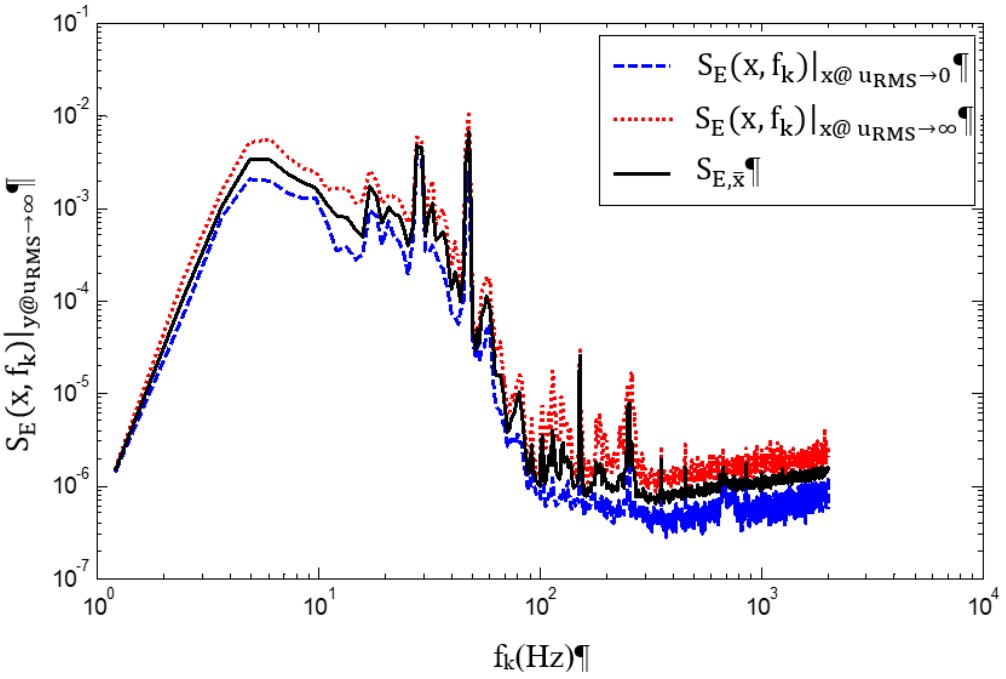

Figure 7.11: Distribution of spectral energy across the frequency domain. Flat plate model is present, free-stream velocity is 14m/s (R_1=0.9E6). 0.24<x/C<0.53

However, if the spectral energy 'S_E' is determined for the same case shown in Figure 7.10, it can be seen that there is some variation across the frequency domain. Figure 7.11 shows the spectral energy distribution as a function of 'x', the distance from the leading edge. It is important to consider that the spectral energy is nominally a function of 'x','y', and 'f_k': i.e. '$S_E(x,y,f_k)$'. This can be reduced to two dimensions by taking the maximum of the spectral energy across the wall-normal 'y' for a given 'x', and 'f_k'. This can be represented in mathematical notation as: '$S_E(x, f_k)|_{y@u_{RMS}\to\infty}$'. This can be further reduced to being dependant on one variable 'f_k', by either taking the mean spectral energy across the length of the plate, i.e: '$S_{E,\bar{x}}$'or by taking the spectral energy at stations where the total energy is either at a maximum, i.e.: '$S_E(x, f_k)|_{x@\ u_{RMS}\to\infty}$', or minimum, i.e.: '$S_E(x, f_k)|_{x@\ u_{RMS}\to 0}$'.

The minimum spectral energy across the wall-normal can also be determined: written in mathematical notation it is: '$S_E(x, f_k)|_{y@u_{RMS}\to 0}$'. The associated plot of the spectral energy 'S_E', against frequency 'f_k' can be seen in Figure 7.12.

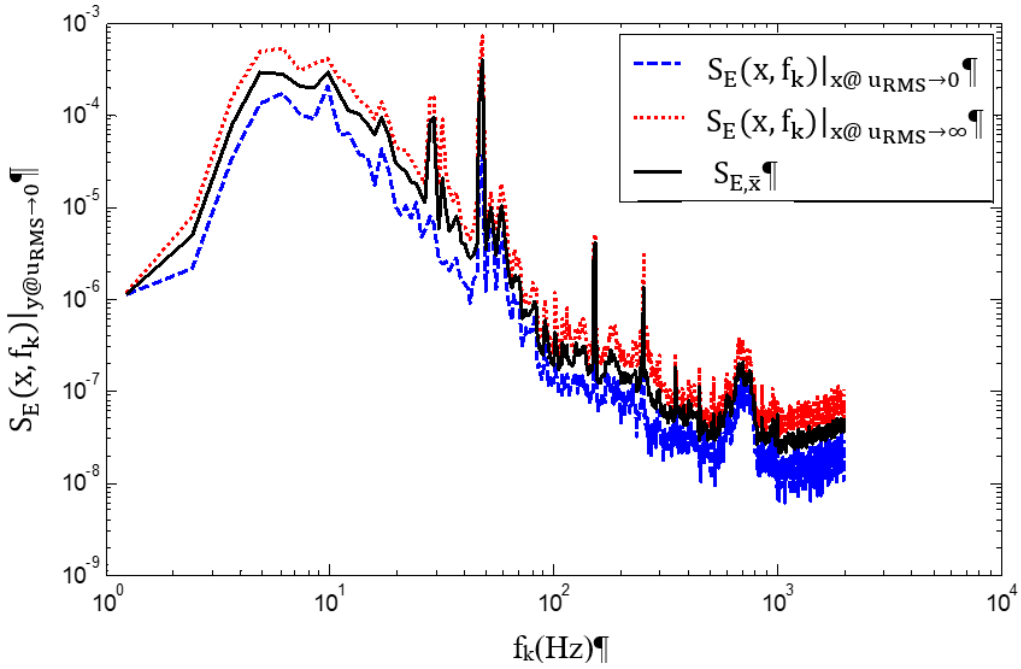

Figure 7.12: Distribution of spectral energy across the frequency domain. Flat plate model is present, free-stream velocity is 14m/s (R_1=0.9E6). 0.24<x/C<0.53

The standard deviation of different spectral modes from the RMS, 'u_{RMS}' was determined for the spectrum shown in Figure 7.11 and Figure 7.12. The standard deviation of individual Fourier modes from 'u_{RMS}', is presented in Table 7.7. This gives a quantitative indication of the uniformity of the turbulence across the spectrum. This is provided at two locations along the wall normal, one near the wall where 'u_{RMS}' is maximum and another in the free-stream where 'u_{RMS}' is minimum. In comparing the standard deviations '$S_D(x)$' with respect to their corresponding 'u_{RMS}' values, it initially appears as though the turbulence levels are both lower and more uniform in comparison to when near the wall. When expressed as a percentage of the 'u_{RMS}' values, the standard deviation is approximately 2.1% for the free stream, and is 1.9% near the wall which is counter to expectation.

Table 7.7: Standard deviation of spectral modes from the Root Mean Square (RMS) velocity, 'u_{RMS}'. Cases where the RMS is maximum and minimum along the wall-normal are presented.

$S_D(x)\|_{y@u_{RMS}\to 0}$	$S_D(x)\|_{y@u_{RMS}\to \infty}$	$u_{RMS}\|_{\bar{x},y@u_{RMS}\to 0}$	$u_{RMS}\|_{\bar{x},y@u_{RMS}\to \infty}$
2.9×10^{-5}m/s	1.1×10^{-4}m/s	1.4×10^{-3}m/s	5.7×10^{-3} m/s

7.2.3 Uniformity of Pressure Distribution

In conducting an experiment over a flat plate at low Reynolds number (0.9-1.2E6) and at a low turbulence intensity (0.014-0.019%): there are certain experimental controls that must be verified.

Firstly, the pressure gradient must be minimised in the area of measurement (i.e. appropriate for a flat-plate experiment). Secondly, the flow must be laminar at an appropriate Reynolds number. These criteria can be verified: by measuring the static pressure field around the flat plate using surface pressure ports, and by performing a velocity traverse across the boundary layer respectively.

Figure 7.13 shows pressure distributions obtained from the static pressure ports for different wind speeds. Each port is measured for three seconds; the median, mean, and mode are calculated across the time the measurement is taken to give three approximations of the pressure distribution. In addition, maximum and minimum instantaneous pressure measurements are shown to give an indication of the range of error.

It can be seen that the mean, mode, and median are similar in magnitude and show better agreement as speed increases. It can be seen the pressure distributions based on each of these statistical quantities is also flat. It is noted that the minimum and maximum pressure values are not always flat. The error band appears to shrink as speed is increased.

7.2.4 Suction System Checks

Specific issues relating to the suction system, that may contaminate experimental results were also investigated. This includes the effects of leakage, pump noise, and resonance inside the suction plenum. These analyses were performed within the context of studying the low frequency disturbance introduced in Section 8.1. These potential sources are believed to be not important based on the results obtained. These results are presented in Appendix B. The repeatability of the low frequency disturbance is also presented in Appendix B.

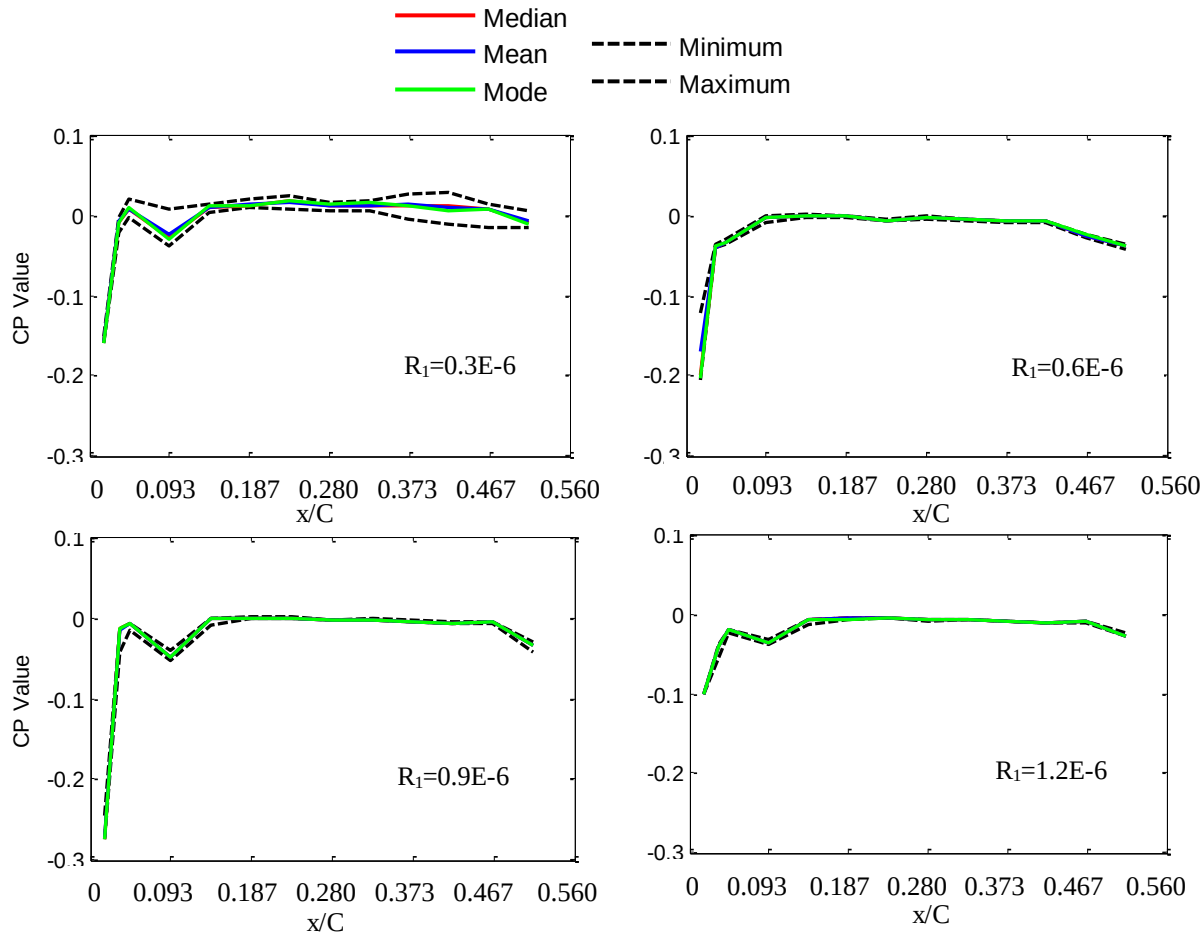

Figure 7.13: Pressure distributions for different speeds.

In these experiments, the uniformity of pressure distribution is mostly important in ensuring that a good approximation of a Blasius flow is in effect for the no-suction baseline case. Thus a comparison of experimental results with Blasius may provide a more useful demonstration that the controls in the baseline case are sufficient to ensure that the flow is Blasius. Such a comparison can be seen in Figure 7.14: here the circular point correspond to data points taken during experimental measurements, and the dotted dashed line corresponds to a theoretical calculation of the Blasius velocity profile (Schlichting 1977).

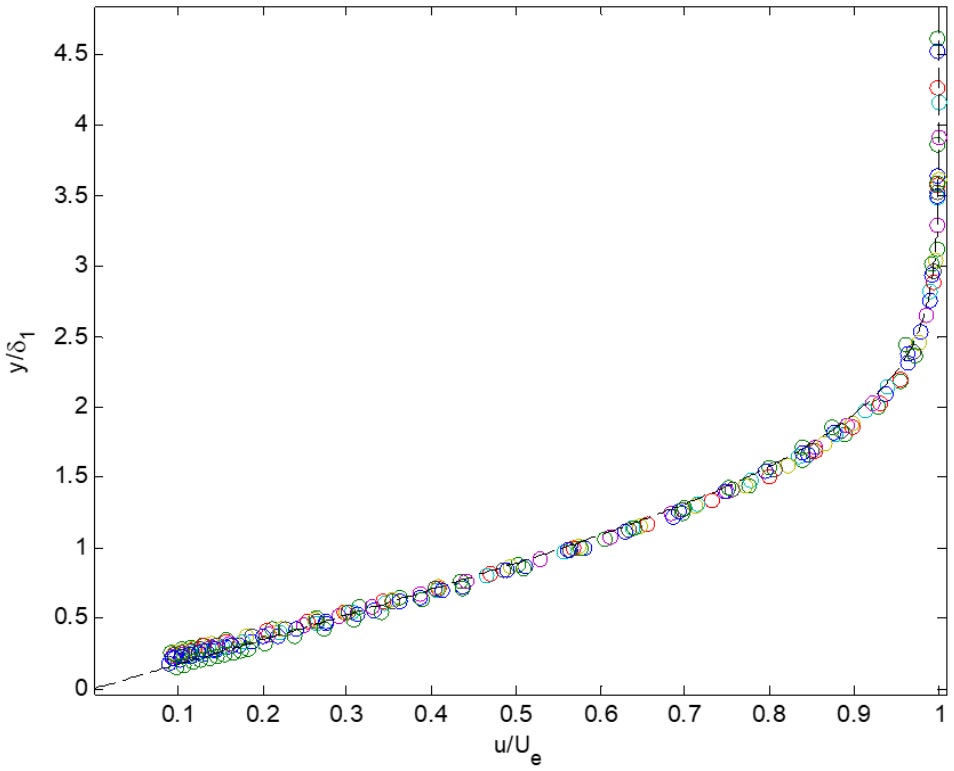

Figure 7.14: A series of velocity profiles, across the wall-normal, taken from x/C=0.26 to x/C=0.56. Free-stream Reynolds number was 0.9E6.

In this plot the stream-wise velocity 'u' is non-dimensionalised with respect to the boundary layer edge velocity 'U_e', and the wall normal 'y' is non-dimensionalised with respect to the displacement thickness 'δ_1'. It can be seen that agreement between the experimental and theoretical results is good, however, a slight favourable pressure gradient is evident; however, this is considered satisfactorily small.

8 Main Experimental Results

In this section the main findings of this work are presented. There were two main findings: the discovery of a low-frequency dominated 'over-suction' transition process; and the discovery of high frequency secondary waves in the traditionally studied 'over-suction' transition process (see MacManus and Eaton 2000; Goldsmith 1956). In this section: these findings are presented, their importance is demonstrated, and a physical explanation is provided for these processes.

Most of the results presented are scans taken in an xy-plane. For most of these results, the span-wise location (z) was chosen such that the xy-plane does not intersect any suction perforations. To clarify, the perforations had a diameter of 0.6mm with a row and column spacing of 6mm. Each row was staggered by 3mm. To avoid all suction perforations when measuring in an xy-plane, all measurements were taken at z=-3.33mm (z=0mm coincides with the centreline) unless otherwise specified.

For the spectral analysis performed in this section the minimum value of the spectra presented here appear smaller than the residual of the hot-wire calibration: ±1.67E-4. However, all significant features that are highlighted in this section have amplitudes which are greater than this uncertainty. All mean velocity measurements were also below the uncertainty of these measurements: ±0.249m/s ($u_m/u_{mean,e}$=±0.018) (See Section 6.6.5 for the uncertainty analysis).

8.1 Discovery of the Low Frequency Disturbance

In this study, the first set of experiments involved a comparison between a no-suction test case over the flat-plate model, and a suction case. Illustrations of the basic setup for these two cases are shown in Figure 8.1. The flowmeter is omitted from the drawing for brevity.

A third case was added (Figure 8.1 (c)) towards the end of this test campaign, which was a suction case where the suction pump was omitted. Suction was achieved by utilising the static pressure difference between the volume above the suction panel, and the ambient pressure condition outside the wind-tunnel.

The wind-tunnel has vents at the end of the test-section which establish a reference pressure; however, these vents have fine porosity filters which induce a total pressure drop. This affects the static pressure over the flat plate; furthermore, the flap angle, normally used to adjust the position of the attachment line, has also been found to affect the static pressure field over the flat plate. These two effects work to establish a difference in static pressure from ambient, which can be used to drive wall suction.

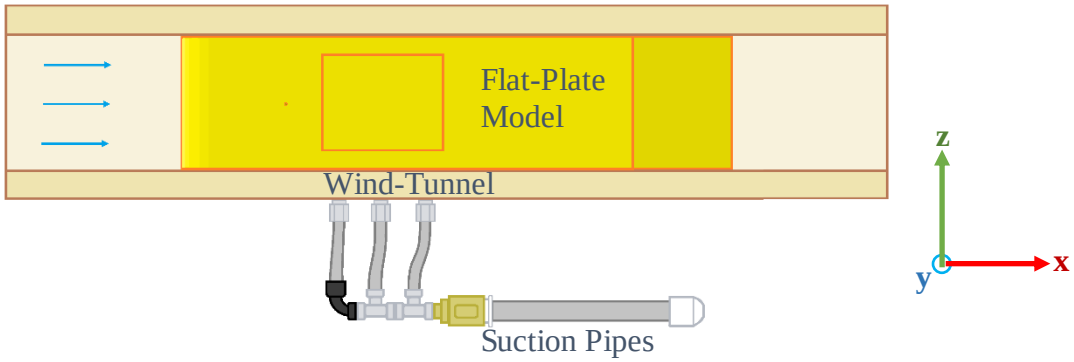

(a)

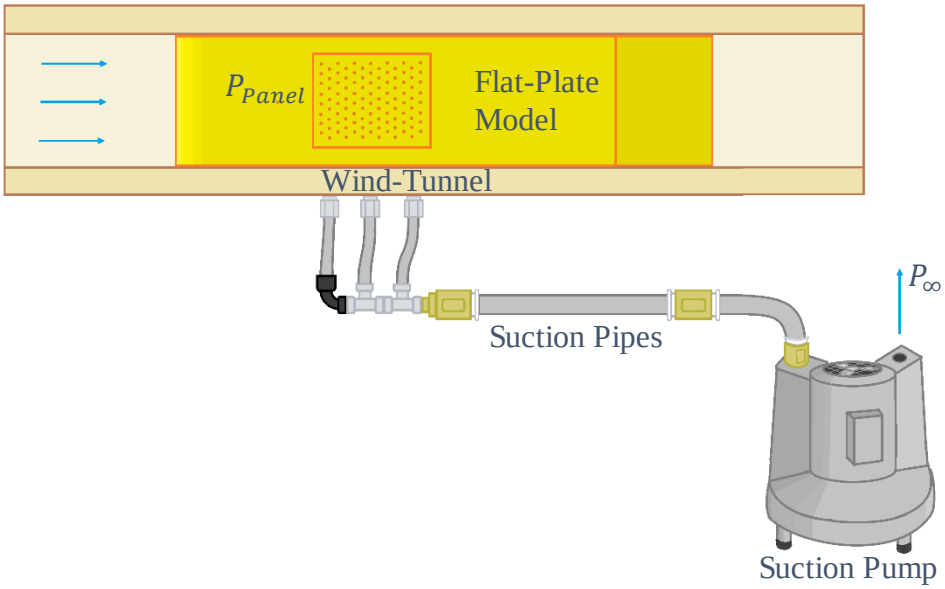

(b)

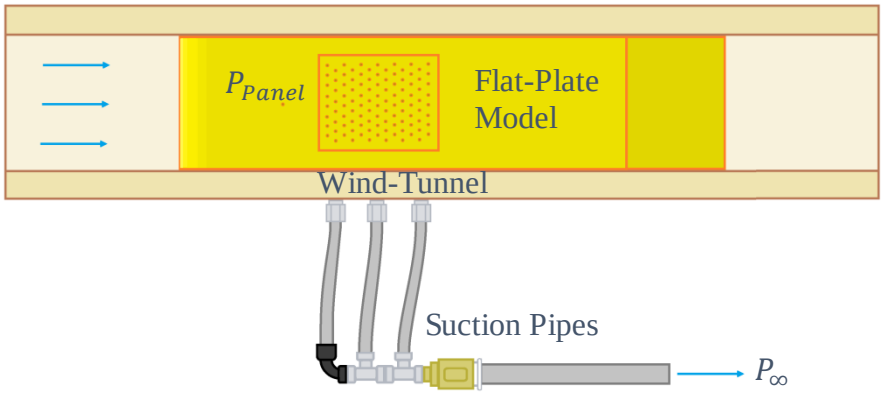

(c)

Figure 8.1: Three basic test configurations used in early experiments: (a) flat-plate with no suction or perforations, (b) flat plate with pump driven suction perforations, and (c) flat-plate with suction perforations driven by "natural" pressure gradients.

8.1.1 Mean Velocity Profiles

Here velocity profiles obtained for the different test configurations shown in Figure 8.1 are provided. Figure 8.2 shows contours of mean velocity ratio '$u_{mean}/u_{mean,e}$' with the associated profile shapes super-imposed. Here 'u_{mean}' is the mean velocity component which is dependent on the distance from the wall 'y', i.e. $u_{mean}(y)$. $u_{mean,e}$ is equivalent to $u_{mean}(y=\delta)$, where 'δ´is the boundary layer thickness.

The spatial origins (in 'x/C') for each of these profile shapes is marked with a dashed vertical line. Here 'x' is the distance from the leading edge, and 'C' is the chord/plate length.

The distance from the wall is shown as a non-dimensional parameter 'η'. This parameter is simply a ratio of Reynolds number with respect to 'y' and Reynolds number with respect to 'C'. Here '$u_e=u_{mean,e}$', and 'υ' is kinematic viscosity.

It is observed that the flow is laminar for all cases shown in Figure 8.2; this is based on the shape of the velocity profiles. The lack of a log-law layer in the profile shape is characteristic of laminar velocity profiles.

The shape factor 'H' is also displayed on the graph. The two vertical black-on-white lines denote the beginning and end of the suction array. It can be seen that there is a small decrease in shape factor after the beginning of the suction panel for both suction cases, shown in Figure 8.2 (b) and (c). This is expected in the presence of suction.

The non-dimensional suction rate 'C_s', determined by an Aalborg 100 flowmeter, was 4.5E-6. This was determined as the ratio of mass-flow through the suction panel 'Q_s', to mass-flow through the wind-tunnel test-section 'u_eA_T'. No suction flow-rate was directly measured in Figure 8.2 (c), because the flow-meter was found to have a throttling effect on the suction.

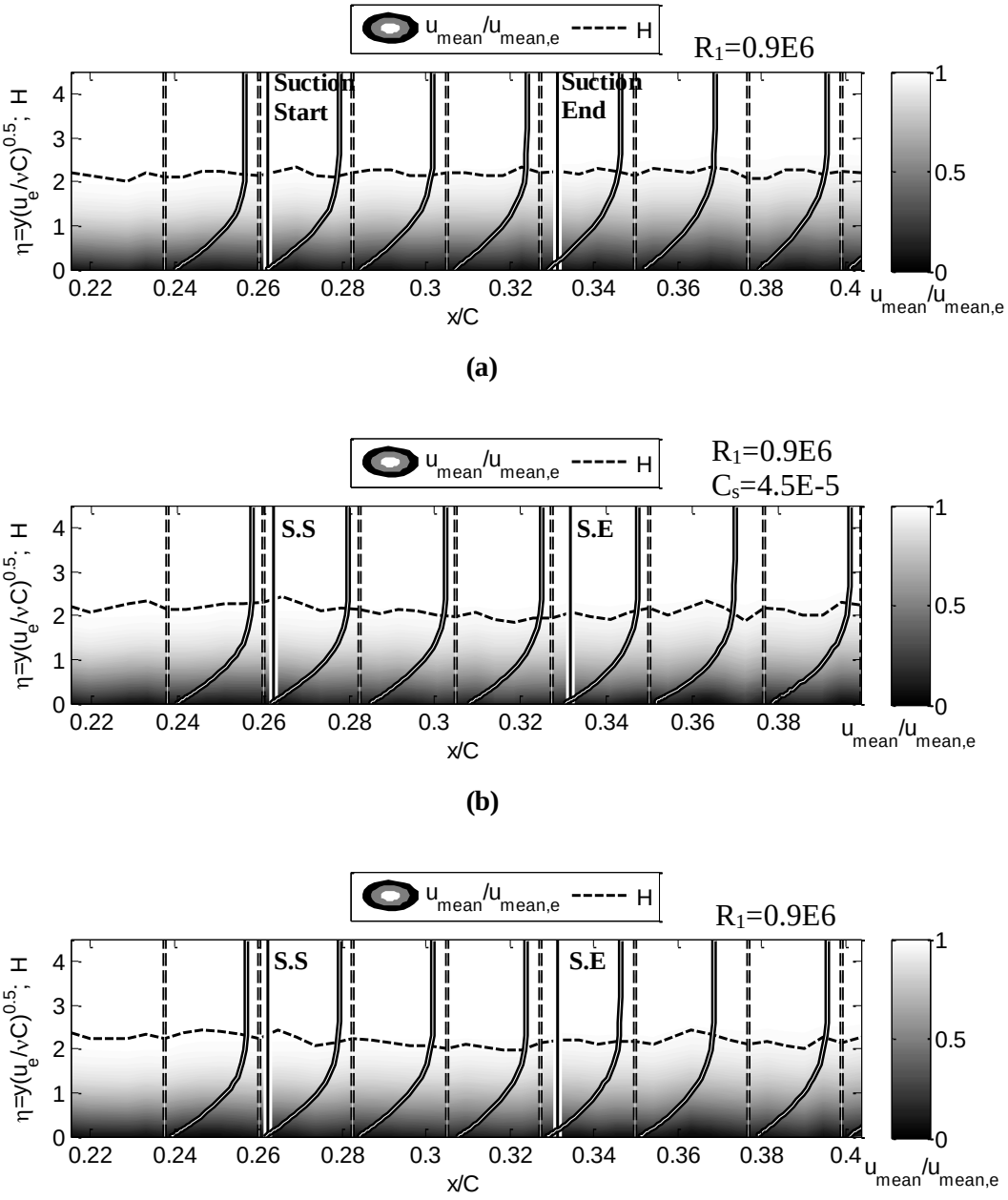

Figure 8.2: Three sets of mean velocity profiles corresponding with different test configurations: (a) flat-plate with no suction or perforations, (b) flat plate with pump driven suction perforations, and (c) flat-plate with suction perforations driven by "natural" pressure gradients. S.S and S.E denote beginning and end of suction array.

8.1.2 Fluctuating Velocity Contours

The excited wave can also be shown directly in an xy-plane through a Fourier reconstruction, the procedure for which is outlined in Section 6.6.3. This wave, at St=19.5, is plotted in Figure 8.3, where the three cases: (a), (b), and (c) correspond to the no-suction, pump driven suction, and natural suction cases illustrated in Figure 8.1.

The plot shows contours of fluctuating velocity 'u'' normalised by the mean velocity at the boundary layer edge 'u_e'.

In Figure 8.3, a non-dimensional frequency parameter 'St=fC/u_e' is used. Here 'u_e' is boundary layer edge velocity, 'f' is dimensional frequency, and 'C' is chord length. The two vertical dotted black lines denote the location of the suction array.

It is noted that in Figure 8.3 (a) that the scale of the colour-map is different from (b) and (c). As in Figure 8.4, Figure 8.3 shows that the excited wave is amplified in (a) but attenuated in (b) and (c). It is notably more strongly attenuated in (b) than in (c).

It is also observed that the flow-structure of the excited wave is slightly different far up-stream (i.e.: x/C=0.21-0.23), the upstream flow-structure is associated with the disturbance near-field, i.e. localised flow-distortion close to the source (the pulsating jet). Similarly the down-stream structures whose shape is characteristic of travelling waves is associated with the disturbance far-field.

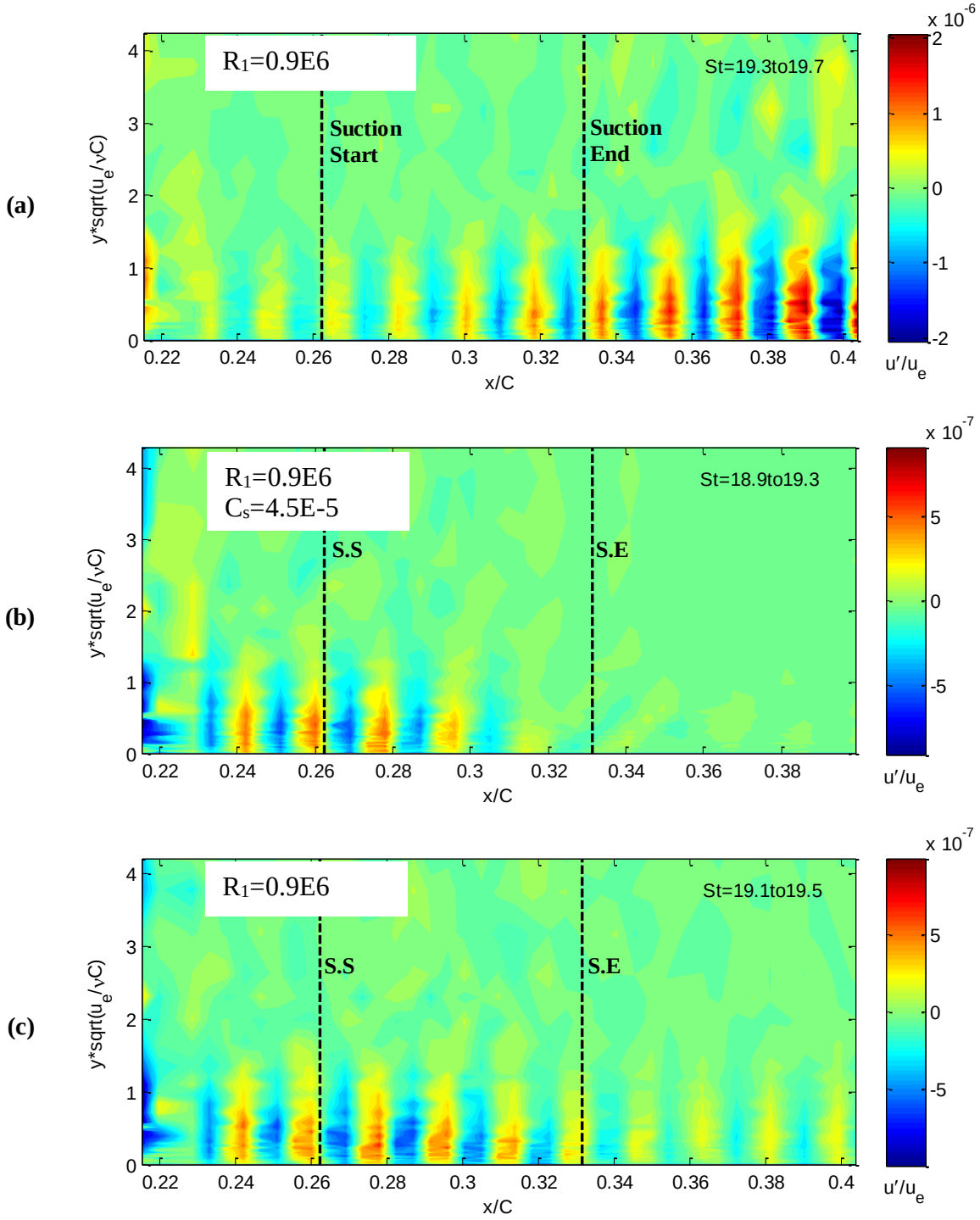

Figure 8.3: Three sets of fluctuating velocity contours corresponding with different test configurations: (a) flat-plate with no suction or perforations, (b) flat plate with pump driven suction perforations, and (c) flat-plate with suction perforations driven by "natural" pressure gradients. Excitation amplitude was $\psi/u_{rms,e}$=0.112.

8.1.3 Spectral Energy Distributions

Figure 8.4 shows the spectral energy distributions that correspond to the cases shown in Figure 8.1 and Figure 8.2. As the early stages of transition from laminar to turbulent flow, is governed by linearly independent waves/modes: it is useful to decompose the energy of the unsteady velocity component 'u'' into a frequency spectrum. This allows the most strongly amplified linearly independent waves to be identified and analysed.

In Figure 8.4 the spectral amplitude 'ψ' is non-dimensionalised with respect to the RMS of the fluctuating velocity component in the free-stream. As these measurements were taken in a two-dimensional plane, 'ψ' is also dependent on the distance from the wall 'y', i.e.: $\psi(x,y)$. In Figure 8.4 'y' is chosen such that $\psi(x,y)\rightarrow\infty$. Here 'x' is the distance from the leading edge. Again non-dimensional frequency is used and is presented as Strouhal number '$St=fC/u_e$'.

In these test cases the boundary layer is excited using a pulsating wall jet. The jet pulsation is only of sufficient amplitude to excite unstable frequencies in the flow, to increase the initial amplitude of travelling waves in the flow. A suitably unstable frequency in the flow was found by empirically varying the frequency of the pulsating jet at the test unit Reynolds number 'R_1'. In Figure 8.4 the frequency of the excited mode was St=19.5. A neutral stability curve was not used to estimate this frequency as one suitable for oblique waves was not available.

The jet was driven by a loudspeaker connected to a surface perforation. The speaker amplitude was defined in volts, however, a more useful estimation of amplitude was obtained by measuring the amplitude at the intersection of the disturbance near and far fields (see Section 8.1.2). Here it was found to be $\psi/u_{rms,e}=0.112$.

In Figure 8.4 (a) it can be seen that the excited wave (at St=19.5) is amplified, where no wall suction is in effect. In contrast it is attenuated in the two suction cases shown in (b) and (c). There is stronger attenuation in (b) which is expected as a result of the stronger suction achieved using the suction pump.

In Figure 8.4 (b) and (c) it can be seen that for St=0-8: there is high spectral energy starting from the beginning of the suction array. This region is absent from Figure 8.4 (a) and is therefore associated with the suction. It also noted that this set of modes is more strongly amplified, over a larger range of frequencies in Figure 8.4 (b), where the suction is stronger. This low frequency disturbance is also observed to be attenuated down-stream from the end of the suction array.

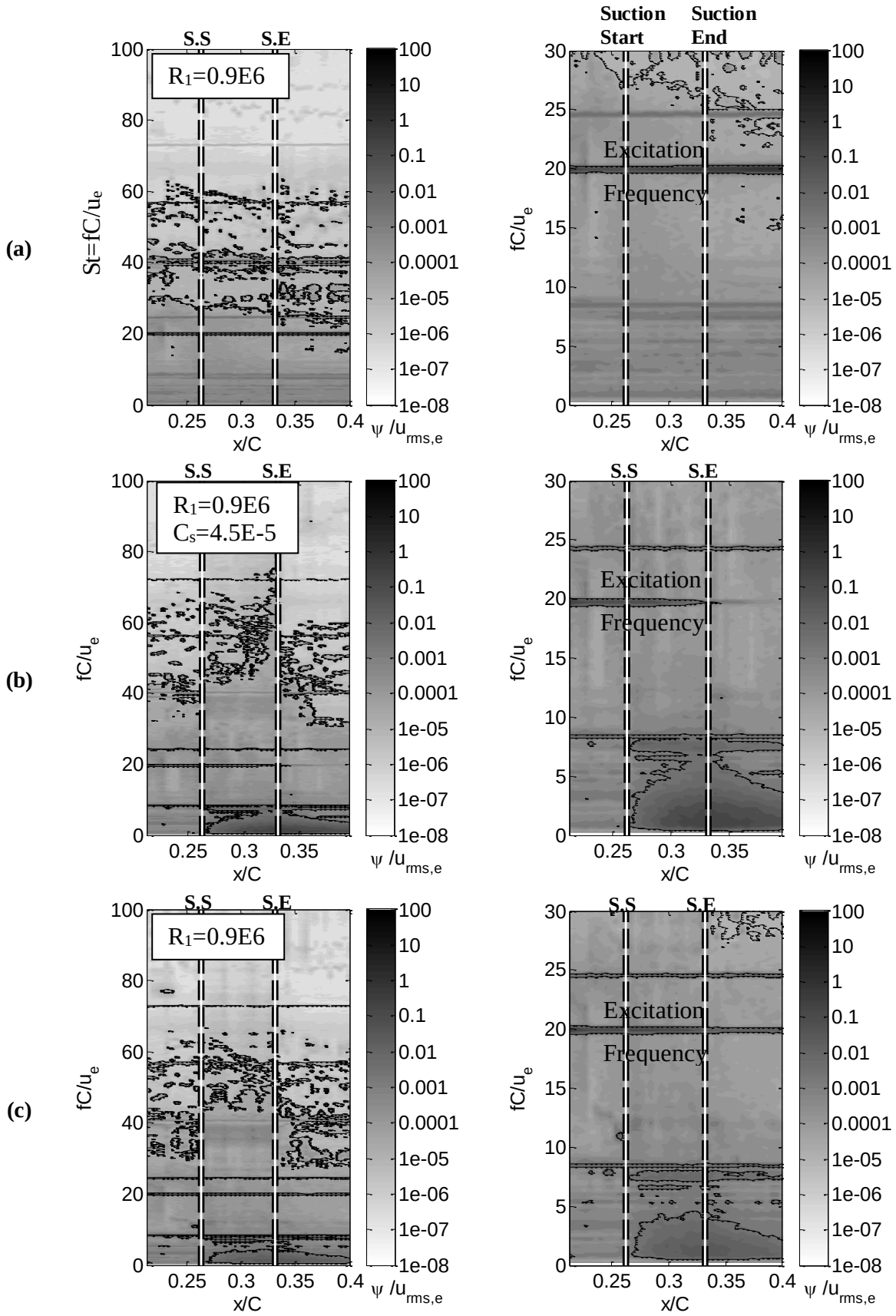

Figure 8.4: Three sets of spectral energy distributions corresponding with different test configurations: (a) flat-plate with no suction or perforations, (b) flat plate with pump-driven suction perforations, and (c) flat-plate with suction perforations driven by "natural" pressure gradients. Excitation amplitude was $\psi/u_{rms,e}$=0.112.

8.2 Significance of Low Frequency Disturbance

The low frequency disturbance reported in Section 8.1 initially appeared benign as it was damped sufficiently down-stream from the suction array. This would indicate that it could only induce laminar-to-turbulent transition over the suction array. This was later proven to be incorrect, as the low frequency disturbance appeared to interact with a pre-established transition front.

8.2.1 Transition Front Close to Suction Panel

Figure 8.5 (a) shows the spectral energy distribution for a case where the excitation frequency (St=32) is sufficiently unstable to cause transition to occur shortly down-stream from the suction panel. The spectral energy is noted to spread from a set of low frequencies as opposed to the excitation frequency, this is characteristic of a N-type transition.

In Figure 8.5 (b), with the addition of some wall-suction, it can be seen that the spatial growth of spectral energy is reduced, which delays laminar to turbulent transition. It can be seen that some spectral energy, at St<20, is weakly attenuated by the suction compared to the remaining frequencies in the spectrum.

From Figure 8.5 (c), it can be seen that the change in transition front position has changed only slightly compared to the change from Figure 8.5 (a) to (b). The exciter signal is more strongly attenuated, but the modes at St<20 are more strongly amplified.

In Figure 8.5 (d), the modes at St<20 are even more strongly amplified, to the point where they are interacting with the exciter signal and causing it to be more strongly amplified than in Figure 8.5 (c). There is a general increase in energy at all frequencies immediately down-stream of the suction array, this appears to be spreading from the modes at St<20. There is no clear change in transition front location, based on the broadening of spectral energy across the frequency domain. Overall, these results suggest that the low frequency disturbance interacts with a pre-established transition front.

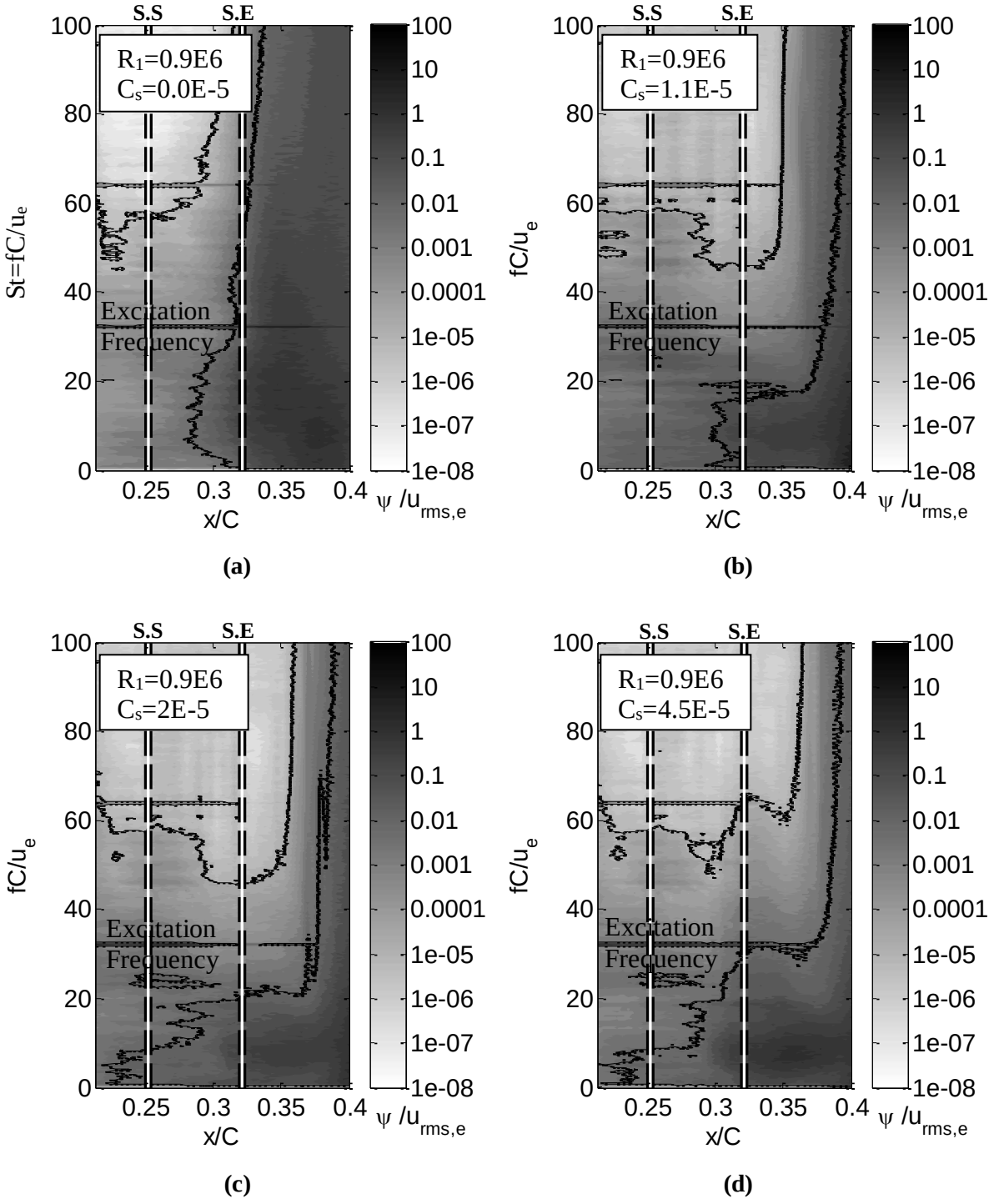

Figure 8.5: Spectral contour plots showing the interaction between discrete suction and a pre-established transition front. (a) shows the case with no suction, (b) shows a case with C_S=1.1E-5, (c) shows a case with C_S=2E-5, (d) shows a case with C_S=4.5E-5. Excitation amplitude was $\psi/u_{rms,e}$=0.1213. S.S and S.E denote beginning and end of suction array respectively.

8.2.2 Transition Front far from Suction Panel

As the low frequency disturbance was found to interact with transition front location, it seemed appropriate to investigate transition-front location as a dependent parameter of 'over-suction'. This would have significant implications on studies in the literature such as Ellis and Poll (1996) and Saric and Reed (1986), where change in transition front location is used to quantify the degree of 'over-suction'.

Thus a different excitation frequency was chosen (St=24), a mode more strongly amplified than shown in Section 8.1.2 but more weakly amplified than in Section 8.2.1. The intention was to pre-establish a transition front within the measurement area (for the base-line no suction case) further down-stream than in Section 8.2.1. A higher forcing amplitude was also used to bring the transition front closer ($\psi/u_{rms,e}$=1.64).

The baseline no-suction case is shown in Figure 8.6 (a), it is noted that the harmonics of the excitation signal are more clearly defined. This is likely due to the stronger forcing; however, it appears as though the transition process is still dominated by a low-frequency N-type transition process. It is noted that compared to Figure 8.5 (a) the transition front is located further down-stream as intended.

In Figure 8.6 (b) it can be seen that the transition front is moved down-stream by the application of a small amount of wall suction (C_s=7E-6). It is noted that the low frequency portion (St<23) of the transition front (associated with oblique modes in N-type transition) is less strongly attenuated than neighbouring frequencies (St>23). It is also noted that the low frequency disturbance has appeared (St<10, x/C=0.3) but is small in amplitude.

It can be seen that for the increased suction case shown in Figure 8.6 (c), the transition-front has moved down-stream of the measurement area. The low frequency disturbance has also grown in amplitude. In Figure 8.6 (d), the suction rate is increased to be consistent with Figure 8.5 (d), this results in observable change on the transition front location. However, this has the effect of further attenuating the excited mode (St=24), and further amplifies the low frequency disturbance (St<15, x/C=0.35).

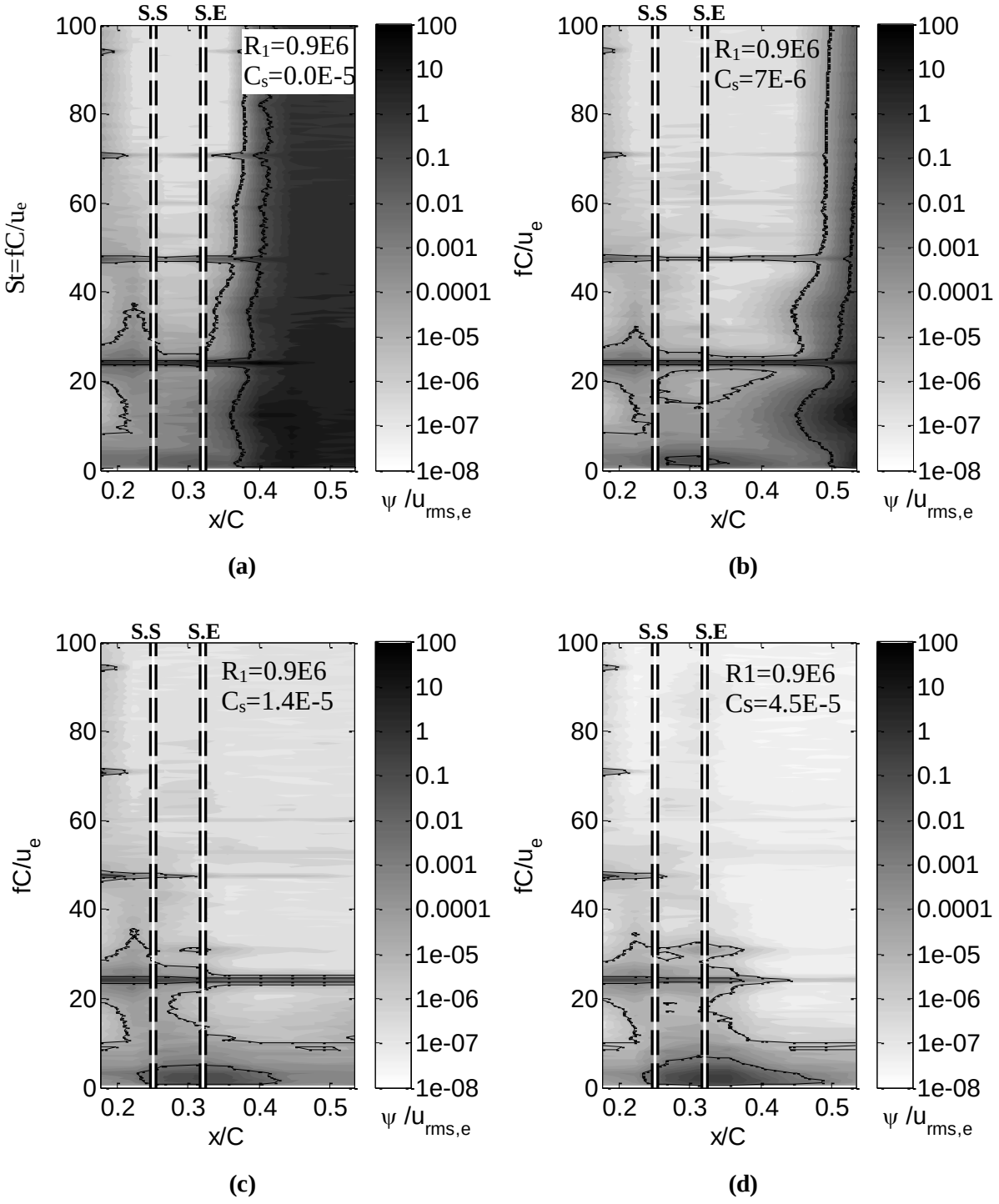

Figure 8.6: Spectral contour plots showing the interaction between discrete suction and a pre-established transition front, set further down-stream. (a) shows the case with no suction, (b) shows a case with C_S=0.7E-5, (c) shows a case with C_S=1.4E-5, (d) shows a case with C_S=4.5E-5. Excitation amplitude was $\psi/u_{rms,e}$=1.64.

The results shown in Figure 8.7 follow the results in Figure 8.6 , in that all the test conditions are the same except for the suction rate which is increased further in Figure 8.7 (a).

In Figure 8.7 (b), the suction rate is increased yet again, and it can be seen that the transition front has returned to the measurement area. It appears as though the spectral energy from the transition front is spreading across the frequency domain, originating from the low frequency disturbance as the transition front develops down-stream. It is also observed that some high frequency modes (St>35) are amplified immediately down-stream of the suction array. Though these do not appear to strongly interact with the transition-front.

Figure 8.7 (c) shows the effect of further increasing the suction rate. It can be seen that the transition front has moved further forward and that the high frequency (St>35) is now interacting with the transition front, it is noted however, that transition is still originating from the low frequency disturbance (St<15).

In Figure 8.7 (d), laminar-to-turbulent transition occurs almost immediately down-stream of the suction array. Here the transition front appears to originate from both low (St<15) and high (St>35) frequency disturbances.

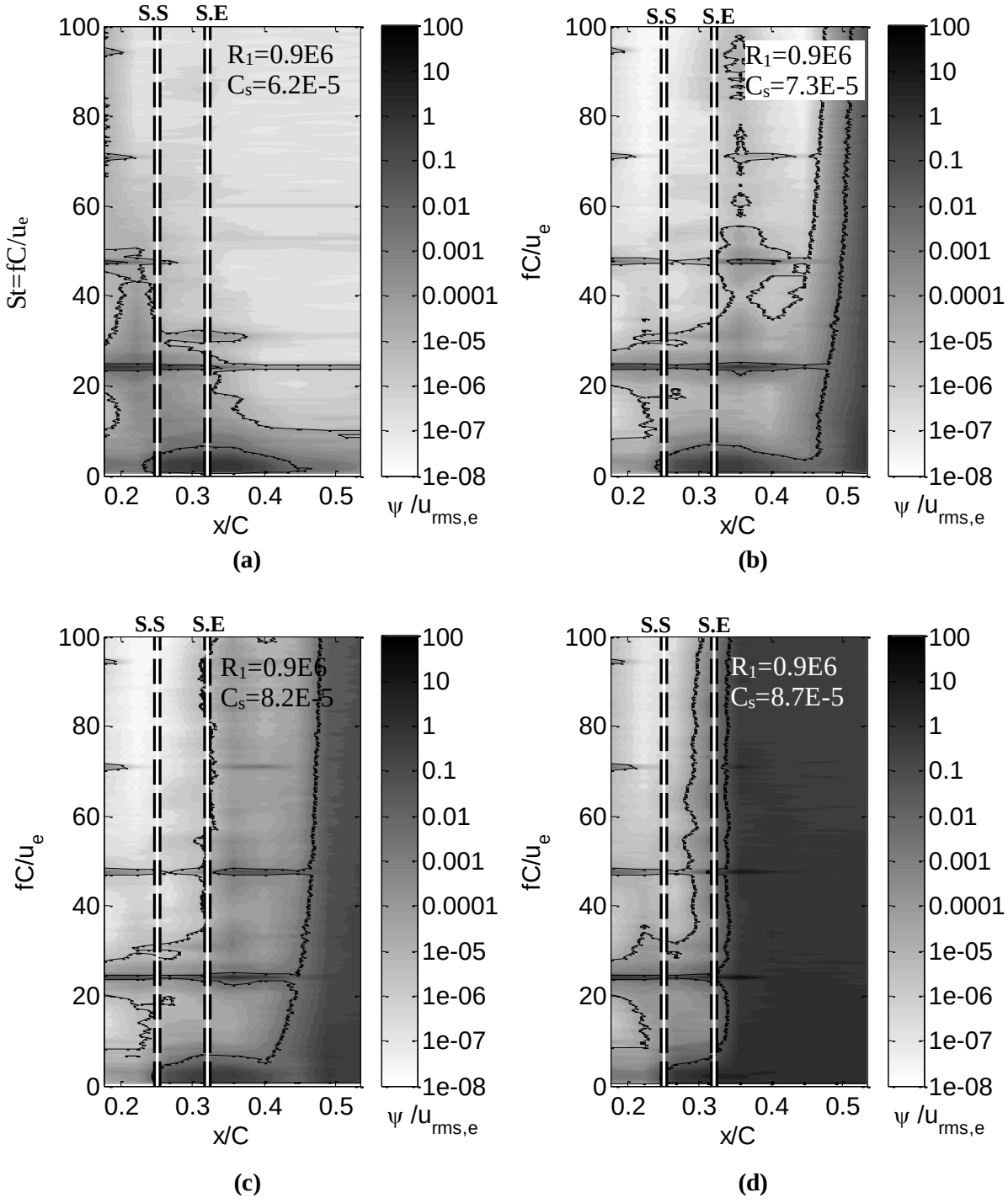

Figure 8.7: Continuation of spectral contour plots showing the interaction between discrete suction and a pre-established transition front, set further down-stream. (a) shows a case with C_S=6.2E-5, (b) shows a case with C_S=7.3E-5, (c) shows a case with C_S=8.2E-5, (d) shows a case with C_S=8.7E-5. Excitation amplitude was $\psi/u_{rms,e}$=1.64.

It is also useful to show mean velocity profiles and distributions associated with the spectral energy distributions shown in Figure 8.6 and Figure 8.7. This is to give another indication of where the transition front is located, and the effect of the suction on the shape of velocity profiles across the wall normal, i.e.: 'u(η)'.

Figure 8.8 shows distributions of mean velocity in the boundary layer, velocity profiles (u{η}) are shown at a number of stream-wise stations (in 'x/C'). The profiles are marked in a white on black solid line, where their origins are marked with a white on black dotted line. The two vertical black lines denote the beginning and end of the suction array, and the dashed horizontal line denotes shape factor.

In Figure 8.8 (a) it is clear the flow starts to become turbulent from an 'x/C' location of 0.45. This is due to the change in the profile shape: showing the development of a log-law region and viscous sub-layer. Furthermore, a relatively sudden drop in shape factor is characteristic of the late stages of laminar-to-turbulent transition. Figure 8.8 (b) shows the effect of adding some weak wall-suction, 'C_s=0.7E-5'. This suction has the effect of moving the transition front down-stream of the measurement area, and causing a small drop in shape factor across the suction array. This is attributed to the flow being accelerated towards the wall as part of the wall-suction.

If the suction rate is increased tenfold, as in Figure 8.8 (c), it can be seen that the transition front has moved forward sufficiently to cause a drop in shape factor at the end of the measurement area. A larger drop in shape factor is also noted across the suction array.

In Figure 8.9 (a), the suction rate is further increased to 'C_s=8.2E-5'. This moves the transition front further forward, as indicated by the earlier drop in shape factor. Here it is noted that the drop in shape factor across the suction array is larger, but more significantly: a stream-wise velocity profile (u{η}) inflection point is observed near the end of the suction array at 'x/C=0.32'.

Figure 8.9 (b) shows that with only a slight increase in suction rate 'C_s=8.7E-5', the transition front moves forward to just slightly down-stream of the suction array end ('x/C=0.35-0.4'). The persistence of the stream-wise velocity profile (u{η}) inflection point near the suction array end is also noted.

(a)

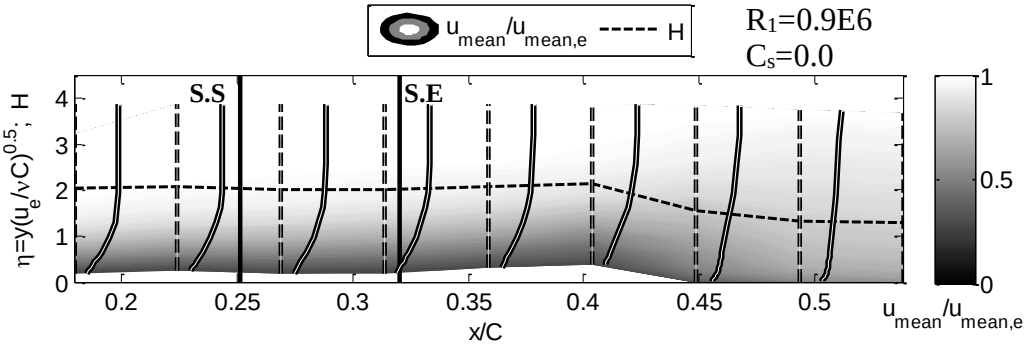

(b)

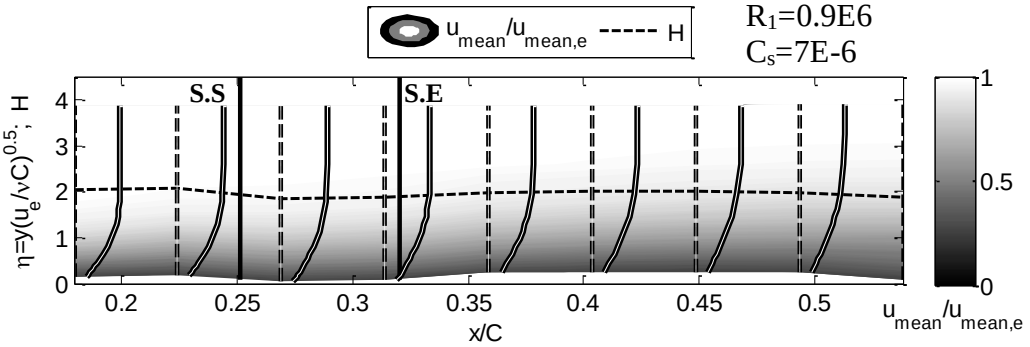

(c)

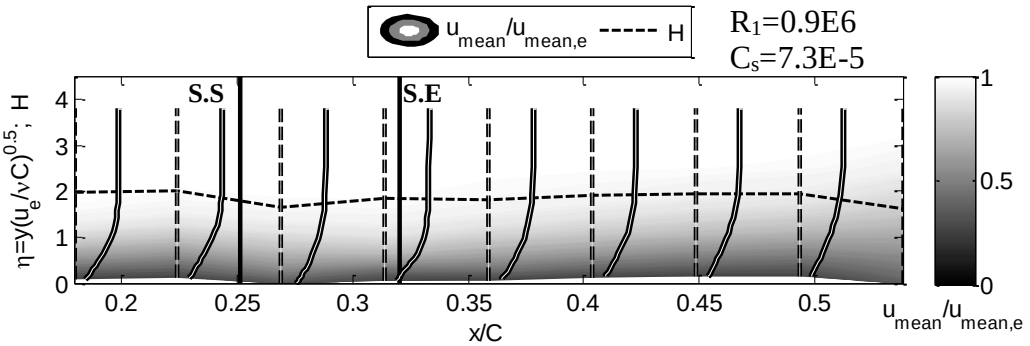

Figure 8.8: Mean velocity contour plots for different suction rates (a)-(c), at the same unit Reynolds number. Velocity profile shapes and their origins are super-imposed through white-on-black lines.

(a)

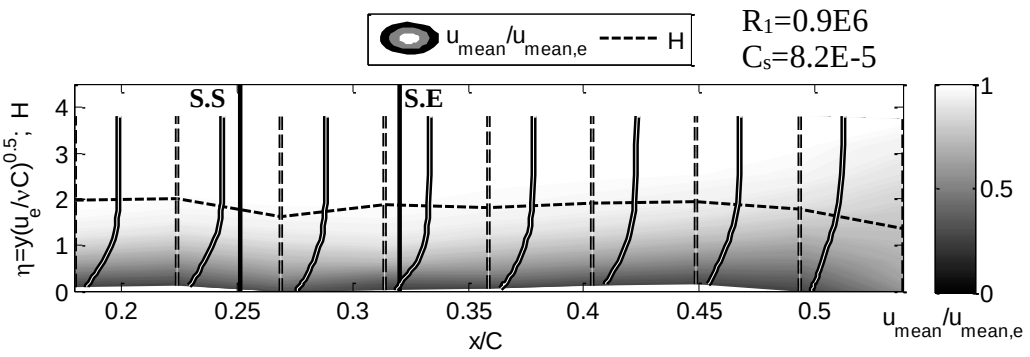

(b)

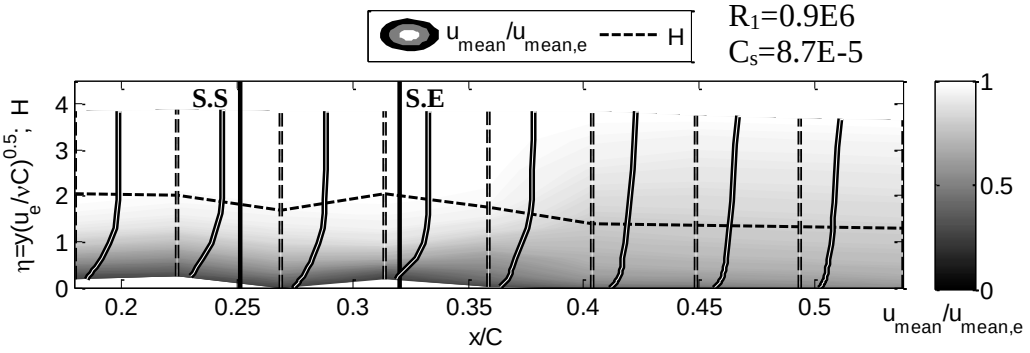

Figure 8.9: Mean velocity contour plots for different suction rates (a)-(b), at the same unit Reynolds number. Velocity profile shapes and their origins are super-imposed through white-on-black lines.

8.3 Significance of the High Frequency Secondary Wave

In Section 8.2.2, it was shown that some high frequency modes become amplified down-stream of the suction array at high suction rates. However, in these measurements the high frequency did not have significant effect on the laminar-to-turbulent transition process. As the spectrum can be seen to spread down-stream from frequencies associated with the low frequency disturbance (St<15). However, these prior studies were performed in the presence of a pre-established transition front. If this transition front is removed it has been found that the high frequency precipitates transition instead of the low frequency.

8.3.1 No Pre-Established Transition Front

Figure 8.10 (a) shows a spectral energy contour plot, with no excitation of the boundary layer. Effectively this means that there is no pre-established transition front without the addition of wall suction. The suction coefficient 'C_s' and free-stream Reynolds number 'R1' are consistent with the case shown in Figure 8.7 (d). This allows a direct comparison of the effect of removing the transition front. Here spectral energy starts to spread across the frequency (for increasing 'x/C') starting at '60<St<100', instead of at 'St<10'.

There are some errors in Figure 8.10 (a), a problem with the suction pump was that it needed to time to cool down during the experiments. A delay of 2 minutes was required to avoid transient effects after the pump was restarted when the low frequency dominated the transition process 'St<10'. For the high frequency it was found these structures had a much larger transient region after restarting the pump. Here a delay of 15 minutes was required. See Appendix A.5 for more details on the suction pump cooling.

Discontinuities in Figure 8.10 (a) and Figure 8.10 (c) are marked by dashed ellipses. It can be seen that they are associated with transients on the high frequency disturbances 60<St<100'. The difference in delay time could suggest that the low frequency disturbance is a form of primary wave and the high frequency is a secondary wave. Secondary waves would require that the primary wave be established first.

A sufficiently long delay after a suction cool-down cycle was provided in Figure 8.10 (b) and Figure 8.10 (d). The only other change in this test case, was that a higher suction coefficient was used. It can be seen in Figure 8.10 (b) that the spectral energy starts to spread across the frequency at an earlier 'x/C' location. Furthermore the shape factor drops sooner in Figure 8.10 (d) which indicates that the mean profile shape is changing to be characteristic of a turbulent flow.

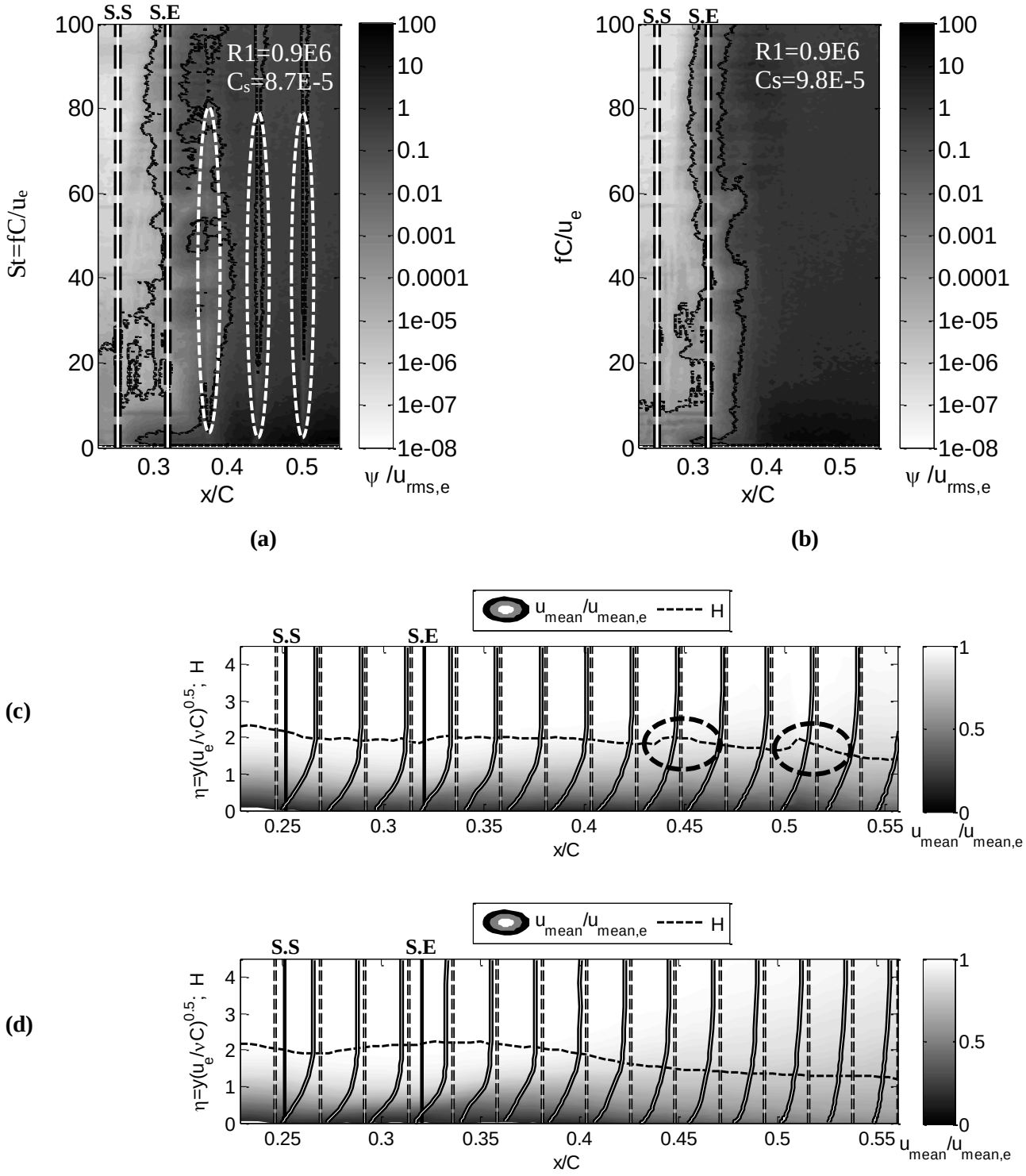

Figure 8.10: Spectral contour plots showing the transition process induced by discrete suction perforations in the absence of a pre-established transition front. (a) has the same Reynolds number and suction coefficient as Figure 8.7 (d). (b) is a higher suction rate. It is noted that there are some transient errors (white dashed ellipses) due to pump cool down cycles in (a) that have been rectified in (b). (c) and (d) are mean velocity contour plots that correspond to cases shown in (a) and (b) respectively.

8.4 Onset of Low and High Frequency Disturbances

The onset of the low and high frequency disturbances has been observed to be different. The change in the amplitude of these disturbances is shown in Figure 8.11. Here the integrated sum of the growth of the low frequency across the suction panel ($0.25<x/C<0.32$) is shown on the y-axis, where 'δx' is the step size for the integration. 'A' is the disturbance amplitude 'u_{rms}' filtered between $0.3<St<6$, and A_0 is the minimum amplitude in the stream-wise direction 'x'. This integrated sum of u_{rms} is plotted against the suction coefficient 'C_s'.

In the case of the low frequency disturbance it is observable at all suction rates, and appears to scale with increasing suction rate (in Figure 8.11). The high frequency only appears at a sufficiently high non-dimensional suction rate. Both appear to grow (approximately) log-linearly with increasing suction rate. The difference in onset might suggest that the low frequency disturbance is a set of primary instability waves, and the high frequency a set of secondary instability waves.

(a)

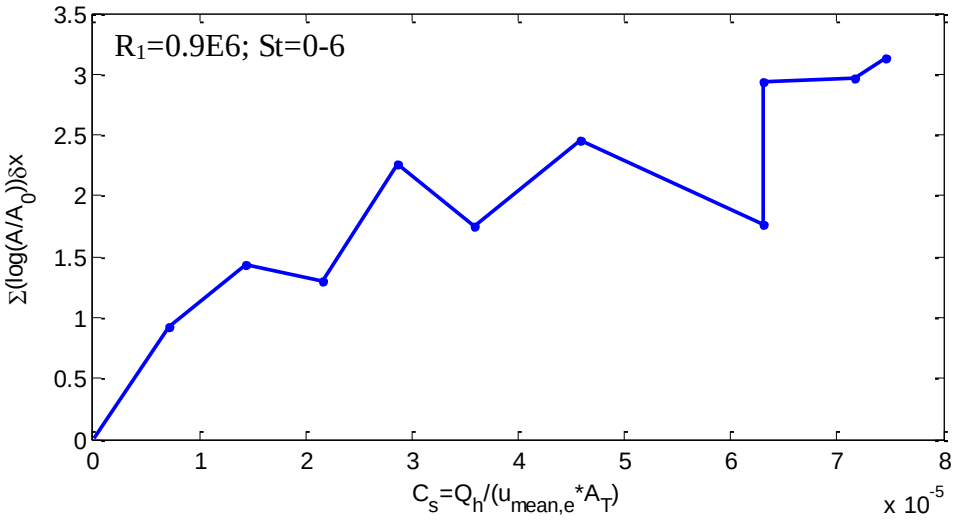

(b)

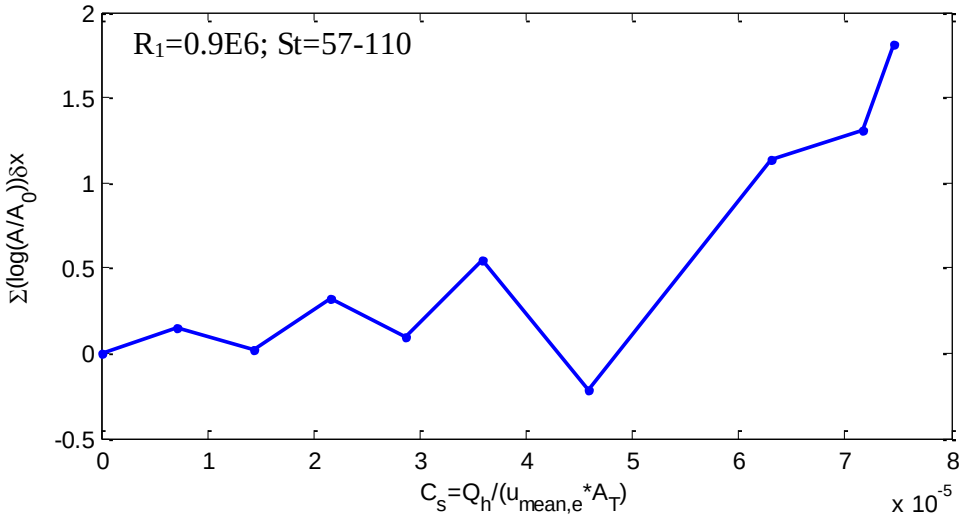

Figure 8.11: Change in integrated amplitude of the low frequency disturbance (a) and the high frequency disturbance (b) for different suction rates at a prescribed Reynolds number.

8.5 Reynolds Number Dependence

It is of interest to see if the low frequency disturbance changes depending on Reynolds number, as this helps to show confidence that the disturbance is not contained to a narrow band of test cases. Figure 8.12 shows the integrated sum of the growth of the low frequency across the suction panel ($0.25<x/C<0.32$) on the y-axis, where 'δx' is the step size for the integration. 'A' is the disturbance amplitude 'u_{rms}' filtered between $0.3<St<6$, and A_0 is the minimum amplitude in the stream-wise direction 'x'. This integrated sum of u_{rms} is plotted against the suction coefficient 'C_s'.

It can be seen that there is good collapse between the different unit Reynolds number 'R_1' cases. This could indicate some Reynolds number independence which would suggest that this low frequency disturbance is an inflectional/inviscid instability (Schlicthing 1977). Thus it is logical to look for inflection points in mean velocity profiles as a source for this disturbance.

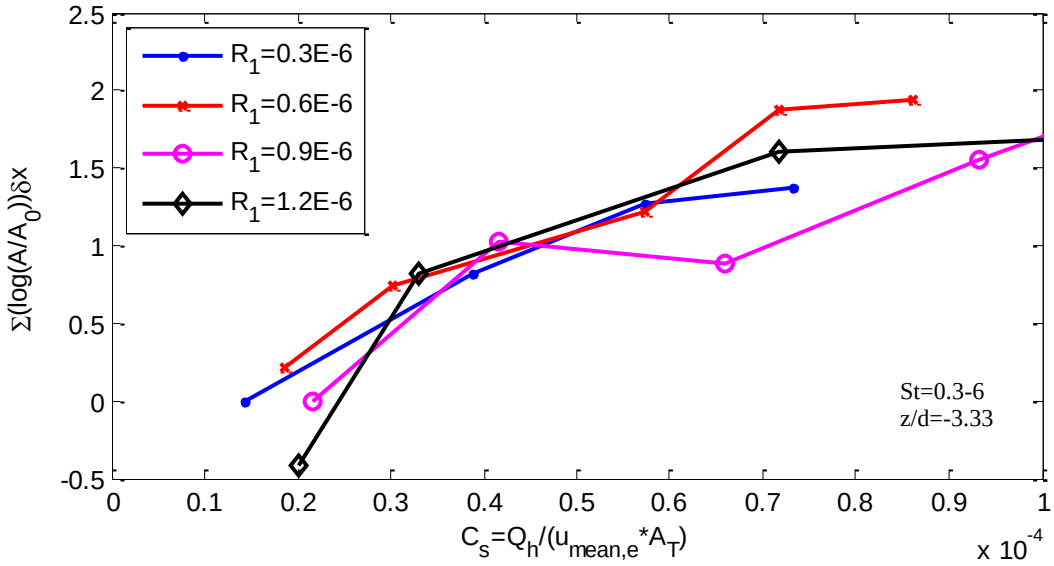

Figure 8.12: Growth rate of low frequency disturbance at different Reynolds numbers.

8.6 Structure of Disturbance Fields

The importance of both the high and low frequency disturbances and their roles in the two different transition processes observed in Sections 8.2 and 8.3 has been demonstrated. To fully understand these processes, it is necessary to identify the cause and nature of the low and high frequency disturbances. To achieve this detailed measurements of the structure of these disturbance fields were taken and compared with the literature.

8.6.1 Structure of Low Frequency Disturbance

The amplitude of the low frequency disturbance was periodic across the span, this can be seen in Figure 8.13 (a). Here the amplitude of low frequency disturbance 'u_{rms}' is super-imposed upon the gradient of the non-dimensional mean stream-wise velocity across the span '$\frac{d}{u_{mean,e}}\frac{du_{mean}}{dz}$'.

This simply shows that the periodicity of low frequency disturbance is strongly correlated with inflection points in the stream-wise velocity profile across the span. Here 'd' is the hole diameter which was 0.6mm. 'η' once again is the non-dimensional distance from the wall.

Figure 8.13 (b) shows the variation in span-wise velocity across the span, here contours of the normalised span-wise mean velocity 'w_{mean}' are shown. Profile shapes of normalised 'w_{mean}' are super-imposed to better show the presence of inflection points. These profiles are marked in white on black solid lines, with their origins marked in dashed white on black lines. It can be seen that these profiles are inflectional, mainly due to the span-wise velocity being zero in the free-stream.

Figure 8.13 (c) shows the correlation between the non-dimensional wall-normal gradient of the span-wise velocity '$\frac{1}{w_{mean,e}}\frac{dw_{mean}}{d\eta}$' and the amplitude of the low-frequency disturbance 'u_{rms}'.

There appears to be some correlation present, though it is much weaker than is seen in Figure 8.13 (a). Regions of correlation are highlighted with black ellipses.

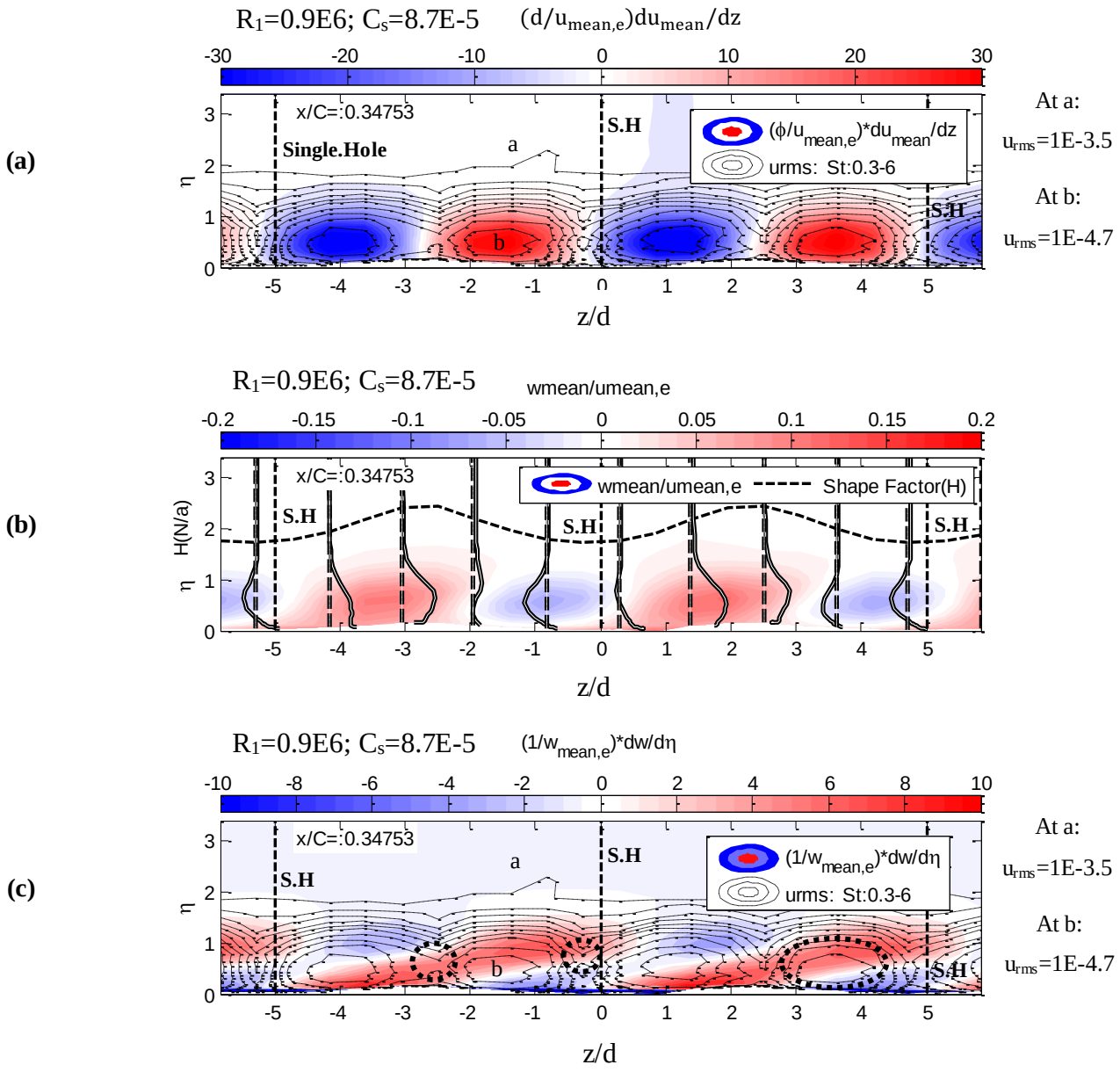

Figure 8.13: Span-wise contour plots showing different quantities relating to mean velocity.
(a) shows the non-dimensional gradient of mean stream-wise velocity across the span.
(b) shows mean span-wise velocity profiles and contours.
(c) shows the non-dimensional gradient of mean span-wise velocity across the wall-normal.
Plots (a) and (c) are correlated with the low frequency disturbance.

The span-wise velocity gradient across the wall-normal was also correlated with the stream-wise growth rate of the low frequency, in Figure 8.14. Here it can be seen that there is strong correlation, suggesting that the growth rate of the low frequency 'u_{rms}' changes with the span-wise velocity gradient.

Due to the prohibitively large number of data-points required to determine '$\frac{d}{u_{mean,e}}\frac{du_{mean}}{dz}$' with a comparable number of stream-wise measurement locations, a similar correlation for the term was not resolved. Attempts found that on the obtained three-dimensional datasets there was too much scatter to make any clear conclusions.

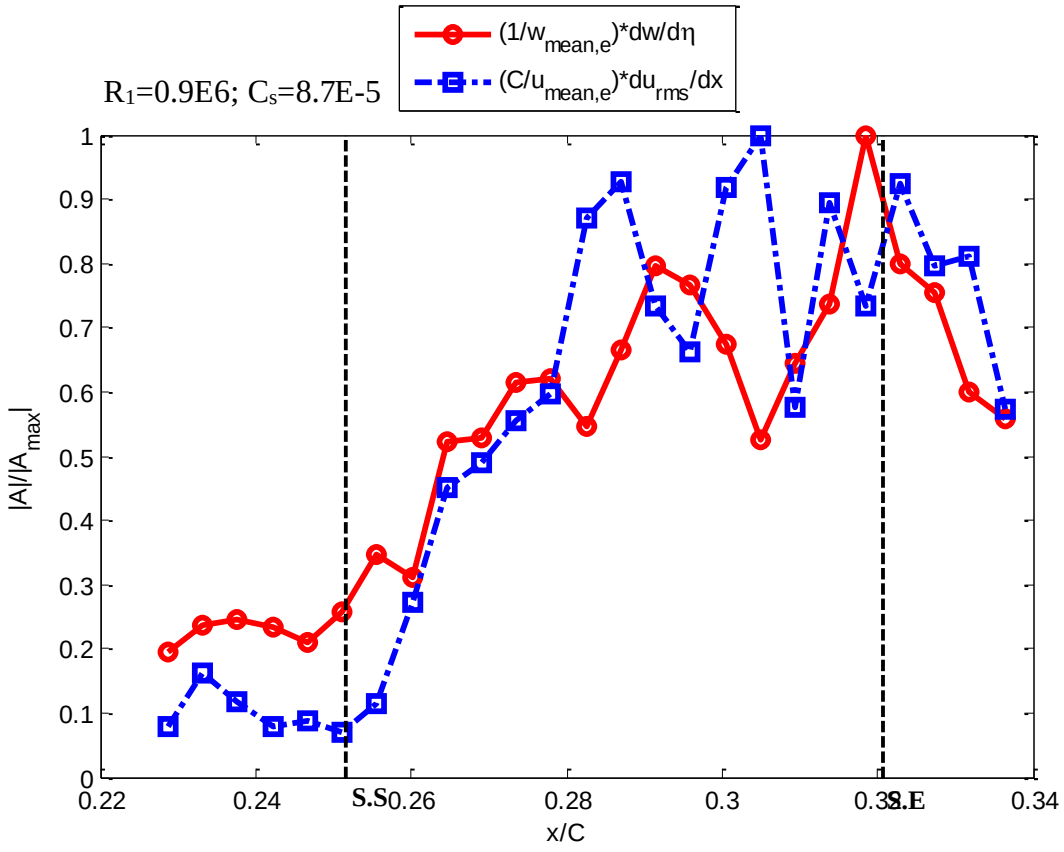

Figure 8.14: Correlation between the stream-wise growth rate of the low frequency disturbance (St=0.3-6) and the span-wise velocity gradient across the wall-normal. Both quantities are normalised to provide an easier comparison. z/d=-3.33.

To better show correlation between u_{rms} and $\frac{1}{w_{mean,e}}\frac{dw_{mean}}{d\eta}$, the effect of $\frac{d}{u_{mean,e}}\frac{du_{mean}}{dz}$ was subtracted from u_{rms}. The exact relationship is shown below:

$$\text{function} = \{u_{rms}\}/\{u_{rms}\}_{max} - \left\{\frac{d}{u_{mean,e}}\frac{du_{mean}}{dz}\right\}\Big/\left\{\frac{d}{u_{mean,e}}\frac{du_{mean}}{dz}\right\}_{max} \qquad \textbf{Equation 8.1}$$

This function is super-imposed upon coloured contours of $\frac{1}{w_{mean,e}}\frac{dw_{mean}}{d\eta}$ in the plot shown in Figure 8.15. Equation 8.1 is represented by the dashed line contours. Here the vertical black dotted line denotes the location of a suction perforation, the dashed contour lines are the function shown in Equation 8.1. Better correlation can be seen here than in Figure 8.13. The periodicity of $\frac{d}{u_{mean,e}}\frac{du_{mean}}{dz}$ could be a stationary mode, if so, it seems reasonable to subtract its effect when looking at correlating the flow distortion with travelling modes. Here the travelling mode is the low frequency disturbance.

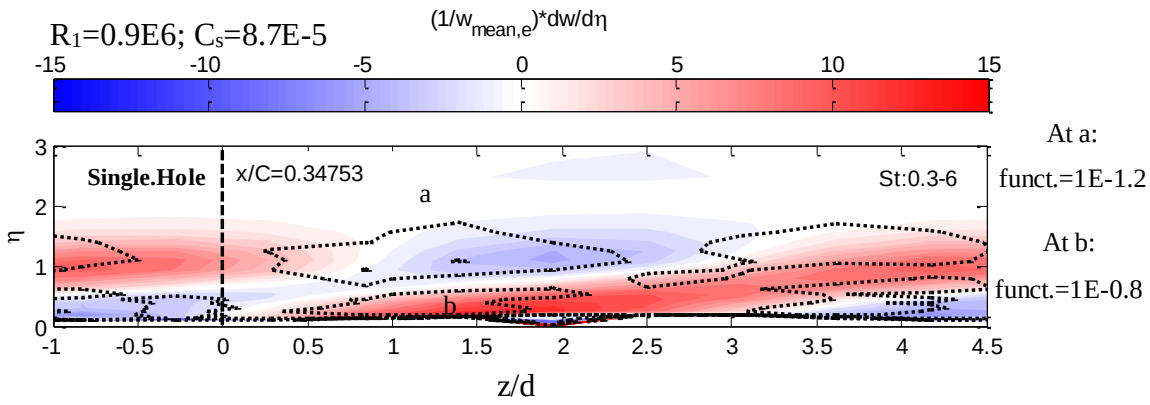

Figure 8.15: Correlation between the gradient of 'w' across 'η' with the low frequency disturbance (St=0.3-6) RMS velocity 'u_{rms}' . u_{rms} has been normalised with respect to itself and the normalised gradient of 'u' across 'z/d' has been subtracted from the field. z/d=-3.33.

In Figure 8.15 there appears to be a phase difference in regions of high normalised u_{rms} and regions where $\frac{1}{w_{mean,e}}\frac{dw_{mean}}{d\eta}$ is large. Otherwise there appears to be good correlation.

8.6.2 Structure of High Frequency Disturbance

The structure of the high frequency disturbance was also investigated to determine its origin. It was compared with span-wise and wall-normal gradients of mean velocity as they have been connected to high frequency breakdown in other vortex dominated transition mechanisms, such as crossflow transition (Poll 1985; White and Saric 2005).

As with the low frequency in Figure 8.13 (a), the amplitude of the high frequency disturbance 'u_{rms}' was found to be periodic across the span, as shown in Figure 8.16 (a). Here the amplitude of high frequency disturbance 'u_{rms}' is super-imposed upon the gradient of the non-dimensional mean stream-wise velocity across the span '$\frac{d}{u_{mean,e}}\frac{du_{mean}}{dz}$'.

Figure 8.16 (b) shows the mean velocity contours of non-dimensional stream-wise velocity. These contours are shown in a span-wise/wall-normal plane. Super-imposed upon these contours are the profile shapes. It can be seen that at only specific span-wise locations these profiles are inflectional.

In Figure 8.16 (c), contours of the gradient of the mean stream-wise velocity (across the wall-nromal) '$\frac{1}{u_{mean,e}}\frac{du_{mean}}{d\eta}$' are shown. Super-imposed upon these contours are contours of the amplitude of the high frequency disturbance 'u_{rms}'. Here only weak correlation is observed compared to Figure 8.16 (a). Some of the regions of correlation are marked with the black dashed ellipses.

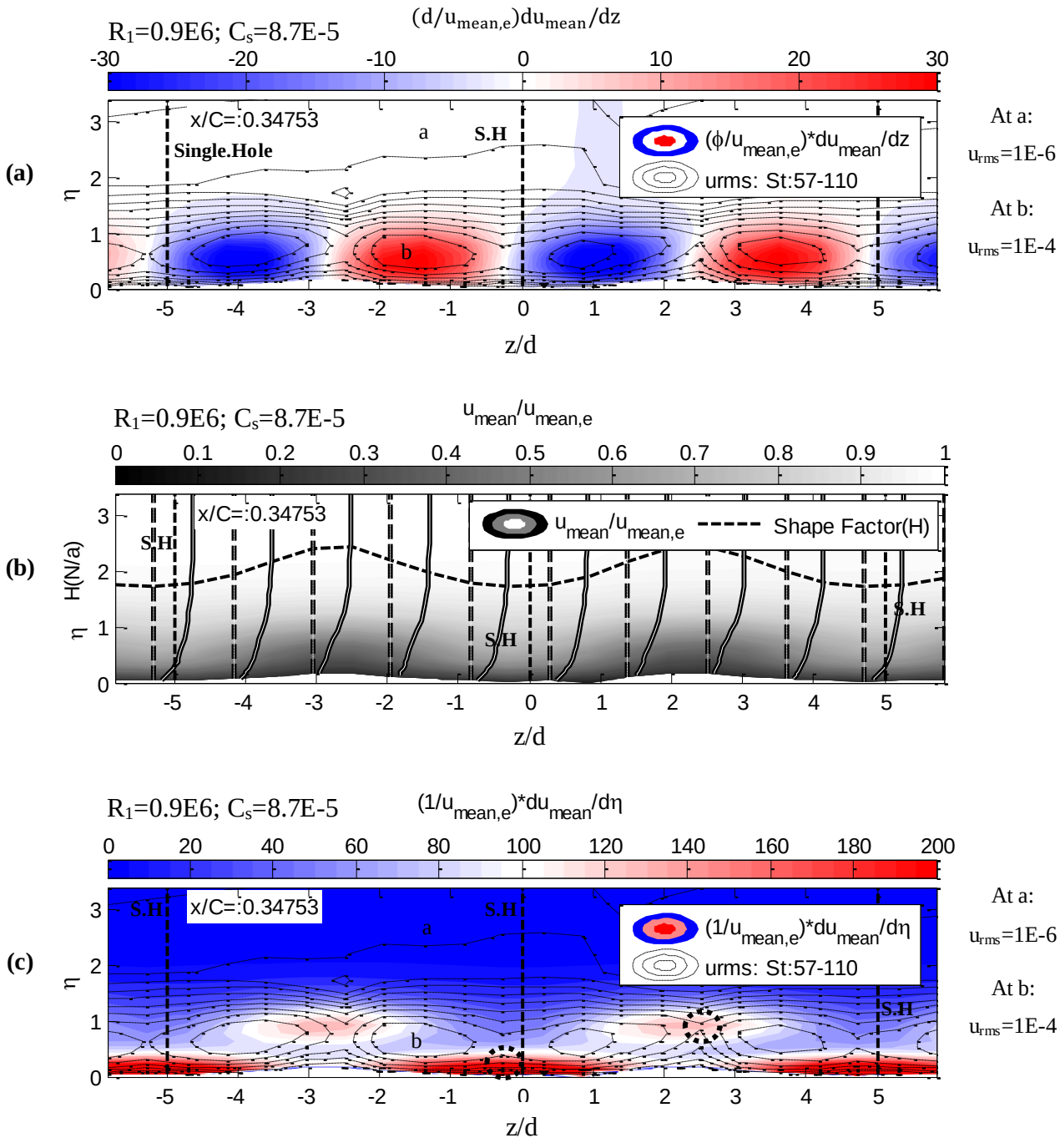

Figure 8.16: Span-wise contour plots showing different quantities relating to mean velocity.
(a) shows the non-dimensional gradient of mean stream-wise velocity across the span.
(b) shows mean stream-wise velocity profiles and contours.
(c) shows the non-dimensional gradient of mean stream-wise velocity across the wall-normal.
Plots (a) and (c) are correlated with the high frequency disturbance.

The stream-wise velocity gradient across the wall-normal '$\frac{1}{u_{mean,e}}\frac{du_{mean}}{d\eta}$' was also correlated with the stream-wise growth rate of the high frequency $\frac{C}{u_{rms}|_{max}}\frac{du_{rms}}{dx}$, in Figure 8.17. Here the correlation is not as obvious as in Figure 8.14. If the value of the red line is high or increasing, this indicates the presence of a favourable pressure gradient. If it is low or decreasing this indicates the presence of an adverse pressure gradient or inflectional velocity profile.

It can be seen that before the suction panel, denoted with the vertical black line, there is a weak adverse pressure gradient, indicated by the drop in gradient at location 'i'. Once on the suction panel, there is a sudden increase in gradient at location 'ii'. This is a favourable pressure gradient associated with the addition of wall-suction.

However, at location 'iii' the gradient starts to drop gradually, this is associated with the appearance of a stream-wise inflection point. It can be also seen that the growth rate of the high frequency starts to increase exponentially as soon as the profile starts to become inflectional.

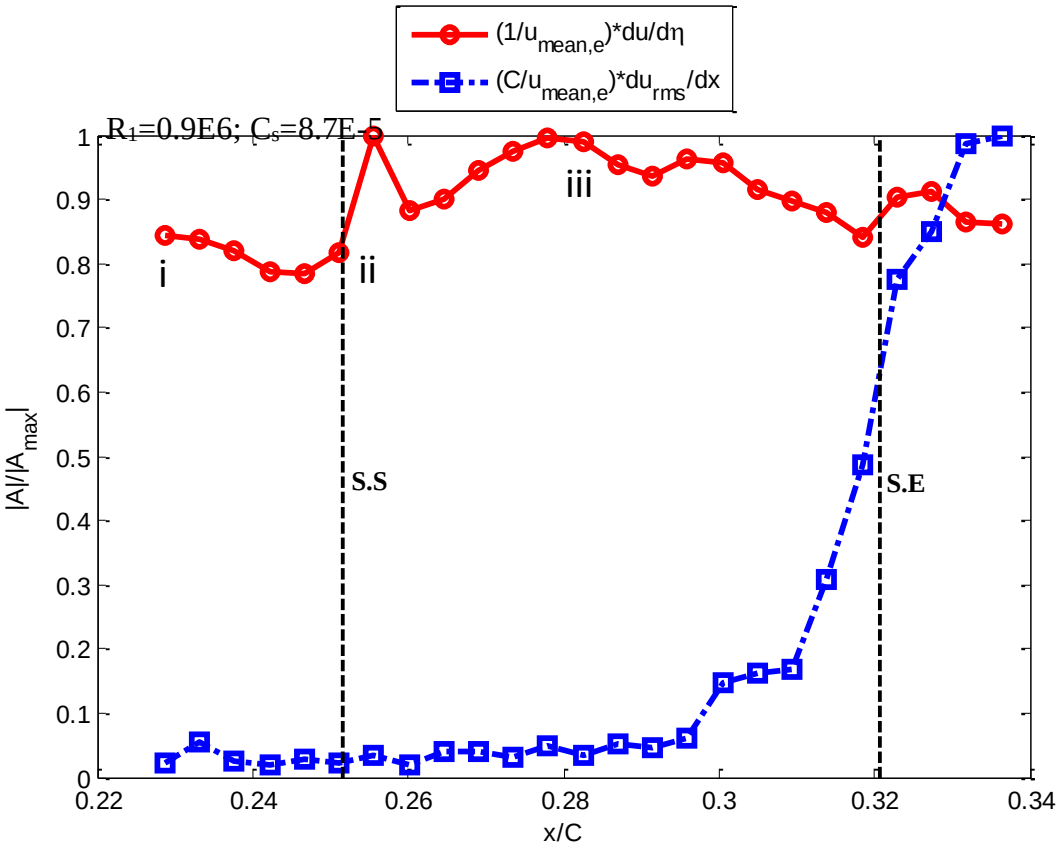

Figure 8.17: Correlation between the stream-wise growth rate of the high frequency disturbance (St=57-110) and the stream-wise velocity gradient across the wall-normal. Both quantities are normalised to provide an easier comparison. z/d=-3.33.

8.7 Comparison of Single Perforation with Perforation Array

In all previously shown results (with suction), the entire suction array (consisting of 1313 perforations) was in use. Here, in this section, the differences in terms of flow structure between an array of widely spaced perforations (based on criteria specified by Reneaux and Blanchard (1992)) and an isolated suction perforation are highlighted.

8.7.1 Frequency Range of High Frequency Disturbance

For the suction perforation array, it was found that for a given unit Reynolds number, the frequency of the high frequency disturbance did not appear to vary with changes in suction rate (see Section 8.3). However, when an isolated suction perforation was studied it was found that the frequency would scale with increasing suction rate. This is shown in Figure 8.18 and Figure 8.19, again these plots show contours of spectral energy of the fluctuating velocity distributed across frequency, in and xy-plane. The shown levels correspond with maximum amplitude along the y-normal for a given frequency and x location.

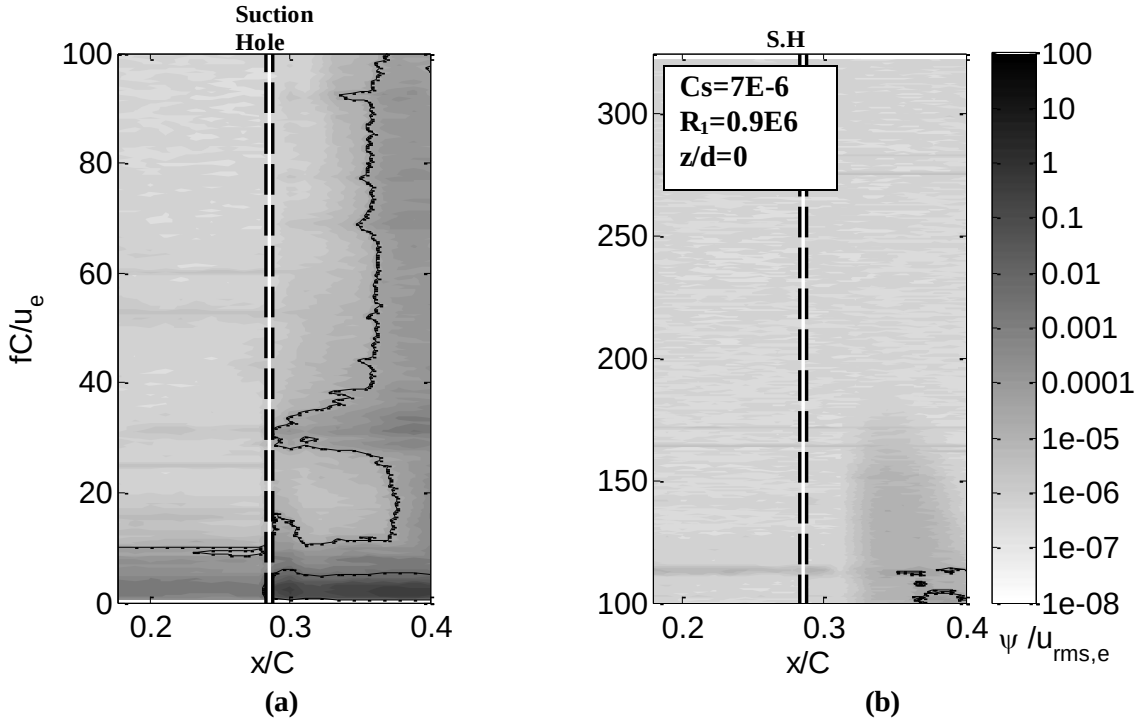

Figure 8.18: Spectral contours of normalised fluctuating velocity, single perforation cases are shown taken along the centreline of the perforation. (a) and (b) show different frequency ranges. No forcing was used.

This change in frequency has been attributed to the wavelength of the suction vortices being constrained by the spacing of the suction perforations. For an isolated suction perforation, no such constraint is present, thus the vortex wavelength changes with suction rate, which changes the frequency of the high frequency disturbance. This change in the vortex wavelength can be inferred from Figure 8.21. This is explained further in Section 8.7.2

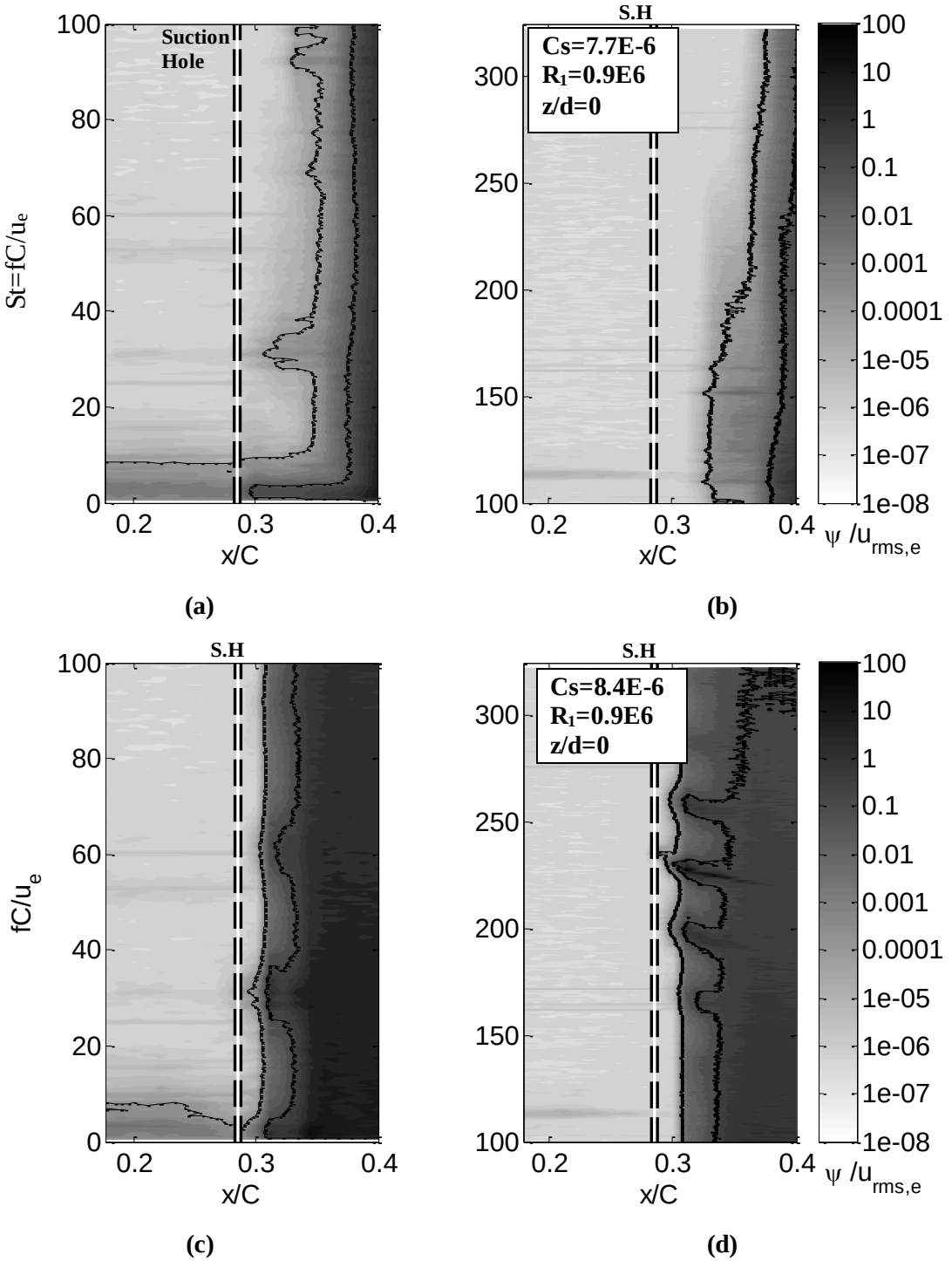

Figure 8.19: Spectral contours of normalised fluctuating velocity, single perforation cases are shown taken along the centreline of the perforation. (a,c) and (b,d) show different frequency ranges. No forcing was used. (a,b) and (c,d) show different non-dimensional suction rates.

Figure 8.20 shows contours of mean velocity taken along the centre of the perforation. These plots are consistent with the cases shown in Figure 8.18 and Figure 8.19. Inflectional profiles are not observed due to these measurements being taken in the plane of a suction perforation rather than a shed vortex.

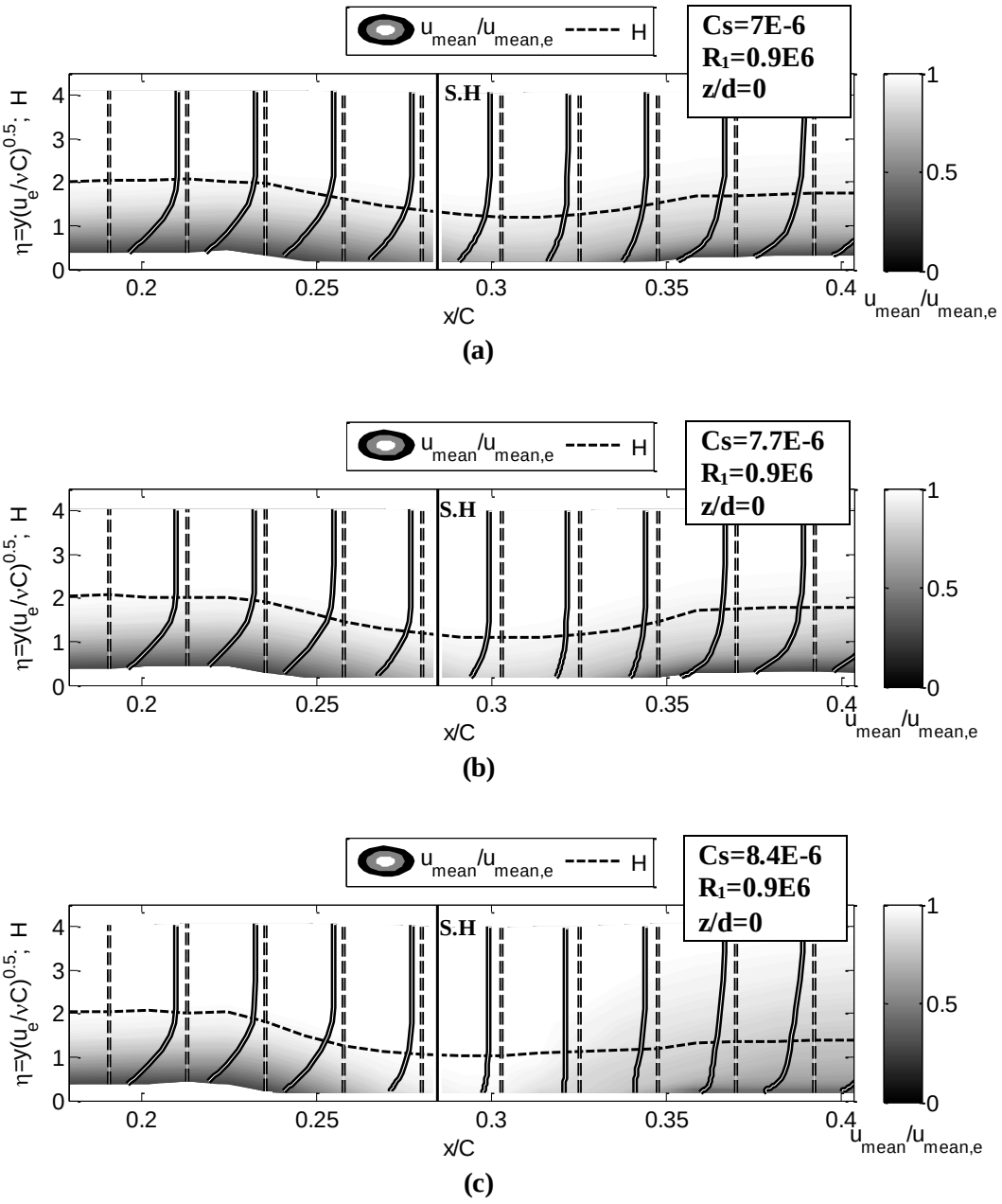

Figure 8.20: Contours of normalised mean velocity (with super-imposed velocity profiles). Single perforation cases are shown, taken along the centreline of an isolated perforation. No forcing was used. (a,b,c) show different non-dimensional suction rates. S.H. denotes the location of the suction perforation.

8.7.2 Strength of Inflection Point across Wall-Normal in Stream-Wise Velocity, u(y)

It was found that when comparing the degree of inflection in the stream-wise velocity profile across the wall-normal, u(y), that the amount of inflection required to trigger transition was much greater for the case with the isolated perforation. Figure 8.21 helps to illustrate this difference in the degree of inflection. In Figure 8.21 (a) the inflection points appear to be stronger, however, there are some difficulties with this comparsion.

There appears to be a periodic structure in Figure 8.21 (b), this can be seen by the two maxima in shape factor at z/d≈-3 and z/d≈2. Only one maxima can be seen in Figure 8.21 (a), at z/d≈-7. The span-wise extent of the distortion of shape factor in Figure 8.21 (a) is much larger (-8>z/d<0 vs -5<z/d<0), suggesting that if it is a similar structure, it is of greater wavelength.

The non-dimensional span-wise displacement parameter 'z/d' does not scale with the size of the mean flow distortion shown in Figure 8.21. Thus because the distortion wavelength is larger in Figure 8.21 (a): Figure 8.21 (b) cannot be shown on the same scale. Similarly it is apparent that non-dimensional suction rate 'C_s' does not scale with the level of mean flow distortion or the onset of transition.

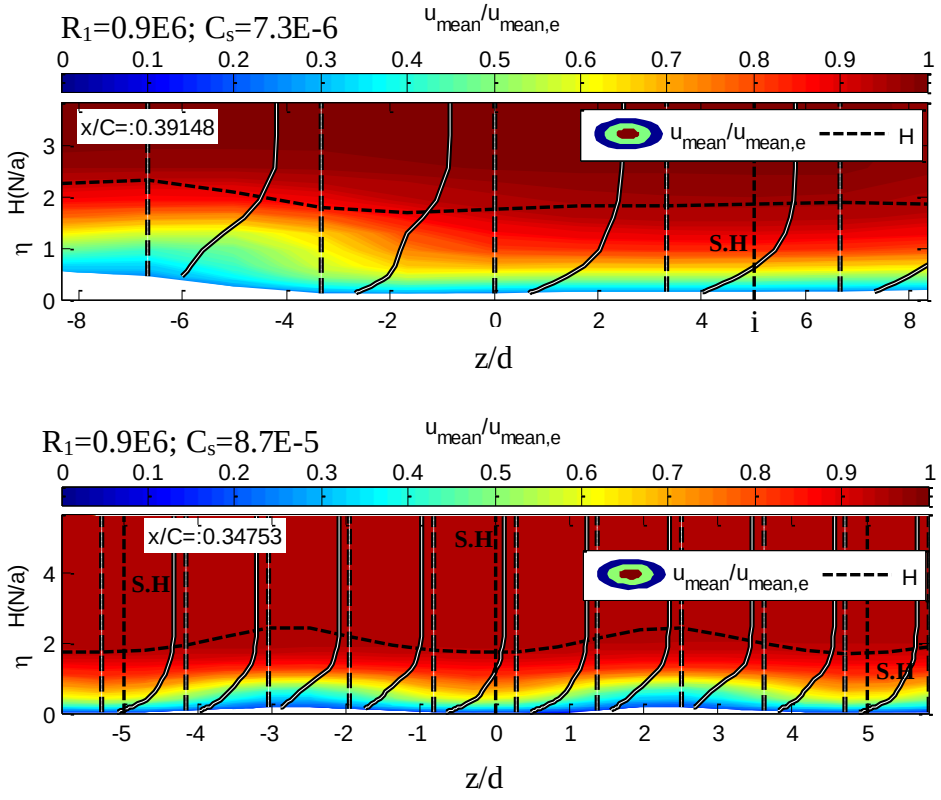

Figure 8.21: Comparison of span-wise velocity contours and profile shapes for: single perforation case (a), and multi-perforation case (b). S.H. (i.e. Suction Hole) denotes the location of suction perforations.

9 Discussion

In all mean velocity measurements shown in Section 8 are found to be within the uncertainties presented in Section 6.6.5. The fluctuating hot-wire signal is well outside the uncertainty of the pressure transducers used to measure dynamic pressure (from which the hot-wire is calibrated). It is believed that the results based the fluctuating velocity should only depend on the residual of the calibration, as it is taken as a perturbation from the mean in the definition of its calibration law (see Section 6.6.1). Furthermore, the low frequency was shown to be repeatable in Appendix B.1.

In this work, a previously unreported low disturbance was found and been shown to correlate with the rate of suction (see Sections 8.1 and 8.4). Initially, this disturbance appeared benign from the perspective of preventing laminar-to-turbulent transition: due to being damped down-stream of the suction array. It has been shown however (in Section 8.2) that this disturbance can interact with a pre-established transition front (established through forcing with a point source). Furthermore, there is evidence to suggest that pre-establishing the transition front in different locations will affect the strength of the interaction. This is an important revelation, as many past studies such as Ellis and Poll (1996) and Saric and Reed (1989) used the transition front location as a measure of the degree of over-suction, in the search for a criterion for when over-suction occurs.

This work also found that in the absence of a pre-established transition front the dominant modes in the weakly non-linear regime were of high frequency (see Section 8.3), when compared to typical Tollmien-Schlichting instability ranges. It was also found that this high frequency was only amplified after a sufficiently high suction rate was reached, whereas the low frequency was amplified for all suction rates (see Section 8.4). Once both sets of modes appeared, their integrated spatial growth was found to be proportional to the suction rate.

In attempting, to identify a source of the high and low frequency disturbances it was found that they were correlated with mean velocity gradients (see Section 8.4). These gradients are indicative of inflectional flow instabilities in their parent profiles. Both low and high frequency were found to be strongly correlated to the change in stream-wise velocity with respect to span-wise displacement 'du_m/dz'. This span-wise gradient is believed to be a stationary mode caused by the counter-rotating vortex pair shed from each suction perforation (see Sections 3.2.3 and 4.1.2).

Furthermore, the low frequency was correlated with gradients of span-wise velocity with respect to the wall-normal 'dw_m/dy'; and the high frequency was correlated with 'du_m/dy'. From comparisons made with the literature presented in Section 3.2.3: it is believed that the low frequencies are destabilised by inflectional 'w(y)' profiles and are analogous to travelling cross-flow modes. Similarly, the high frequency is believed to be analogous to the high frequency secondary instability found in cross-flow studies (i.e. swept wings, see Section 3.2.3), where high frequency is often found to be correlated to 'du_m/dz' and 'du_m/dy' (Malik et al. 1999; Serpieri and Kotsonis 2016; White and Saric 2005). This would suggest that different vortex breakdown based transition mechanisms may be very similar qualitatively.

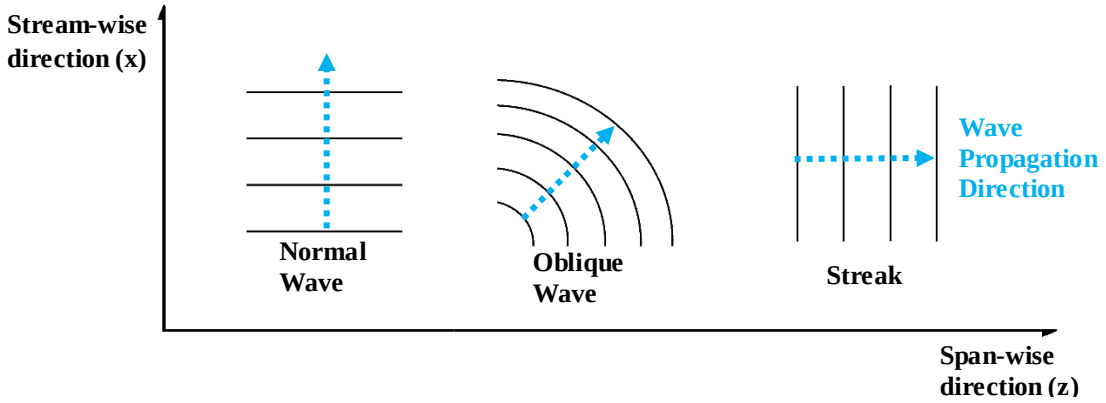

Figure 9.1: Illustration of different types of waves, based on information from Berlin (1998).

The suggestion that the low frequency may be amplified by the inflectional 'w(y)' profiles would explain the interaction between the low frequency from the: N-type transition process, and discrete suction array. The N-type low frequency modes are known from the literature to be attributed to oblique modes that form resonant triads with stream-wise oriented normal modes (Kachanov and Levchenko 1983, see Section 3.2.2). It is logical that the resultant velocity profile associated with u(y) and w(y), will have a three-dimensional distortion of its shape, across the wall-normal. For this reason, it may excite a band of oblique modes, or even streaks if the distortion of w(y) is severe enough. This is apparent in the formulation of the Orr-Sommerfeld-Squire equations where the shape of the resultant of u(y) and w(y) dictates the stability of waves in the flow, for different propagation angles (Schmid and Henningson 2001).

10 Conclusions

A low frequency disturbance was found that is believed to be amplified by inflection points in span-wise velocity profiles across the wall-normal, i.e. w(y). This span-wise velocity component is associated with counter-rotating suction induced vortices.

The low frequency disturbance was found to only be dominant in cases where the transition was fixed a priori by another method of forcing.

Initial Transition front location has been identified as a new critical suction parameter, due to its position affecting the strength of the interaction between the low frequency and the transition front. Development of a fully comprehensive over-suction criterion will require the initial transition front location to be accounted for; this is beyond the scope of this investigation due to difficulties in parametrically varying transition front location in the allotted time for this work.

A high frequency disturbance was found to dominate in the absence of any initial transition front, or where the front was very far down-stream of the suction array. This high frequency is believed to be a secondary instability of the stationary mode 'du_{mean}/dz', and has been found to coincide with inflectional stream-wise velocity profiles across the wall normal '$u_{mean}(y)$'. This stationary mode is associated with the counter-rotating vortex pair shed from each suction perforation.

11 References

Aalborg (2014) GFC Mass Flow Controller: Operating Manual. TD9709M. Rev P.

Alam, M., Sandham, N. (2000) Direct numerical simulation of 'short' laminar seperation bubbles with turbulent reattachment. *J. Fluid Mech.* 410, pp. 1-28.

Atkin, C. (2001a) Review of Porous Panel Over-Suction Criteria. *Dera. HYLTEC*. TR 22.

Atkin, C. (2001b) Suction Chamber Layouts for the A310 Wing: Retrofit and Deisgn-for-Retrofit. *Dera. HYLTEC*. TR 52.

Atkin, C. (2002) 3D Analysis of A310 Wing HLFC Retrofit and Deisgn-for-Retrofit Performance. *Dera. HYLTEC*. TR 81.

Atkin, C. (2010) A New Approach to Designing the Layout of HLFC Chambers. *Dera. HYLTEC*. TR 23.

Baher, H. (1990) *Analog and digital signal processing.* Chirchester: John Wiley and Sons.

Becker (2015) *Side Channel Suction Vacuum Pumps: Double Stage Air-cooled*. Sv. 5.130/2.

Berlin, S. (1998) *Oblique Waves in Boundary Layer Transition.* Ph.D Thesis. Royal Institute of Technology.

Bell, S. (1999) A Beginner's Guide to Uncertainty of Measurement. *National Physical Laboratory: Measurement Good Practice Guide.* 11(2).

Bippes, H. (1999) Basic experiments on transition in three-dimensional boundary layers dominated by cross-flow instability. *Progress in Aerospace Sciences.* 35, pp. 363-412.

Borodulin, V., Kachanov, Y. (1988) Role of the mechanism of local secondary instability in K-breakdown of boundary layer [SIC]. *Izv. Sib. Otd. Akad. Nauk SSSR, Ser. Tekh. Nauk.* 18; 65-77 (In Russian).

Braslow, A. (1999) A History of Suction-Type Laminar-Flow Control with Empahsis [SIC] on Flight Research. *Monographs in Aerospace History.* 13. Washington: NASA History Division.

Bruun, H. (1996) *Hot-wire Anemometry: Principles and Signal Analysis.* Oxford: Oxford University Press.

Butler, S. (1955) Current tests on laminar-boundary-layer control by suction through perforations. *R.A.E. Tech. Note Aero.* 2375.

Cooke, J. (1950) The boundary layer of a class of infinite yawed cylinders. *Math. Proc. Camb. Phil. Soc.* 46(4), pp. 645-648.

Correge Sensors (2019) *Data Sheet Ambient Sensor*. [online]. Accessed: 05 Apr 2019.

Craik, A. (1971) Non-linear resonant instability in boundary layers. *J. Fluid Mech.* 50(2), pp. 393-413.

Dannenber, R., Gambucci, B., Weiber, J. (1956) Perforated Sheets as a Porous Material for Distributed Suction and Injection. *Nat. Advis. Comit. Aero. Technical Note*. 3669.

Ellis, E., Poll. D. (1996) Laminar and laminarizing boundary layers by suction through perforated plates. *2nd European Forum on Laminar Flow Technology, Bordeaux.*

Evans, H. (1968) *Laminar Boundary-Layer Theory*. Addison-Wesley Publishing Company: Reading.

Fox, R., McDonald, A. (1994) *Introduction to Fluid Mechanics.* 7th ed. John Wiley and Sons: New York.

Eppink, J. (2014) *The Interaction of Crossflow Instabilities and a Backward Facing Step in Swept Boundary Layer Transition.* Ph.D thesis, Tufts University.

Falkner, V., Skan, S. (1931) Solutions of the Boundary-Layer Equations. *Lond. Edin. Dub. Phil. Mag. Jor. Sci.* 12(80), pp. 865-896.

Fichter, C., Marquart, S., Sausen, R., Lee, D. (2005) The impact of cruise altitude on contrails and related radiative forcing. *Metrologische Zeitschrift.* 14(4). pp. 563-572.

Gaster, M. (1965a) The role of spatially growing waves in the theory of hydrodynamic stability. *Prog. Aero. Sci.* 6, pp. 251-269.

Gaster, M. (1965b) On the generation of spatially growing waves in a boundary layer. *J. Fluid. Mech.* 22(3), pp. 433-441.

Gaster, M. (1969) The Structure and Behaviour of Laminar Separation Bubbles. *A.R.C. Technical Report*. R.&M. 3595.

Gaster, M., Grant, I. (1975) An experimental investigation of the formulation and development of a wave packet in a laminar boundary layer. *Proc. R. Soc.* 347, pp. 253-269.

Gaster, M. (1997) Flow Distortions Created by Suction. *Progress on DRA.* ASF/2942U.

Gaster, M. (2015) *Private Communication.*

Goldsmith, J. (1956) Investigation of the Flow in a Tube with Laminar Suction through 80 Rows of Closely-Spaced Holes. *Northrop Aircraft*. *Rep*. BLC-86.

Goldsmith, J. (1957) Critical laminar suction parameters for suction into an isolated hole or single row of holes. *Northrop Aircraft*. *Rep*. BLC-95.

Gray, W. (1952) The effect of wing sweep on laminar flow. *RAE TM Aero:* 255.

Gregory, N. (1961) Research on Suction Surfaces for Laminar Flow. *Boundary Layer and Flow Control*. In Lachmann, G. (2), pp. 924-960.

Gregory, N., Walker, W. (1958) Experiments on the Use of Suction through Perforated Strips for Maintaining Laminar Flow: Transition and Drag Measurements. *A.R.C. Technical Report*. R.&M. 3083.

Head, M. Flight experiments on maintaining laminar flow with suction applied through perforations. *Unpublished Ministry of Supply Reports.*

Herbert, T. (1983) Secondary instability of plane channel flow to subharmonic three-dimensional disturbances. *Phys. Fluids.*26, pp. 871-874.

Kachanov,Y., Koslov, V., Levchenko, V. (1977) Nonlinear development of a wave in a boundary layer. *Fluid Dyn*. 12, p. 383.

Kachanov, Y., Levchenko, V. (1983) The resonant interaction of disturbances at laminar-turbulent transition in a boundary layer. *Journal of Fluid Mechanics*. 138, pp. 209-247.

Kachanov, Y. (1994) Physical Mechanisms of Laminar-Boundary-Layer Transition. *Annu. Rev. Fluid Mech.* 26, pp. 441-482.

King, L. (1914a) On the convection of heat from small cylinders in a stream of fluid: determination of the convectional constants of small platinum wires with application to hot-wire anemometry. *Proc. Royal. Soc. London.* 12, pp. 563-570.

King, L. (1914b) On the convection of heat from small cylinders in a stream of fluid. *Phil. Trans. Royal Soc*. A214, pp. 373-432.

Kohama Y., Saric W., Hoos J. (1991) A high-frequency, secondary instability of crossflow vortices that leads to transition. *Proc. R. Aero. Soc. Conf. Bound.-Layer Transit.* Cambridge, England, pp. 4.1-4.13.

Kohama, Y. (2000) Three-dimensional boundary layer transition study. *Current Science*. 79(6), pp. 801-807.

Klebanoff, P., Tidstrom, K., Sargent, L. (1962) The three-dimensional nature of boundary-layer instability. *Journal of Fluid Mechanics*.12, pp. 1-34.

Lachmann, G. (1961a) *Boundary Layer and Flow Control*. 1. Oxford: Pergamon Press LTD.

Lachmann, G. (1961b) *Boundary Layer and Flow Control*. 2. Oxford: Pergamon Press LTD.

Lindfield, A., Pinsent, H., Pinsent, P. (1961) Approximate methods of calculating the three-dimensional boundary layer on wings. *Boundary Layer and Flow Control*. In Lachmann, G. (2), pp. 842-912.

Lynn, P. (1989) *An Introduction to the Analysis and Processing of Signals.* 3rd ed. MacMillan Education LTD: London.

MacManus, D., and Eaton, J. (1996) Predictions and Observations of the Flow Field Induced by Laminar Flow Control Microperforations, *Exp. Therm. Fluid. Sci.* 13, pp. 395-407.

MacManus, D., and Eaton, J. (2000) Flow physics of discrete boundary layer suction-measurements and predictions, *J. Fluid Mech*. 417, pp. 47-75.

Maddalon, D., Collier, F., Montoya, L., Putnam, R. (1989). Transition Flight Experiments on a Swept Wing with Suction. *IUTAM: Third symposium on Laminar-Turbulent Transition.* Toulouse. September 11-15.

Malik, M., Li, F., Choudhari, M., Chang, C. (1999) Secondary instability of cross flow vortices and swept-wing boundary-layer transition, *J. Fluid Mech*. 399, pp. 85-115.

National Instruments (2019) *Understanding FFTs and Windowing*. [online]. Accessed 12 Dec 2019.

Cummings R., Mason, W., Morton, S., McDaniel, D. (1998) *Applied Computational Aerodynamics: A Modern Engineering Approach.* Cambridge Aerospace Series: Cambridge.

Meyer, W. (1955) Preliminary report on the flow field due to laminar suction through holes. *Northrop Aircraft. Rep.* BLC-75.

Mueller and Patone (1998) Air Transmissivity of Feathers. *The Journal of Experimental Biology*. 201, pp. 2591-2599.

Nishioka, M., Asai, M. Ida., S. (1980) An experimental investigation of the secondary instability. *Laminar-Turbulent Transition: IUTAM Symposium Stuttgart.*in Eppler, R. Fasel, H. Berlin: Springer-Verlag. 432, pp.37-46.

Perry, A. (1982) *Hot-wire Anemometry.* Oxford University Press: Oxford.

Pfenninger, W., Bacon, J. (1961) About the development of swept laminar suction wings with full chord laminar flow. *Flow Control*. In Lachmann, G. (2), pp. 1007-1032.

Pfenninger, W. (1977) Laminar Flow Control Laminarization. *Agard Report.* 654, pp. 3.1-3.75.

Poll, D. (1985) Some observations of the transition process on the windward face of a long yawed cylinder. *J. Fluid Mech.* 150, pp. 329-356.

Rayleigh, L. (1880) On the stability, or instability, of certain fluid motions. Proc. Lond. Mathe. Soc. 11(1).

Renaux, J., Blanchard, A. (1992) The design and testing of an airfoil with hybrid laminar flow control. *Office National d'Etudes et de Recherches Aerospatiales*. 1st European Forum on Laminar Flow Technology. Hamburg. March 16-18.

Reed., H., Saric, W. (1989) Stability of three-dimensional boundary layers. *Annu. Rev. Fluid Mech.* 21, pp. 235-284.

RS (2019) Platinum Resistance PT100 & PT1000 Thin Film Detectors. [online]. Accessed: 05 Apr 2019.

Saric, W., Reed., H. (1986) Effect of Suction and Weak Mass Injection on Boundary-Layer Transition. *AIAA Journal*. 34(3), pp. 383-389.

Saric, W. (1986) A Year-End Report on the Three-Dimensional Structure of Transitional Boundary Layers. *Air Force Office of Scientific Research.* AFOSR-TR-87-0739.

Saric, W., Nayfeh, A. (1977) Nonparallel stability of boundary layers with pressure gradients and suction. *AGARD.* 224(6).

Saric, W., Carrillo, R., Reibert, M. (1998) Leading-Edge Roughness as a Transition Control Mechanism. *36th AIAA Aerospace Sciences Meeting and Exhibit*. U.S.A: NV.

Saric, W., Reed., H., White, E. (2003) Stability and Transition of Three-Dimensional Boundary Layers. *Ann. Rev. Fluid. Mech.* 35, pp. 413-440.

Sattarzadeh, S., Fransson, M. (2017) Spanwise boundary layer modulations using finite discrete suction for transition delay. *Exp Fluids.* 58(14), pp. 1-14.

Schlichting, H. (1979) *Boundary-Layer Theory*. 7th ed. McGraw-Hill: New York.

Schmid, P., Henningson, D. (2001) Stability and transition in shear flows. *Applied Mathematical Sciences.* 142. New York: Springer.

Serpieri, J., Kotsonis, M. (2016) Three-dimensional organisation of primary and secondary crossflow instability. *J. Fluid Mech.* 799, pp. 200-245.

Setra (2019a) *Model 239: High Accuracy, Low-Differential Pressure Transducer*. [online]. Accessed: 05 Apr 2019.

Setra (2019b) *Model 270: Setraceram for Barometric, Gauge or Absolute Pressure*. [online]. Accessed: 05 Apr 2019.

Steinhart, J., Hart, S. (1968) Calibration curves for thermistors. *Deep-Sea Research.* 15, pp. 497-503.

Tollmien, W., Grohne, D. (1961) The Nature of Transition. *Boundary Layer and Flow Control*. In Lachmann, G. (2), pp. 602-636.

Van Bokhorst, E. (2017) *Private Communication.*

Wassermann, P., Kloker., M. (2002) Mechanisms and passive control of cross-flow-vortex induced transition in a three-dimensional boundary layer. *J. Fluid Mech.* 456, pp. 49-84.

White, F. (2011) *Fluid Mechanics.* 7th ed. McGraw-Hill: New York.

White, E., Saric, W. (2005) Secondary instability of crossflow vortices. *J. Fluid Mech.* 525, pp. 275-308.

12 Appendices

A Pump Power Estimation

After determining a design mass-flow rate for the suction system: the pipe geometry and the suction pump could be chosen. What follows is an analysis to determine the pressure losses across the suction system, which can be used to estimate the amount of power required from the suction pump. Furthermore, this analysis allows geometry to be adjusted to more easily realise the specified volumetric flowrate.

A.1 Darcy-Weisbach model

Bernoulli's equation, which holds along an inviscid streamline, can benefit from the addition of a viscous correction factor, to account for pressure losses due to viscous effects. These losses can be accounted for through use of a total pressure loss coefficient added to Bernoulli's equation, as shown in Equation 12.1 (White 2011; Fox and McDonald 1994).

$$\Delta P_{Ti} = \left(P_{si} + \rho g y_i + \frac{\rho V_i^2}{2} \right) - \left(P_{s(i-1)} + \rho g y_{(i-1)} + \frac{\rho u_{(i-1)}^2}{2} \right) \qquad \textbf{Equation 12.1}$$

$$\Delta P_{Ti} = P_{Tfi} + P_{Tlmi} = \frac{\rho}{2}\left(\frac{64\nu}{V_i} \frac{L_i}{D_i^2} + K_i \right) u_i^2 \quad \text{(Laminar Flow)} \qquad \textbf{Equation 12.2}$$

$$\Delta P_{Ti} = P_{Tfi} + P_{Tlmi} = \frac{1}{2g}\left(f \frac{L_i}{D_i^2} + K_i \right) u_i^2 \quad \text{(Turbulent Flow)} \qquad \textbf{Equation 12.3}$$

Where ΔP_{Ti} is the total pressure drop across a station in a pipe system, P_{Tfi} is the total pressure drop due to major/friction losses, P_{Tlmi} is the total pressure drop due to minor losses/ changes in pipe geometry, ν is kinematic viscosity, y is height above a reference plane, f is a turbulent friction factor, g is acceleration due to gravity, D is pipe diameter, u is velocity through the pipe, L is the pipe length,and K is the minor loss coefficient.

The total pressure loss coefficient can be separated into major and minor losses (White 2011; Fox and McDonald 1994). The major losses are attributed to frictional losses, and these change in the case of a turbulent flow (see Equation 12.3).

If R_D exceeds 4000, the flow is assumed turbulent, if R_D is less than 2000 it is assumed laminar (White 2011). In the author's analysis the flow is assumed turbulent in between these Reynolds numbers, to provide a more conservative estimate of the system pressure loss, and pump power required.

The minor losses are associated with sudden and gradual changes in geometry that may induce total pressure loss, such as: bends, contractions, and expansions. Minor losses are represented through the parameter 'K_i' in Equation 12.2 and Equation 12.3. Values for this parameter are determined using equations, graphs or tables found in the literature and appropriate dimensional parameters (White 2011; Fox and McDonald 1994). For example, a sudden contraction would depend on the two diameters on either side of the contraction, and bends would depend on bend radius.

In Equation 12.2, in the laminar case, the friction factor is represented by a simple Reynolds number relation. However, for turbulent flows a more complex relation is required and is shown in Equation 12.4 (White 2011).

$$\frac{1}{f^{1/2}} = -2\log_{10}\left(\frac{e}{3.7D_i} + \frac{2.51}{R_D f^{1/2}}\right) \qquad \textbf{Equation 12.4}$$

Equation 12.4 must be solved using an iterative technique. An approximate solution is used to determine an initial guess which will reliably converge, this approximation is shown in Equation 12.5 (Fox and McDonald 1994). 'e' is a material dependent roughness parameter and must be determined from experiments, it can be referenced from tabulated cases for certain materials (White 2011).

$$f_0 = 0.25\left[\log_{10}\left(\frac{e}{3.7D_i} + \frac{5.74}{R_D^{0.9}}\right)\right]^{-2} \qquad \textbf{Equation 12.5}$$

The power can be also defined as the product between the integrated sum of the stagnation pressure loss at all stations in the suction system, and the volume flow rate through the system, as shown in Equation 12.6.

$$\text{Power} = \sum_{i=1}^{N} P_{Ti}\, Q_T \qquad \textbf{Equation 12.6}$$

A.2 Suction System Internal Geometry

The suction system had relatively complex internal geometry, as multiple pipe sizes were used across the pipe-line, as well as different instruments having different bore diameters. This resulted in a considerable number of minor losses across the pipe-line. In addition, the over-all length of the pipe-line was relatively long, for the diameter considered, resulting in considerable losses due to friction.

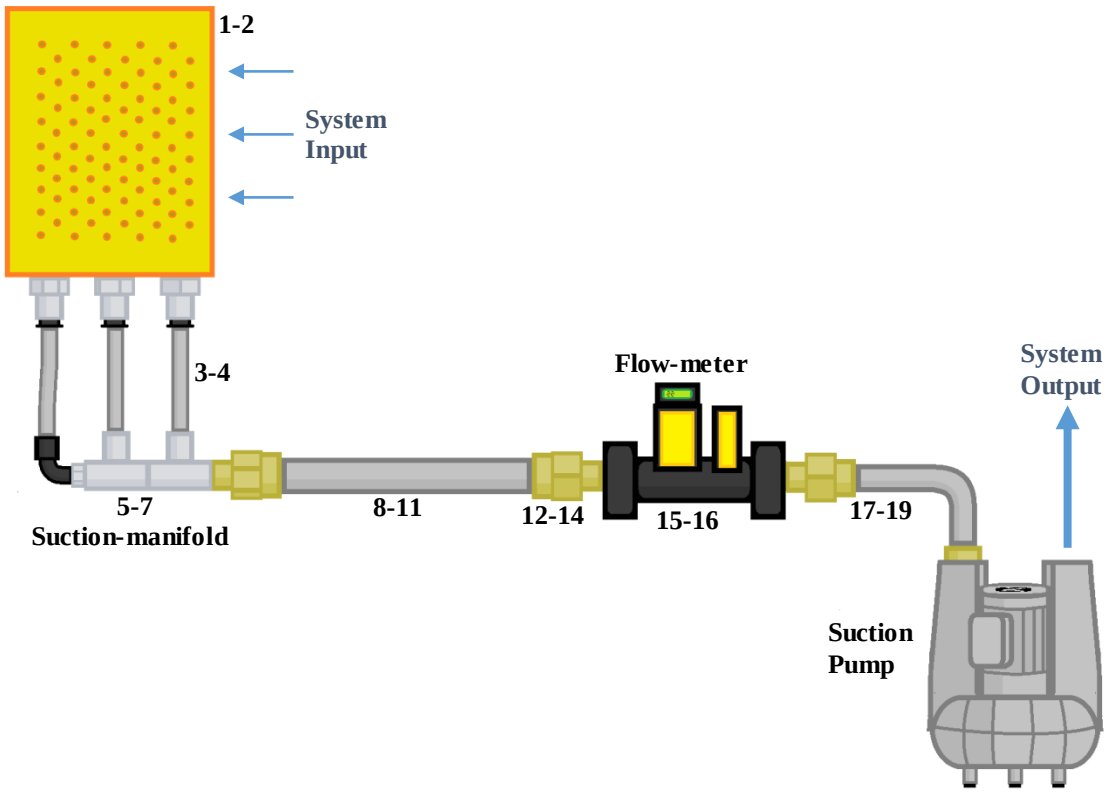

Figure 12.1: Approximate map of the suction system, labelling stations where minor pressure losses are incurred.

A diagram mapping out the suction system can be seen in Figure 12.1. A series of stations are outlined on the figure, numbering between 1 and 19. Each of these stations corresponds with a change in geometry which induces a minor loss and a change in friction loss; this is significant in application to modelling the system using the Darcy-Weisbach method outlined in Section A.1. Each station corresponds with a different integer value for the index ‘i’ in Equation 12.1 to Equation 12.3.

Stations correspond to lengths rather than positions, because the length of each station or element must be specified in defining the friction losses. A station is required for every change in geometry across the pipe system; for brevity, stations are described here in groups concerning a single component of the system. For example, at station 3 there are losses due to entering a pipe and travelling to its exit, at station 4 there are losses due to exiting the pipe and travelling across the beginning of the fitting which follows. Thus losses associated with the pipe occur for Stations 3-4.

Table 12.1: Description of minor loss types and causes corresponding to Figure 12.1.

Stations	Minor Loss Type	Description
1,2	Sudden contraction and Expansion	Losses entering the suction perforations and exiting them into the suction plenum
3,4	Sudden contraction and Expansion	Losses from leaving suction plenum and entering pipeline
5,6,7	Bending, Sudden contraction and Expansion	Losses across fittings, manifold length, pipe bends
8,9,10,11	Sudden contraction and Expansion	Losses due to several diameter changes across multiple fittings to change pipe diameter
12,13,14	Sudden contraction and Expansion	Losses due to entry into flow-meter (change in bore size)
15,16	Bending, Sudden contraction and Expansion	Losses due to (speculated) internal geometry of flowmeter
17-19	Bending, Sudden contraction and Expansion	Losses due to bore of suction pump inlet being larger than pipeline diameter

A.3 Initial System Pressure Loss Estimate

The results from the Darcy-Weisbach model (see Section A.1), for the system shown in Section A.2, are shown in Figure 12.2. Figure 12.2 (a) and (b) show the estimated pressure loss per station across the system, if the effect of the flow-meter is neglected. Initially to develop a specification for the suction pump, the flow-meter was neglected completely in this analysis.

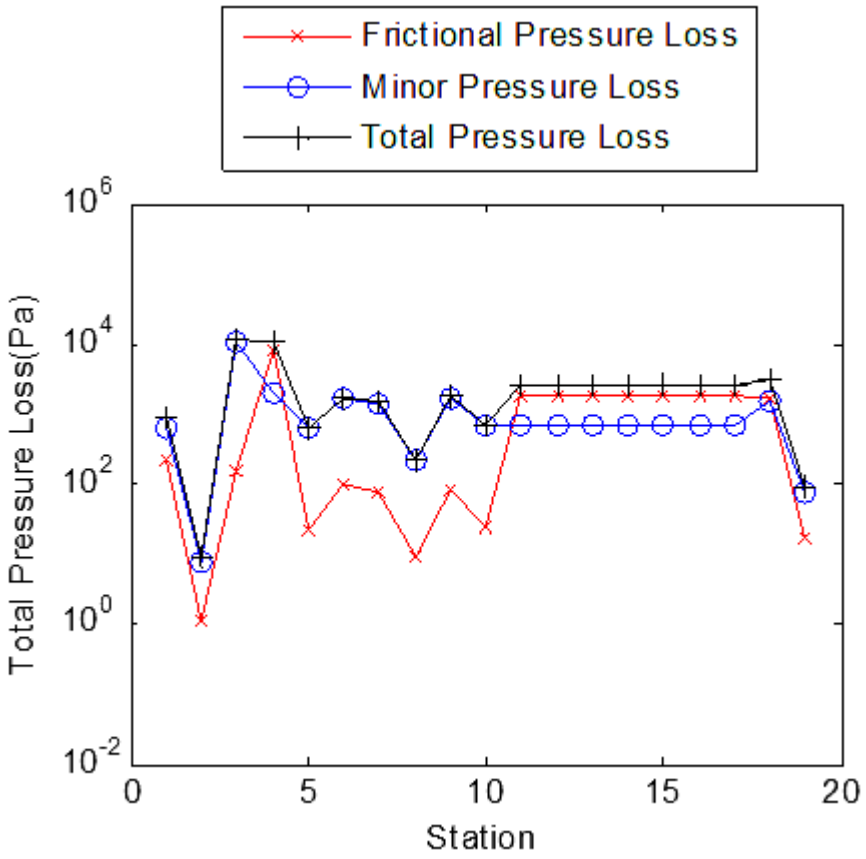

(a)

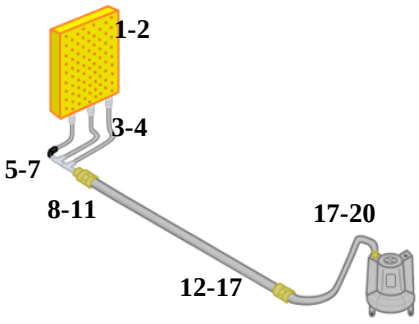

(b)

Figure 12.2: Diagrams showing the pressure loss across the suction system with no flow-meter (a) and (b) accounted for in the analysis.

After purchasing the flow-meter it was found that a significant reduction in mass-flow was realised when compared to what the analysis predicted. After some investigation it appeared likely that the flow-meter was acting as a significant source of pressure loss. When the thermal flow-meter was replaced with a rotameter with a needle valve, it was found maximum flowrate was further reduced. To account for this an empirically derived loss across the flowmeter (see Appendix A.3 for specification) was added to the model. This was done with the aid of illustrations of the internal geometry.

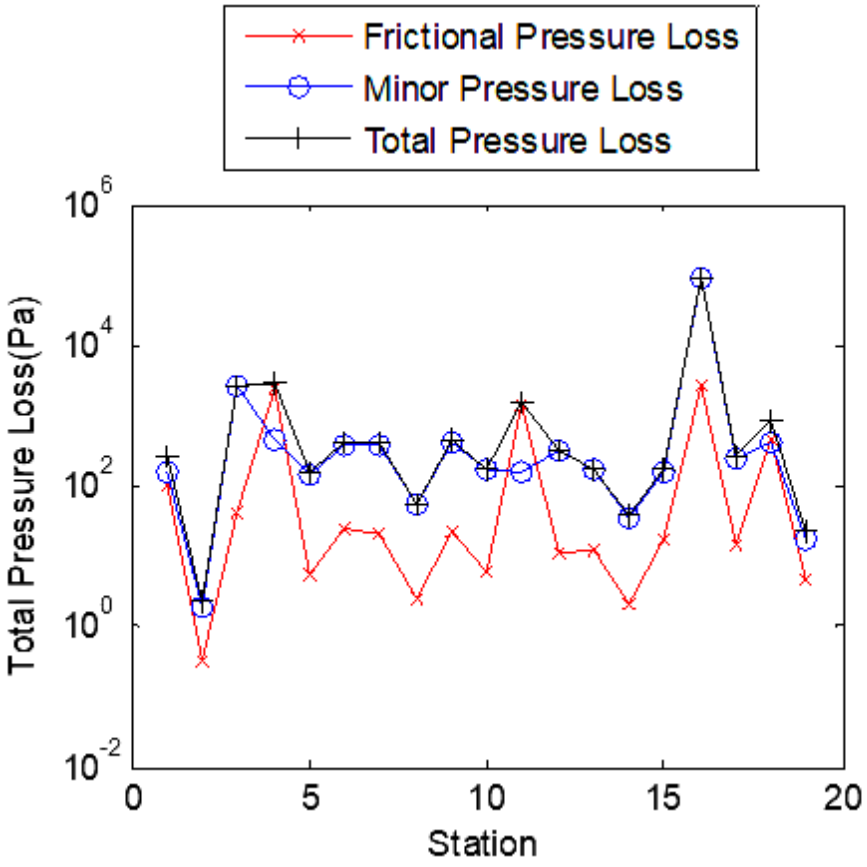

(a)

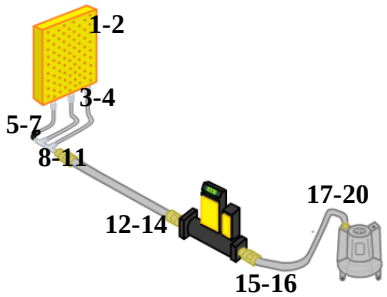

(b)

Figure 12.3: Diagrams showing the pressure loss across the suction system with a flow-meter (a) and (b) accounted for in the analysis.

The dimensions of the internal geometry were systematically varied until the predicted pressure loss matched the loss found in practice. This seems an unreasonable approach to designing a system. However, an iterative procedure was still performed to determine if the inaccuracy of the original calculation could be attributed to the flowmeter, and to provide an approximation should further modifications to the suction system be required after being commissioned.

Figure 12.3 (a) and (b) show the pressure loss per station across the suction system, estimated by the Darcy-Weisbach model with the flow-meter accounted for. Table 12.2 shows the difference in flow-rate estimates as a result when including/ignoring the pressure losses induced by the flow-meter. These estimates assume a fixed hydraulic power of 700W which is specified as electrical power for the pump. It is acknowledged that the pump will not operate at this power across all possible flow-rates, as the hydraulic efficiency will change. However, it was assumed that the pump has an efficiency of 85% based on the maximum flow-rate and pressure drop specified its specification. A baseline specification for the suction pump with no external losses is provided in Appendix A.5.

Table 12.2: The effect of neglecting/including the flow-meter on the Darcy-Weisbach analysis is shown.

Pump Power (w)	Flow-rate without flow-meter	Flow-rate with flow-meter
700	$0.0119m^3/s$	$0.0058m^3/s$
	716L/min	350.05L/min

B Investigation of Error in Experimental Setup and Procedure

As direct information on the low and high frequency disturbances was not readily available in the literature (based on the survey performed in advance of the drafting of the document), it was necessary to investigate these disturbances as potential sources of error in the setup and methodology used in these experiments.

B.1 Repeatability Study

It was of considerable importance to show that the low frequency disturbance is repeatable. Figure 12.4 shows two test cases, where the growth of the low frequency is filtered from the data. It can be seen that there is good agreement between the two test cases. The u_{rms} amplitude of the low frequency disturbance 'A' is plotted with respect to its minimum amplitude 'A_0'. The natural log of this ratio is taken and plotted on the y-axis of Figure 12.4. As in previous plots 'S.S' and 'S.E' mark the beginning and end of the suction array.

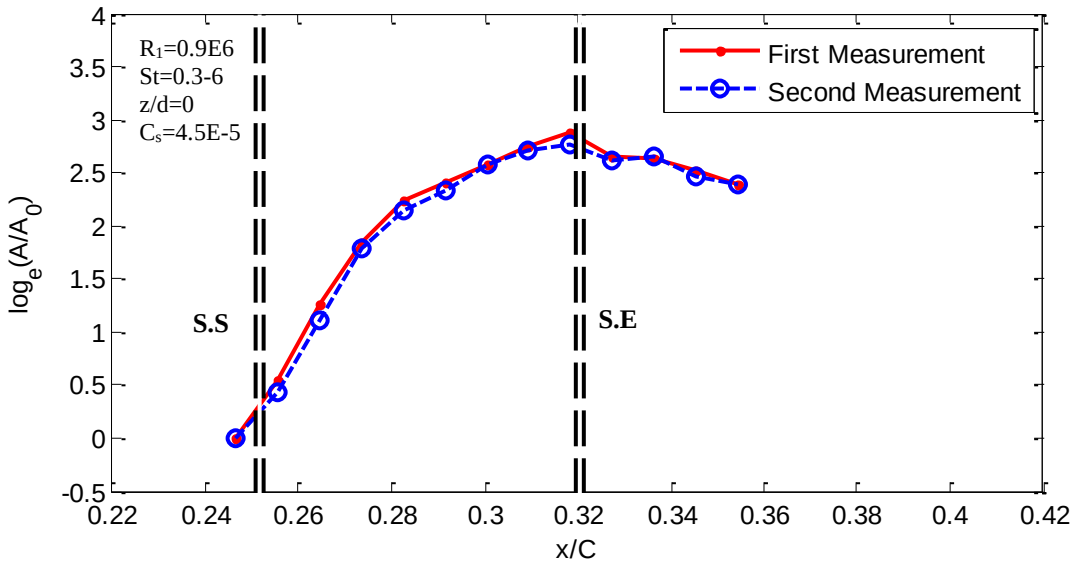

Figure 12.4: Growth of u_{rms} amplitude of low frequency disturbance, for two different test cases with the same flow parameters.

B.2 Suction Pump Unsteadiness and Roughness of Perforation array

A possible source of the low frequency was unsteadiness due to the suction pump, this was briefly investigated in Section 8.1: where it can be seen that suction can be achieved in the absence of the suction pump. Here the low frequency disturbance remains present. However, here, it is not clearly demonstrated that the low frequency is induced by weak suction as opposed to the roughness of the perforations.

In an attempt to clarify this, an additional case was studied (in the presence of a transition front) where the suction outlet was capped and compared to the baseline case and the case with natural suction gradients. This concept is illustrated in Figure 12.5. Corresponding growth curves are shown in Figure 12.6: (a) shows the effect of the different configuration on the forced mode, (b) shows the same effects on the low frequency disturbance.

It appears as though the ‘Closed’ and ‘Blasius’ cases collapse for both Figure 12.6 (a) and (b). However, for the ‘Open’ case in: Figure 12.6 (a) the forced mode is strongly attenuated, and for the low frequency is slightly amplified (as seen in Figure 12.6 (b).

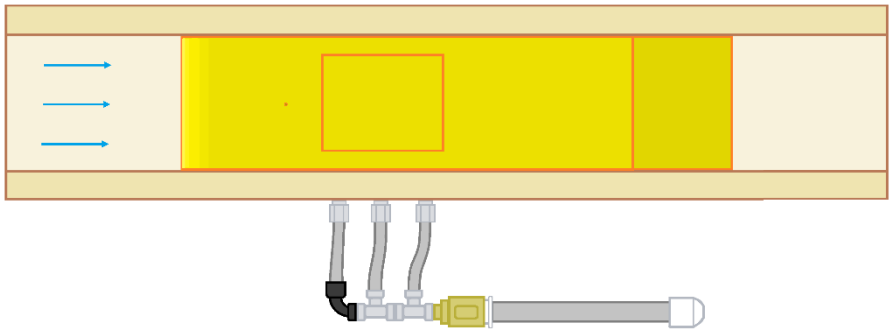

(a)

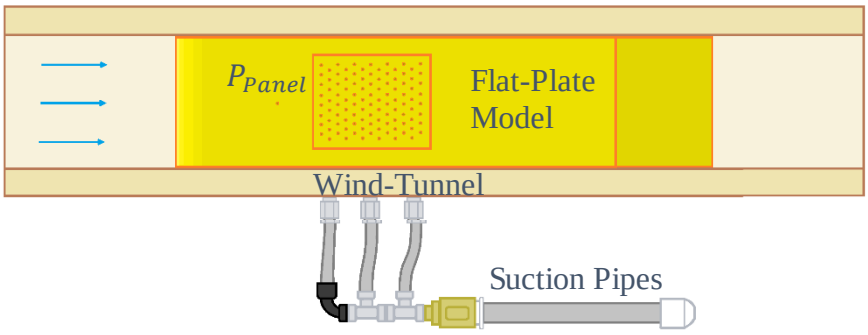

(b)

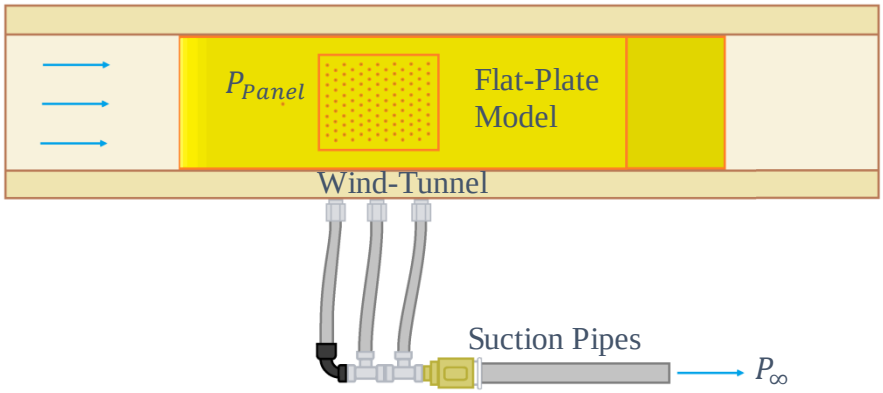

(c)

Figure 12.5: Three basic test configurations used to investigate pump unsteadiness and surface roughness (a) flat-plate with no suction or perforations, (b) Roughness but no suction due to end cap on suction pipes, and (c) flat-plate with suction perforations driven by "natural" pressure gradients perforations.

(a)

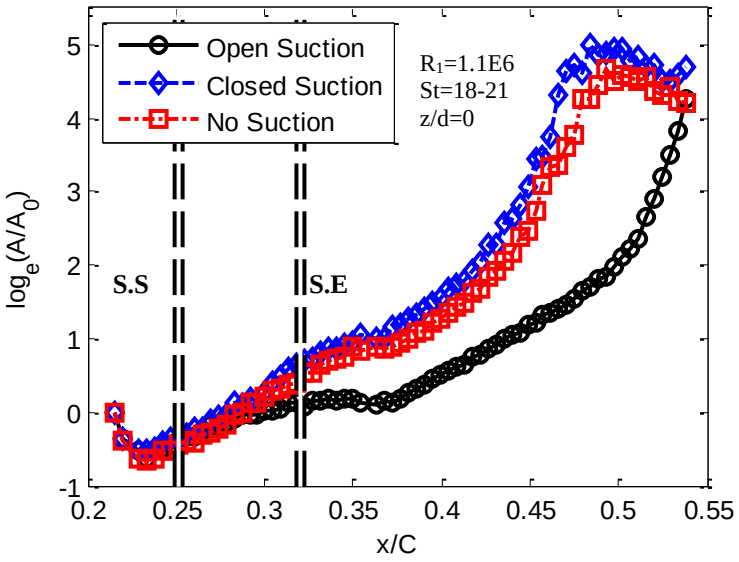

(b)

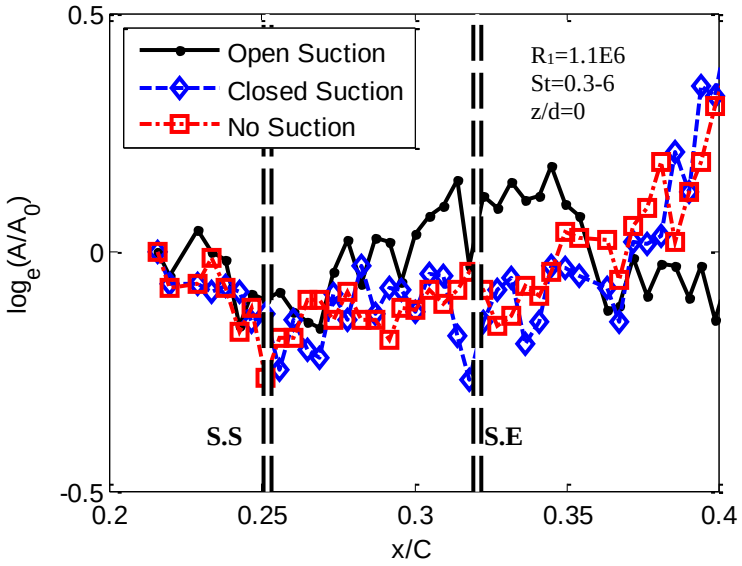

Figure 12.6: Change in normalised amplitude of forced mode (a), and low frequency (b), for cases shown in Figure 12.5 (a-c). Wall forcing at St=19.5

B.3 Suction System Leakage

The effect of system leakage was also investigated. The gasket was loosened, the suction perforations sealed, and the outlet was throttled to ensure the same pressure drop to ambient as when the perforations are unsealed. With these controls in place, the gasket seal was adjusted to form a set of different test cases and the corresponding leakage flow was measured with the flow-meter.

These leakage flows were difficult to measure due to being two orders of magnitude smaller than the smallest suction flow rates considered. For each test case the perforations were unsealed and the throttling of the outlet was removed, the tunnel was then run with suction through the perforation array. The results of these tests are shown in Figure 12.7. There does not seem to be a coherent effect of the leakage on the low frequency disturbance.

It is noted that there was difficulty in measuring the leakage rates due to being of much smaller magnitude than the lowest suction rates. The uncertainty of the flow-meter was high for these test cases (see Section A.3.1).

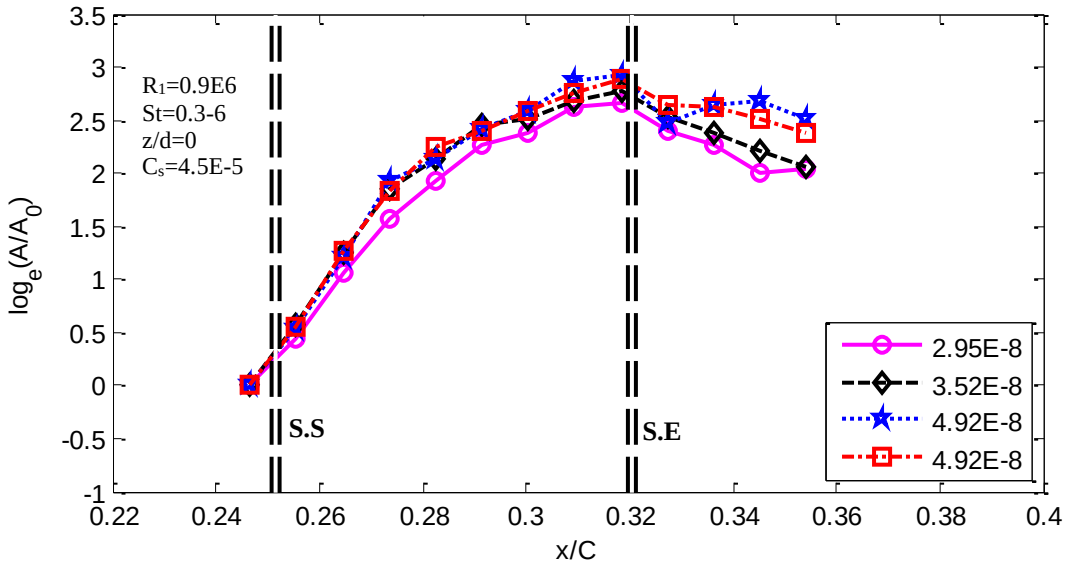

Figure 12.7: Change in normalised amplitude of forced mode (a), and low frequency (b), for different leakage rates.

B.4 Plenum Resonance

Another possible source of the low frequency disturbance was that there could be unsteadiness in the suction flows due to Helmholtz resonation in the suction plenum with the mean flow above the suction array. If this were the case, it was hypothesised that filling the suction plenum with porous foam should have an effect on the resonance. Figure 12.8 shows the effect of different types of porosity on the amplitude of the forced mode in (a) and the low frequency modes in (b).

Four different cases with different porosities were considered: the ‘baseline case’ had no additional porous foam, the ‘porous inserts’ case had porous pipe inserts on the outlet of the suction plenum. The ‘porous plenum’ case consisted of a block of porous foam that filled the volume of the suction plenum, there was a slight gap underneath the perforations. The ‘porous plenum inserts’ case consisted of both pipe inserts and a block of foam inside the suction plenum.

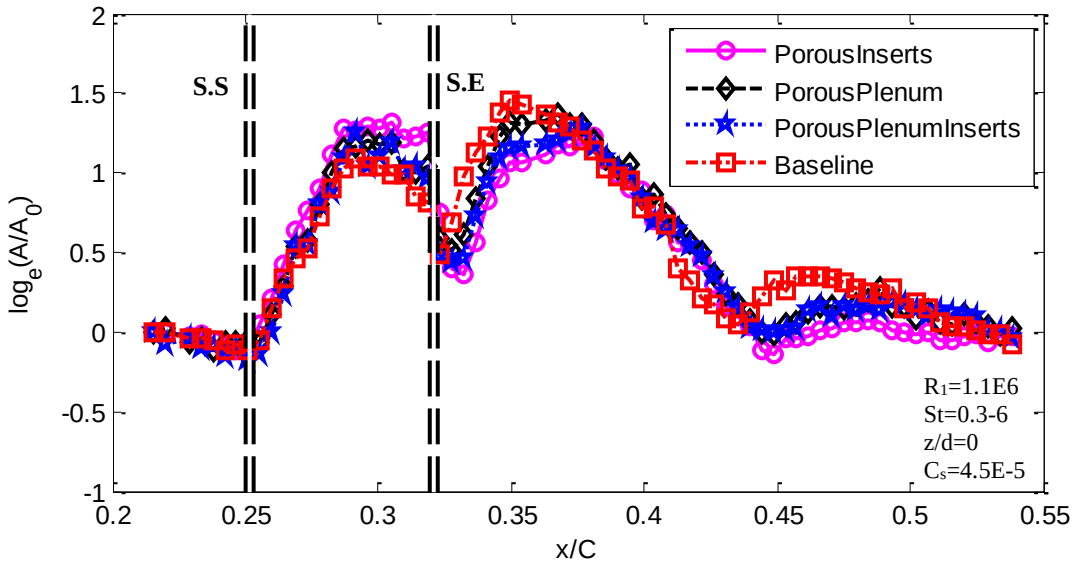

(a)

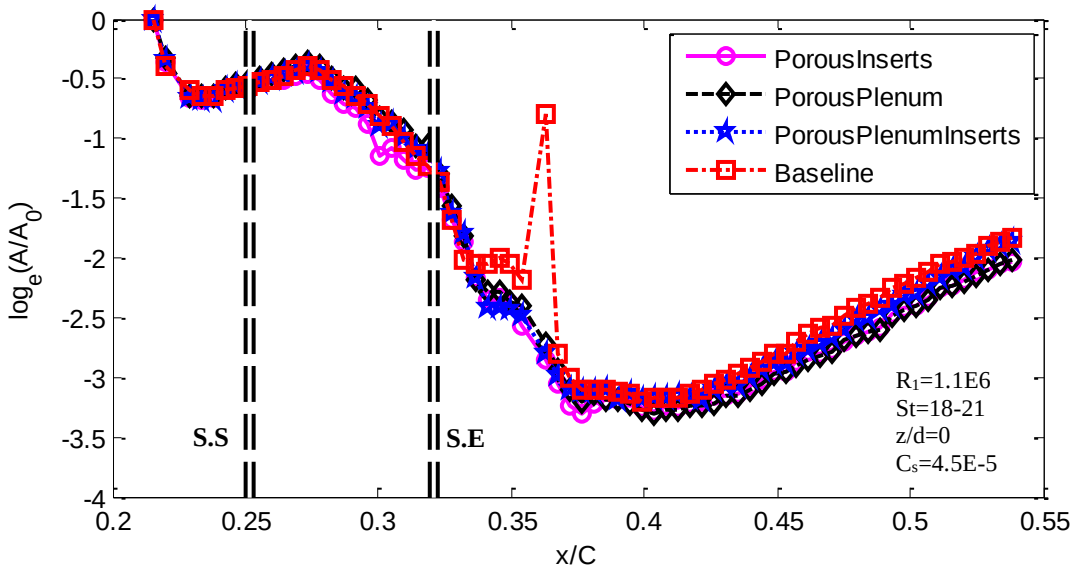

(b)

Figure 12.8: Change in normalised amplitude of forced mode (a), and low frequency (b), for different levels of suction system porosity. Wall forcing at St=19.5

B.5 Pressure fluctuations between neighbouring perforations

Early studies by Butler (1955) and Atkin (2001b) proposed that in the presence of a strong pressure distribution it may be necessary to either backpressure the suction perforations or have multiple cellular suction plenums. The proposed problem is that the static pressure across a wing may drop below the plenum static pressure due to a strong favourable pressure gradient. In this case there may be local blowing instead of suction, alternatively there may be some unsteadiness in the vicinity of the perforations (Butler 1955).

To investigate if this unsteadiness was the source of the low frequency disturbance two test cases were considered, the first was a baseline case with no alterations, the second had a thin porous foam sheet adhered to the back of the suction array (inside the plenum). This method was recommended by Butler (1955) to resolve the unsteadiness in the suction reported in this study.

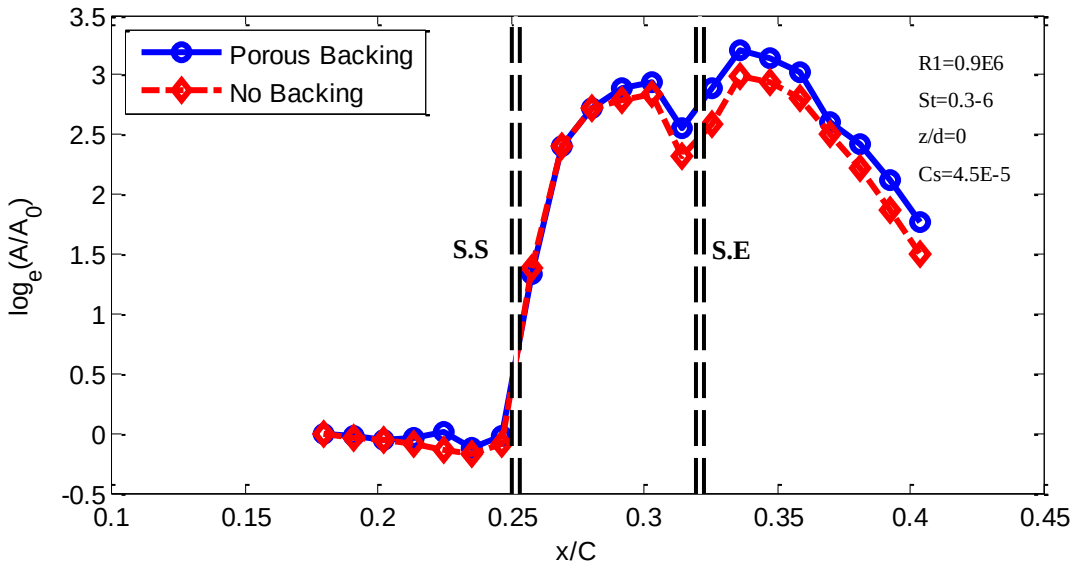

Figure 12.9: Change in normalised amplitude of low frequency modes with and without porous backing.